Title
THE HIGH-FREQUENCY STARK EFFECT AND ITS APPLICATION TO PLASMA DIAGNOSTICS

Author
Hicks, William W.

Publication Date
1973-12-01

LBL-2470

THE HIGH-FREQUENCY STARK EFFECT AND ITS APPLICATION TO PLASMA DIAGNOSTICS

William W. Hicks
(Ph. D. Thesis)

December 1973

Prepared for the U. S. Atomic Energy Commission
under Contract W-7405-ENG-48

LBL-2470

DISCLAIMER

THE HIGH-FREQUENCY STARK EFFECT AND ITS APPLICATION TO PLASMA DIAGNOSTICS

Contents

THE HIGH-FREQUENCY STARK EFFECT AND ITS APPLICATION TO PLASMA DIAGNOSTICS

William W. Hicks

Lawrence Berkeley Laboratory
University of California
Berkeley, California 94720

December 1973

ABSTRACT

This work presents a theoretical and experimental study of the high-frequency Stark effect of hydrogen and helium spectral lines. The theory starts from Schrödinger's equation for an atom in a monochromatic high-frequency electric field and a static magnetic field, and following a method due to Autler and Townes, reduces the problem to an equivalent problem of diagonalizing a matrix equation. The general solution of this matrix equation is discussed in some detail, the photon emission spectrum is calculated for the general case and for typical cases of hydrogen-like and helium-like spectral lines, and a physical interpretation of this solution in terms of multi-quantum transitions is developed. In general, the matrix problem must be solved numerically; however, for weak electric fields, the matrix equation can be expanded in terms of the electric field strength and an analytic solution found. This weak electric field solution reduces to the normal perturbation expression first calculated by Mozer and Barranger using second-order time-dependent perturbation theory, and furthermore yields in a natural way the extension of the Mozer-Barranger theory to include (1) the case of a magnetic field and

(2) the Stark shifts of the atomic levels due to the presence of the high-frequency electric field.

The theory is general, being applicable to any general atomic system for which the energy levels and the dipole coupling coefficients are known. For plasma diagnostics, however, the two most important cases are hydrogen and helium spectral lines. After a discussion of the actual setup of a typical problem, i.e., what energy levels have to be retained, the calculation of the dipole matrix elements and the energy levels, etc., calculated profiles of several spectral lines of both hydrogen and helium for a variety of electric field parameters are presented. For simplicity, all calculations are performed for a magnetic field equal to zero; however, the effect of (1) a dc electric field perpendicular to the high-frequency electric field, and (2) fine-structure splitting on the calculated profiles is considered for the first two hydrogen Balmer lines H_α and H_β.

Finally, calculated profiles for hydrogen and helium are compared to experimental profiles for which the frequency and electric field strength are known. For this purpose a capillary glow discharge is used in conjunction with a calibrated resonant microwave cavity. Over the range of electric field strengths investigated, which included cases for which perturbation theory was totally inadequate, good agreement is found between measured profiles and profiles calculated using the theory described above for the helium spectral lines 4922, 4388, and 4144. It is further found for the experimental parameters of this experiment that the

Blochinzew-type calculation of the hydrogen line profiles is adequate and the fine-structure shift and the dc electric field Stark shift can be included as anomalous broadening of the 'instrumental profile'. Even with this broadening the individual components predicted by Blochinzew are observed for H_α and H_β; for H_γ and H_δ only the envelope could be observed. The electric field frequency and electric field strength determined spectroscopically from the hydrogen and helium spectral lines agreed to within 4% with the corresponding values measured using the standard microwave theory.

I. INTRODUCTION

In 1961 Baranger and Mozer proposed using the high-frequency Stark effect of neutral helium spectral lines as a diagnostic tool to study oscillating electric fields in plasmas.[1] They proposed that "satellites" which were produced by two-quantum transitions induced by a high-frequency electric field could be used to measure the frequency and the field strength of that electric field. They further presented calculations based on second-order time-dependent perturbation theory which related the intensity of these satellites to the electric field frequency and electric field strength. The perturbation calculations were then extended by Reinheimer,[2] and by Cooper and Ringler,[3] who also demonstrated agreement with experimental results for low electric field strengths.

In the years from 1968 to 1973, numerous authors applied the Stark effect to the study of plasmas.[4-14] In two of these experiments[7,9] the electric fields were so high that the validity of calculations based on perturbation theory were questionable. Recognizing this, Kunze et al. modified the perturbation theory by adding a phenomenological damping constant[4] and by extending the calculation of the intensities of the lowest-order satellites to fourth order.[7] However, there were important disadvantages of any perturbation approach to the problem of calculating satellite intensities and positions. First, it was difficult to extend them to include higher-order satellites (higher-order multiple quantum transitions) and second, Stark shifts of the levels (which had not been included in the Mozer-Barranger theory) which changed the

positions of the satellites and which became increasingly important for strong electric fields had to be included in the perturbation theory in an ad hoc, and not entirely satisfactory manner. Recognizing these limitations, Hicks, Hess, and Cooper[15] extended a theory of Autler and Townes,[16] which avoided the usual perturbation treatment, to include more than two upper levels and the interaction of a magnetic field. In two preliminary papers, Cooper and Hicks[17] estimated the range of validity of the perturbation calculations and pointed out possible pitfalls in using the high-frequency Stark effect in plasma diagnostics, and Cooper and Hess[8] pointed out a simplification introduced in the interpretations of the Stark effect data by a magnetic field: By simply inspecting the Zeeman pattern of the satellites it was possible to determine the relative directions of the electric and magnetic field and, if the electric field was circularly polarized, the polarization. This latter technique was also applied by Scott et al.[9]

In recent years there has been a growing interest in the use of the high-frequency Stark effect of neutral hydrogen spectral lines to do plasma diagnostics. The effect of a monochromatic high-frequency electric field on a hydrogen-like atom was first theoretically investigated by Blochinzew[18] in 1933. He found that in a monochromatic high-frequency electric field the hydrogen spectral lines broke up into a symmetric pattern of individual lines separated from each other by the electric field frequency. The intensity of these lines was given by a simple expression involving Bessel functions. His findings were not exploited until 1959

when Mitsuk[19] measured the effect of a microwave electric field (frequency 9.4 GHz) on the H_β spectral line. Mitsuk could not resolve the individual components of the pattern but was able to confirm the predicted dependence of the line width on the electric field strength over a range of from one to 10 kilovolts per centimeter. The results of Blochinzew and Mitsuk were applied by Lifshits et al.[20] to measure the electric field in a plasma-filled waveguide. The application of the high-frequency Stark effect to a plasma with both low-frequency and high-frequency electric fields was theoretically investigated by Lifshits,[21] who derived an expression relating the spectral line width of hydrogen lines to the plasma parameters. Several authors have used Stark broadening of spectral lines to study high-frequency electric fields in plasmas.[22-25]

Recently, Gallagher and Levine reported plasma satellites lying at one and two times the plasma frequency from the position of H_β.[26,27] They interpret their findings as due to the existence of turbulent high-frequency electric fields at the plasma frequency produced during plasma heating in the Tormac plasma containment experiment. Their results do not exactly follow the normal Blochinzew pattern, a discrepancy they feel is due to the presence of the high-dc electric field in their plasma. Calculations by Cohn et al.[28] on H_α appear to confirm this hypothesis, indicating that the presence of a dc electric field can significantly change the Blochinzew pattern.

In this paper we consider both the cases of hydrogen and

helium Stark effects. In Chapter II we review and extend the discussion of the multilevel theory presented in Ref. 15. In Chapter III we review the specific problem of applying the multilevel theory to hydrogen and helium and present numerical calculations for both lines for a variety of cases, including the effect of a dc electric field perpendicular to a high-frequency field on the first two Balmer lines of hydrogen. Chapter IV briefly describes the experiment which was used to test the multilevel theory (a more thorough discussion of this experiment is contained in Appendices C to F). Finally, in Chapter V the predictions of the multilevel theory (as well as other theories) are compared to experimental measurements of hydrogen and helium spectral line profiles.

II. MULTILEVEL THEORY

A. Equivalence of Schrödinger's Equation to an Infinite set of Linear Equations

We start from the time-dependent Schrödinger equation for an atom in external magnetic and electric fields, and split the Hamiltonian into three parts:

$$i\dot{\psi} = H(\vec{r},t)\psi \equiv (H_0 + H_1 + H_2)\psi. \tag{2.1}$$

In Eq. (2.1) and in the rest of this paper all energies are expressed in angular frequency units. H_0 is the time-independent Hamiltonian for the unperturbed atom (no external fields) and is assumed to have a known orthonormal set of eigenfunctions $\{U_j\}$ and corresponding eigenvalues $\{\omega_j\}$:

$$H_0U_j = \omega_jU_J, \qquad j = 1, 2, \cdots. \tag{2.2}$$

In general, H_0 will have an infinite number of eigenfunctions, but for any single calculation only a finite number N will be physically important (their choice will be discussed in Chapter III). H_1 represents the interaction energy between the atom and any externally applied static magnetic or electric field and is time-independent. It will often be possible to pick the $\{U_j\}$ to be eigenfunctions not only of H_0 but also H_1. In this case we define

$$(H_0 + H_1)U_j \equiv \omega_j'U_j. \tag{2.3}$$

For instance, if there is a static magnetic field, $B\hat{z}$, and the

$\{U_j\}$ are hydrogenic eigenfunctions, then

$$\omega_j' = \omega_j + m_j\omega_L, \tag{2.4}$$

where ω_L is the Larmor frequency

$$\omega_L \equiv \frac{1}{2}\left|\frac{eB}{m_e c}\right|,$$

and m_j is the magnetic quantum number of eigenstate j. H_2 represents the interaction energy between the atom and the externally applied electric field. The electric field is assumed to vary harmonically in time with frequency ω, thus allowing separation of the time and space dependence of H_2:

$$H_2(\vec{r},t) = H_2^{+}(\vec{r})e^{i\omega t} + H_2^{-}(\vec{r})e^{-i\omega t}. \tag{2.5}$$

We next expand the wave function

$$\psi(\vec{r},t) = \sum_{j=1}^{N} T_j(t)U_j(\vec{r}), \tag{2.6}$$

where the T's are time-dependent coefficients to be determined. Substituting this expansion into Eq. (2.1) we obtain

$$i\sum_{j=1}^{N} U_j\dot{T}_j = \sum_{j=1}^{N} (\omega_j + H_1 + H_2)U_jT_j. \tag{2.7}$$

We multiply on the left by $U_{j'}^{*}$, integrate over all space, and use the orthonormality of the U's to get (we interchange j and j' for convenience)

$$i\dot{T}_j = \omega_jT_j + \sum_{j'=1}^{N} (\alpha_{jj'} + \beta_{jj'}^{+}e^{i\omega t} + \beta_{jj'}^{-}e^{-i\omega t})T_{j'}, \tag{2.8}$$

where we have defined the following quantities:

$$\alpha_{jj'} \equiv \langle j|H_1|j'\rangle \equiv \int d^3r\, U_j^* H_1 U_{j'}$$

and $$\beta^{\pm}_{jj'} \equiv \langle j|H_2^{\pm}|j'\rangle, \qquad \beta^{\pm *}_{jj'} = \beta^{\mp}_{j'j}. \tag{2.9}$$

Using Floquet's theorem of differential equations,[29] we can expand the time-dependent coefficient T_j as

$$T_j = e^{-i\lambda t} \sum_{s=-\infty}^{\infty} C_{js} e^{-is\omega t}, \tag{2.10}$$

where λ and the C's are time-independent unknowns; the C's are in general complex, and λ is real. Substitution of this expression for T_j into Eq. (2.8) yields

$$\sum_{s=-\infty}^{\infty} (\lambda + s\omega) C_{js} e^{-i(\lambda+s\omega)t} = \sum_{s=-\infty}^{\infty} \omega_j C_{js} e^{-i(\lambda+s\omega)t}$$

$$+ \sum_{j'=1}^{N} \sum_{s=-\infty}^{\infty} C_{j's} \left[\alpha_{jj'} e^{-is\omega t} + \beta^{+}_{jj'} e^{-i(s-1)\omega t} \right.$$

$$\left. + \beta^{-}_{jj'} e^{-i(s+1)\omega t} \right] e^{-i\lambda t}. \tag{2.11}$$

Since this equation must be valid for all times, we may equate coefficients of equal powers of $e^{-i\omega t}$ to give

$$(\omega_j - s\omega - \lambda) C_{js} + \sum_{j'=1}^{N} (\alpha_{jj'} C_{j's} + \beta^{+}_{jj'} C_{j',s+1}$$

$$+ \beta^{-}_{jj'} C_{j',s-1}) = 0; \tag{2.12}$$

$$j = 1, 2, \cdots, N,$$

$$s = -\infty, \cdots, +\infty.$$

This set of equations was solved by Autler and Townes[16] in terms of an infinitely continued fraction for the special case $N = 2$, $\alpha = 0$ (no magnetic field), and $\beta^+ = \beta^-$ (linearly polarized electric field). As pointed out by Autler and Townes, once any single solution has been found to the set of equations (2.12), the new variables

$$\lambda' \equiv \lambda + m\omega,$$

$$C'_{js} \equiv C_{j,s+m}, \; j = 1, \cdots, N, \; s = -\infty, \cdots, +\infty, \tag{2.13}$$

where m is any positive or negative integer, will also comprise a solution. We will refer to solutions related by Eqs. (2.13) as a "set." There are an infinite number of solutions within each set but every solution in a set contains the same physical information, i.e., corresponds to the same wave function ψ, as can be seen by noting that the expression for T_j [Eq. (2.10)] is invariant under the substitution given by Eqs. (2.13).

B. Discussion of the Exact Solution

We have shown above that solving Schrödinger's equation [Eq. (2.1)] is equivalent to solving the infinite set of equations (2.12) for λ and the C's. Given a solution of Eqs. (2.12), substitution of λ and C_{js}, $j = 1, \cdots, N$, and $s = -\infty, \cdots, \infty$, into the expression for ψ gives a solution to Eq. (2.1). Since the Hamiltonian H has been defined over an N dimensional space

made up of the eigenstates of H_0, the complete solution of Eq. (2.1) must consist of N linearly independent ψ's. We have seen above that the solutions of Eq. (2.12) within a single set give the same wave function ψ, thus there must be N different sets of solutions to Eq. (2.12). We denote the different sets with the index "i":

$$\psi_i = e^{-i\lambda_i t} \sum_{j=1}^{N} C^i_{js} e^{-is\omega t} U_j, \qquad i = 1, \cdots, N. \tag{2.14}$$

Before discussing the interpretation of the wave function ψ_i, we will examine its mathematical properties and from them prove two relations between the C's which will be useful in the following two sections. We start from Schrödinger's equation $H\psi_i = i\partial\psi_i/\partial t$ and its Hermitian conjugate $\psi^*_{i'}H = -i\partial\psi^*_{i'}/\partial t$ which together imply

$$\frac{d}{dt}\langle i'|i\rangle \equiv \frac{d}{dt}\int d^3r\, \psi^*_{i'}\psi_i = 0. \tag{2.15}$$

We can use Eq. (2.14) to evaluate ψ_i:

$$\langle i'|i\rangle = e^{-i(\lambda_i-\lambda_{i'})t} \sum_{u=-\infty}^{\infty} e^{-iu\omega t} \sum_{j=1}^{N} \sum_{s=-\infty}^{\infty} C^{i'*}_{j,s-u} C^i_{js}, \tag{2.16}$$

$$u \equiv s - s'.$$

From the above expression we can get a useful relationship between the C's by noting that condition (2.15) requires that the right-hand side of Eq. (2.16) be independent of time. This will be true if and only if

$$\sum_{j=1}^{N} \sum_{s=-\infty}^{\infty} C_{j,s-u}^{i'*} C_{js}^{i} = \chi_i \delta_{ii'} \delta_{u0} \equiv \delta_{ii'} \delta_{u0}. \qquad (2.17)$$

The constants $\{\chi_i\}$ are arbitrary and we have chosen them to be 1 (this choice determines the normalization of the C's).

Using (2.17) we can rewrite (2.16) as

$$\langle i' | i \rangle = \delta_{ii'}, \qquad (2.18)$$

and thus show that at any time t the $\{\psi_i\}$ form an orthonormal set of solutions to the time-dependent Schrödinger equation. Furthermore the $\{\psi_i\}$ form a set of stationary wave functions (the probability density $\psi_i^* \psi_i$ is independent of time when integrated over all space) and hence represent the stationary states of an atom in the presence of a static magnetic field and an oscillating electric field; by stationary we mean that an atom in state ψ_i at time $t = t_0$ will remain in that state indefinitely.

To derive a second relation similar to (2.17) we start by rewriting Eq. (2.14) as

$$\psi_i = \sum_{j=1}^{N} \tau_{ij} U_j; \qquad \tau_{ij} \equiv e^{-i\lambda_i t} \sum_{s=-\infty}^{\infty} C_{js}^{i} e^{-is\omega t}. \qquad (2.19)$$

Since both sets of wave functions, $\{\psi_i\}$ and $\{U_j\}$, form an orthonormal basis for the N-dimensional vector space at any time t, the matrix $\vec{\tau}$ must be unitary for all t. For a unitary matrix $\vec{\tau}$ we must have $\tau^\dagger \tau = 1$. Evaluating this condition in terms of the matrix elements τ_{ij}:

$$\sum_{u=-\infty}^{\infty} e^{-iu\omega t} \sum_{i=1}^{N} \sum_{s=-\infty}^{\infty} C^{i*}_{j',s-u} C^{i}_{js} = \delta_{jj'} \tag{2.20}$$

for all t. Since the right-hand side is independent of t, the left-hand side must be also. This will be true if and only if the C's satisfy the condition

$$\sum_{i=1}^{N} \sum_{s=-\infty}^{\infty} C^{i*}_{j',s-u} C^{i}_{js} = \delta_{jj'}\delta_{u0}. \tag{2.21}$$

As is shown by Eq. (2.19) above, the set of wave functions $\{\Psi\}$ which solves the time-dependent Schrödinger equations represents the rearrangement of the eigenfunctions $\{U_j\}$ into a new set of functions which span the same N-dimensional space as the $\{U_j\}$. The nature of this rearrangement changes in time since $\vec{\tau}$ is a function of time, but at all times the new set of functions form an orthonormal set. We shall assume that the $\{\psi_i\}$ have been chosen such that in the limit $H_1, H_2 \to 0$, $\psi_i \to U_i e^{-i\omega_i t}$. This choice is not necessary but will lead to simplifications in the following sections. When no external fields are present an atom can be characterized by the set of stationary states represented by the wave functions $\{U_j e^{-i\omega_j t}\}$. Each such state has a well-defined energy ω_j; an allowed dipole transition between two such states produces a single spectral line. In the presence of an external oscillating electric field the stationary states of the atom are represented by the $\{\psi_i\}$ or linear combinations (with time-independent coefficients) of the $\{\psi_i\}$. As can be seen from the form of the $\{\psi_i\}$ and expression (2.19) there is no set of states whose

members are both stationary and can be characterized by a unique energy (i.e., have a simple exponential time dependence). As a result spectra produced in the presence of an oscillating electric field are more complicated than in the field-free case: a single line (allowed or forbidden) which would exist in the field-free case is replaced in the field-present case by an infinite series of spectral lines.

C. Transition Rate of an Atom in the Presence of an Oscillating Electric Field

In order to calculate the theoretical radiation pattern emitted by an atom in an oscillating electric field we solve the equation:

$$i \frac{\partial \Phi}{\partial t} = \left[H(t) + H' \right] \Phi, \tag{2.22}$$

where $H(t)$ is as defined in Eq. (2.1) and H' is the particle-radiation field interaction operator:

$$H' = \frac{e}{\hbar m_e c} \vec{A} \cdot (\vec{p} + \frac{e}{c} \vec{A}^{ex});$$

$\vec{p}$ is the momentum of the optical electron, $\vec{A}$ is the vector potential of the radiation field, and $\vec{A}^{ex}$ is the vector potential of any external magnetic field. At any time t, the solutions of the equation $i(\partial\varphi/\partial t) = H(t)\varphi$ form a complete orthonormal set. Hence we may expand $\Phi(t)$ as $\Phi(t) = \sum_d \Gamma_d(t)\varphi_d(t)$, where the sum is over the complete set of the φ_d's. The φ_d's explicitly contain both atomic and radiation field quantum numbers and hence differ from the solutions of Eq. (2.1) (ψ's). Substitution for $\Phi(t)$ in

Eq. (2.22) yields:

$$i \sum_d \frac{d\Gamma_d}{dt} \varphi_d = \sum_d \Gamma_d H' \varphi_d . \tag{2.23}$$

Multiplication of Eq. (2.23) on the left by φ_k^* and integration over all space yields an equation governing the time development of the coefficient Γ_k:

$$i \frac{d\Gamma_k}{dt} = \sum_d \langle k|H'|d\rangle \Gamma_d ; \tag{2.24}$$

the matrix element $\langle |H'| \rangle$ involves integration over both atomic and radiation field variables.

We assume that at $t = \tau$ the system (atom + radiation field) is in a state $\Phi = \varphi_i \left[\Gamma_d(\tau) = \delta_{di}\right]$; then $|\Gamma_k(t)|^2$ is the probability that the system, initially in state i at $t = \tau$, will by time t have undergone a transition to state k by emitting or absorbing photons from the radiation field. If we consider a time interval, $t - \tau$, small compared with the lifetime of state i, then we can solve Eq. (2.24) by iteration:

$$\begin{aligned} \Gamma_k &= \Gamma_k^{(0)} + \Gamma_k^{(1)} + \cdots , \\ \Gamma_k^{(0)} &= \delta_{ki} , \\ \Gamma_k^{(1)} &= - i \int_\tau^t dt \, \langle k|H'|i\rangle \text{ etc.} \end{aligned} \tag{2.25}$$

We now specialize to the problem of spontaneous emission of a single photon in the atomic transition $\psi_i \rightarrow \psi_k$. In the pres-

ence of an oscillating electric field, the state of an atom, both before (ψ_i) and after (ψ_k) a transition, will be described by a wave function of the form (2.14). Then

$$\varphi_k = \Lambda_\gamma e^{-i(\lambda_k+\omega_\gamma)t} \sum_{\ell=1}^{N} \sum_{\sigma=-\infty}^{\infty} C^k_{\ell\sigma} U_\ell(\vec{r}) e^{-i\sigma\omega t}$$

$$\varphi_i = \Lambda_0 e^{-i\lambda_i t} \sum_{j=1}^{N} \sum_{s=-\infty}^{\infty} C^i_{js} U_j(\vec{r}) e^{-is\omega t},$$

where Λ is the radiation field state function; Λ_γ denotes the presence of photon γ, Λ_0 denotes that no such photon is present. By substituting φ_k and φ_i into Eq. (2.25) and performing the time integration ($\lambda_{ik} \equiv \lambda_i - \lambda_k$, $s \equiv s - \sigma$),

$$|\Gamma_k^{(1)}|^2 = \sum_{s,s'=-\infty}^{\infty} K^{ik}_{ss'} e^{-\frac{1}{2} i(s-s')\omega(t+\tau)} \times \frac{\sin \frac{1}{2}\left[(\omega_\gamma - \lambda_{ik} - s\omega)(t-\tau)\right]}{\frac{1}{2}(\omega_\gamma - \lambda_{ik} - s\omega)} \times \frac{\sin \frac{1}{2}\left[(\omega_\gamma - \lambda_{ik} - s'\omega)(t-\tau)\right]}{\frac{1}{2}(\omega_\gamma - \lambda_{ik} - s'\omega)} \qquad (2.26)$$

$$K^{ik}_{ss'} \equiv \sum_{j,j'=1}^{N} \sum_{\ell,\ell'=1}^{N} \sum_{\sigma,\sigma'=-\infty}^{\infty} \times \langle j'|H'|\ell'\rangle\langle \ell|H'|j\rangle C^k_{\ell'\sigma'} C^{k*}_{\ell\sigma} C^{i*}_{j's'+\sigma'} C^i_{js+\sigma}$$

$$K^{ik}_{s's} = K^{ik*}_{ss'}$$

where the matrix element $\langle|H'|\rangle$ now denotes integration only over atomic variables.

As a function of ω_γ, $|\Gamma_k^{(1)}|^2$ consists of a series of "peaks" with centers $\omega_\gamma = \lambda_{ik}+s\omega$ and widths $\sim 1/(t - \tau)$. For $\omega(t - \tau) >> 1$ the peaks are narrow relative to the interpeak spacing ω and we can approximate $|\Gamma_k^{(1)}|^2$ by

$$|\Gamma_k^{(1)}|^2 \simeq \int d\omega_\gamma \sum_{u=-\infty}^{\infty} \delta(\omega_\gamma - \lambda_{ik} - u\omega) I_k^{iu},$$

where I_k^{iu} is the number of photons emitted in transitions from state i to state k into solid angle $d\Omega$ with $\omega_\gamma \simeq \lambda_{ik} + u\omega$ during the time interval (τ,t):

$$I_k^{iu} \equiv \int_{\omega_-}^{\omega_+} d\omega_\gamma \, |\Gamma_k^{(1)}|^2 \rho(\omega_\gamma) d\Omega$$

$$= 2\pi\rho(\lambda_{ik} + u\omega)d\Omega \sum_{s=-\infty}^{\infty} \mathrm{Re}\left[K_{us}^{ik} \left(\frac{e^{i(s-u)\omega t} - e^{i(s-u)\omega\tau}}{i(s - u)\omega} \right) \right]$$

$\rho(\omega_\gamma)$ is the density of photon states/radian-solid angle and $\omega_\pm = \lambda_{ik} + u\omega \pm \Delta$, where Δ is chosen to satsify $1/(t - \tau) \ll \Delta \ll \omega$. In performing the integrations above we have used the sharply peaked nature of the integrands by evaluating $\rho(\omega_\gamma)$ and the matrix elements at the peak center and then letting $\Delta \to \infty$ (see Appendix A). Of more physical interest than $|\Gamma_k^{(1)}|^2$ is its time derivative, the differential transition rate:

$$\frac{d}{dt}\left|\Gamma_k^{(1)}\right|^2 = 2\pi\int d\omega_\gamma\ \rho(\omega_\gamma)d\Omega \sum_{u,s=-\infty}^{\infty} \delta(\omega_\gamma - \lambda_{ik} - u\omega)$$

$$\times\ \mathrm{Re}\left[K_{us}^{ik} e^{i(s-u)\omega t}\right]. \qquad (2.27)$$

The differential transition rate given by Eq. (2.27) is a rapidly varying function of time for frequencies for which the approximations above hold $\left[\omega \gg (t-\tau)^{-1} \gg (\text{lifetime of state } k)^{-1}\right]$, and hence of more experimental interest is the time-averaged differential transition rate dA_i^k. Evaluation of the matrix elements in Eq. (2.27) (using the dipole approximation) and $\rho(\omega_\gamma)$ yields

$$\langle \ell|H'|j\rangle = i\left(\frac{2\pi e^2}{\hbar v\omega_\gamma}\right)^{1/2} \omega'_{j\ell}\xi_j^\ell \qquad \text{and} \qquad \rho(\omega_\gamma) = \frac{v\omega_\gamma^2}{8\pi^3c^3},$$

where v is the system volume, and where we have defined the following quantities

$$\omega'_{j\ell} \equiv \omega'_j - \omega'_\ell, \qquad \omega'_j \equiv \int d^3r\ U_j^*(H_0 + H_1)U_j, \qquad \text{etc., and}$$

$$\xi_j^\ell \equiv \int d^3r\ U_\ell^*\, e_\gamma^* \cdot \vec{r}\ U_j.$$

Then

$$dA_i^k = \int d\omega_\gamma \frac{e^2 d\Omega}{2\pi\hbar c^3} \sum_{s=-\infty}^{\infty} \omega_\gamma \delta(\omega_\gamma - \lambda_{ik} - s\omega)$$

$$\times \left| \sum_{j,\ell=1}^{N} \sum_{\sigma=-\infty}^{\infty} \omega'_{j\ell}\xi_j^\ell\, C_{\ell\sigma}^{k*} C_{js+\sigma}^{i} \right|^2. \qquad (2.28)$$

We now consider two special cases of Eq. (2.28) which will be applicable to the spectra discussed in the next chapter.

Case (1). In many instances we can assume that the final state k is negligibly affected by the electric field. As can be seen from the perturbation solution for λ and the C's, Eq. (2.48), this condition will occur if all states k' coupled to the state k by a nonzero electric dipole matrix element $\beta^{\pm}_{kk'}$ also satisfy $|\omega'_k - \omega'_{k'}| \gg |\beta^{\pm}_{kk'}|$ and ω. In addition, if we assume that a representation of the unperturbed eigenstates has been chosen such that both H_0 and H_1 are diagonal operators, then the final state k can be described by the wave function

$$\psi_k = U_k e^{-i\omega'_k t}. \tag{2.29}$$

In terms of our general wave function Eq. (2.14), we have

$$\begin{aligned} \lambda_k &= \omega'_k \\ C^k_{\ell\sigma} &= \delta_{\ell k}\delta_{\sigma 0}. \end{aligned} \tag{2.30}$$

Then the time-averaged differential transition rate takes on the form

$$dA^k_i = \int d\omega_\gamma \frac{e^2 d\Omega}{2\pi\hbar c^3} \sum_{s=-\infty}^{\infty} \delta(\omega_\gamma - \lambda_i + \omega'_k - s\omega) \times \left| \sum_{j=1}^{N} \omega'_{jk} \xi^k_j C^k_{js} \right|^2. \tag{2.31}$$

Case (2). Hydrogen-like spectra in a sinusoidally-oscillating linearly polarized electric field ($\vec{E} = E_0 \cos\omega t\, \hat{z}$) with no external static fields present ($H_1 = 0$). For this case the zero-order energy levels are degenerate ($\omega_j = \omega_0$, $j = 1, \cdots, N$) and for a proper choice of the eigenfunctions $\{U_j\}$ Schrödinger's equation (2.1) can be solved directly.[18] One chooses the $\{U_j\}$ to be eigenfunctions of both H_0 and H_2. Then Schrödinger's equation for ψ_j reduces to

$$i\dot{\psi}_j = (\omega_0 + \omega\Delta_j \cos\omega t)\psi_j, \qquad \Delta_j \equiv \frac{|e|E_0}{\hbar\omega} \langle j|z|j\rangle \tag{2.32}$$

which has the solution (J_s is the Bessel function of the first kind of order s)

$$\psi_j = U_j e^{-i(\omega_0 t + \Delta_j \sin\omega t)} = U_j e^{-i\omega_0 t} \sum_{s=-\infty}^{\infty} J_s(\Delta_j) e^{-is\omega t} \tag{2.33}$$

or in terms of the general solution (2.14)

$$\lambda_i = \omega_0$$

$$C^i_{js} = \delta_{ij} J_s(\Delta_i). \tag{2.34}$$

For this case dA^k_i has the form

$$dA^k_i = d\omega_\gamma \frac{e^2 d\Omega |\xi^k_i|^2 \Delta\omega^2}{2\pi\hbar c^3} \sum_{s=-\infty}^{\infty} \omega_\gamma \delta(\omega_\gamma - \Delta\omega - s\omega) J_s^2(\Delta_{ik}) \tag{2.35}$$

where we have defined $\Delta\omega \equiv \omega_0$ (for the initial set of levels) $-\omega_0$ (for the final set of levels), $\Delta_{ik} \equiv \Delta_i - \Delta_k$, and where we have used the fact that [see Ref. 30, Eq. (9.1.75)]

$$J_s(\Delta_i - \Delta_k) = \sum_{\sigma=-\infty}^{\infty} J_\sigma(\Delta_k) J_{s+\sigma}(\Delta_i). \qquad (2.36)$$

D. Photon Emission Spectrum for an Ensemble of Atoms in an Oscillating Electric Field

We define $S(\omega_\gamma)d\omega_\gamma d\Omega$ to be the number of photons emitted into solid angle $d\Omega$/sec with polarization e_γ and with frequencies in the range ω_γ to $\omega_\gamma + d\omega_\gamma$. In the following we shall ignore the effect of Doppler shifts in the frequencies of the photons due to motion of the emitting atoms. Such effects are easily included in the usual way by performing a folding integral of $S(\omega_\gamma)$ with the neutral velocity distribution function.[31] $S_i^k(\omega_\gamma)$, the photon emission spectrum for the transition $\psi_i \to \psi_k$, is then given by the integrand of expression (2.28):

$$S_i^k(\omega_\gamma) = \frac{e^2}{2\pi\hbar c^3} \sum_{s=-\infty}^{\infty} \omega_\gamma \delta(\omega_\gamma - \lambda_{ik} - s\omega) \times \left| \sum_{j,\ell=1}^{N} \sum_{\sigma=-\infty}^{\infty} \omega'_{j\ell} \xi_j^\ell \, C_{\ell\sigma}^{k*} C_{js+\sigma}^{i} \right|^2 . \qquad (2.37)$$

The total photon emission spectrum S from an ensemble of N_a atoms populating the N states $\{\psi_i\}$ will be expression (2.37) summed over final states, averaged over initial states, and summed over photon polarization:

$$S(\omega_\gamma) = \sum_{e_\gamma} \sum_{i=1}^{N} K_i \sum_{k=1}^{N'} S_i^k, \qquad K_i \equiv \frac{N_i}{N_a} . \qquad (2.38)$$

Here N_i is the number of atoms in the state i, N' is the number of final states, and K_i represents the probability that the state i is occupied by atoms in the ensemble and has the normalization

$$\sum_{i=1}^{N} K_i = 1. \tag{2.39}$$

The value given to K_i in any particular problem will be governed by physical considerations. In the calculations presented in the following sections we have assumed that

$$K_i = 1/N, \; i = 1, \cdots, N; \tag{2.40}$$

i.e., that each of the states ψ_i is equally populated by atoms in the ensemble. In the limit of no external fields where $\psi_i \to U_i$, Eq. (2.40) is just the assumption that the N eigenstates $\{U_i\}$ are in thermal equilibrium at a high temperature. Such a situation occurs in most laboratory plasmas when random collisions (and not radiative transitions) are the dominant mechanism inducing transitions among states with different values of i and when the average kinetic energy of the colliding particles is large compared with the interlevel energy spacing of the N states. Then the energy levels are "degenerate" with respect to collisional excitation and deexcitation, and the effect of collisions will be to maintain equal populations. In the presence of external fields, energy levels of the N states are shifted relative to each other, by energies of the order of ω and $\lambda_i - \omega_i$, but we still expect collisional processes to maintain equal populations if the mean

kinetic energy of the colliding particles is much greater than these energy shifts. We can make the analogy of assumption (2.40) and high-temperature thermal equilibrium more explicit by considering a consequence of Eq. (2.40). From Eq. (2.19), the probability that an atom in the state i is also in the eigenstate U_j is

$$|\tau_{ij}|^2 = \sum_{u=-\infty}^{\infty} e^{-iu\omega t} \sum_{i=1}^{N} C_{j,s-u}^{i*} C_{js}^{i} \tag{2.41}$$

and is time dependent. Then W_j, the probability that the eigenstate j is populated by the atoms in the ensemble, is given by Eq. (2.41) averaged over the states i:

$$W_j = \sum_{u=-\infty}^{\infty} e^{-iu\omega t} \sum_{i=1}^{N} K_i \sum_{s=-\infty}^{\infty} C_{j,s-u}^{i*} C_{js}^{i} = \frac{1}{N} ; \tag{2.42}$$

the latter equality follows from Eqs. (2.40) and (2.21). Thus Eq. (2.40) implies that the probability that the spatial eigenstate j is populated by atoms in the entire ensemble is time-independent and the same for all j even though the probability that a single particle in the stationary state i is in the spatial eigenstate j is time-dependent.

E. Physical Model

We now construct a physical model of the time-averaged behavior of an ensemble of atoms in the presence of a time-varying electric field. Such a model is useful in describing the solution to the Schrödinger equation, Eq. (2.14), in terms of simple physical processes between the atom and the oscillating electric

field, and leads to correct theoretical predictions of atomic spectra when the variation of the differential transition rate, Eq. (2.27), over times of the order of ω^{-1} can be ignored. We first note that from Eq. (2.16) (setting i' = i),

$$\langle i|i\rangle = \sum_{j=1}^{N} \sum_{s=-\infty}^{\infty} |C_{js}^{i}|^2 = 1, \tag{2.43}$$

where we have used Eq. (2.17) to simplify the result. We can also calculate the energy of a particle in state ψ_i:

$$\langle i|H|i\rangle \equiv d^3r\, \psi_i^* i \frac{\partial}{\partial t} \psi_i = \sum_{j=1}^{N} \sum_{s=-\infty}^{\infty} (\lambda_i |C_{js}^{i}|^2 + s\omega \sum_{u=-\infty}^{\infty} e^{-iu\omega t} C_{j,s-u}^{i*} C_{js}^{i}). \tag{2.44}$$

The particle energy oscillates in time due to the interaction of the atom and the external electric field. If we average Eq. (2.44) over the period of the electric field, $T = 2\pi/\omega$, we get

$$\frac{1}{T}\int_0^T dt\, \langle i|H|\rangle = \sum_{j=1}^{N} \sum_{s=-\infty}^{\infty} |C_{js}^{i}|^2 (\lambda_i + s\omega). \tag{2.45}$$

We could equally well obtain the above equation by using the following model. We consider an ensemble of atoms populating the state i. We assume that each atom in the ensemble has "eigenstates" characterized by the "quantum numbers" (i,j,s); such a state has a spatial dependence U_j and an energy $\lambda_i + s\omega$. The probability that the state (i,j,s) is populated by atoms in the ensemble is assumed to be $|C_{js}^{i}|^2$. In this model Eq. (2.43) represents the normalization for the probability and Eq. (2.45)

represents the ensemble-averaged energy. If we extend our ensemble to include atoms in the states $\{\psi_i,\ i = 1, \cdots, N\}$, then the probability of the state (i,j,s) in the enlarged ensemble will be $|C^i_{js}|^2$ multiplied by the probability that the state i is populated, i.e., K_i, and the average energy of an atom in the enlarged ensemble will be

$$E_{av} = \sum_{i=1}^{N} \sum_{j=1}^{N} \sum_{s=-\infty}^{\infty} K_i |C^i_{js}|^2 (\lambda_i + s\omega). \qquad (2.46)$$

Atoms in the ensemble undergo transitions between the states $\{(i,j,s),\ i = 1, \cdots, N,\ j = 1, \cdots, N \text{ and } s = -\infty, \cdots, +\infty\}$ owing to the interactions with quanta of the external electric field. An interaction consists of the emission (absorption) of a quantum; the new state (i',j',s') after the interaction will have i' = i (each state i is stationary) and s' = s - 1 (s' = s + 1); i.e., its energy after the interaction will have been decreased (increased) by the quantum energy. Since the field quanta carry angular momentum of 1 (in units of $\hbar$), the state after an interaction will differ in the index j from the state before the interaction. For instance, in the particularly simple case where the $\{U_j\}$ are also eigenfunctions of the orbital angular momentum L, the change in j will follow the selection rule: $\Delta\ell \equiv \ell' - \ell = \pm 1$, where $\ell \equiv \langle j|L|j\rangle\hbar$.

In this model the energy of the state (i,j,s), $\lambda_i + s\omega$, has the following interpretation: the energy difference between ω_i (the energy of state i in the limit, $H_1, H_2 \to 0$) and $\lambda_i + s\omega$

is the result of the Stark shift of the energy levels, the Zeeman splitting, and the exchange of quanta with the electric field. We assume that a representation of the $\{U_j\}$ can be found such that both H_0 and H_1 are diagonal; then the Zeeman shift of state i is $m_i\omega_L$. We must now decide which member of each set of solutions to choose for each ψ_i. From Eqs. (2.13) it is clear that each number of the set will have a different value of λ_i. If we choose that solution in each set for which $\Delta E \equiv \lambda_i - m_i\omega_L - \omega_i$ goes to zero when the electric field goes to zero, then we can interpret ΔE as the Stark shift, and s as the net number of electric field quanta absorbed or emitted by the atom in the state (i,j,s). Under this assumption as the electric field goes to zero

$$C^i_j \to \delta_{ij}\delta_{s0}, \qquad \lambda_i \to \omega_i + m_i\omega_L. \tag{2.47}$$

We can now see the significance of this particular choice. Another member of the set would have the property that a different coefficient $C^i_{j\sigma}$ $(\sigma \neq 0)$ would remain finite in the weak-field limit. Such a situation would not change the physics, since $\lambda_i + \sigma\omega$ is invariant for all members of a set, but would not yield such a simple interpretation; $s - \sigma$ would be the net number of quanta absorbed or emitted in state (i,j,s).

Finally, we note that an atom in the state (i,j,s) can undergo a spontaneous radiative transition to a state with lower energy with which it has a nonzero dipole moment. In such a transition, the energy of the resultant photon will be $\lambda_i + s\omega$ minus the energy of the final state; hence, the optical spectra of atoms in

an oscillating electric field will consist of "satellites," a given satellite being determined by fixed values of i, j, and s. The intensity of such a satellite would be given by $K_i|C^i_{js}|^2$ times the transition rate from U_j to the lower state. However, as can be seen from the correct expression for the total photon emission spectrum (2.37), this simplified model only works in the special case that we can ignore cross terms (those of form $\xi_j\xi_{j'}, j\neq j'$ etc.) in Eq. (2.28). Circumstances under which cross terms can be ignored often occur and are discussed in Sect. F.

F. Weak-Field Limit

If the electric field is weak, then we can get an explicit expression for the solution of Eq. (2.12). We assume $C_{js} = 0$ $(s > 1)$ (higher values of s correspond to multiple quantum transitions which we expect to be rare for weak electric fields) and diagonalize the matrix $\vec{\vec{X}}$ (see Appendix B). The resulting expression for λ and the C's are power series in the small parameters $\beta^{\pm}_{ij}$:

$$\lambda_i = \omega'_i + \omega^S_i + \mathcal{O}(|\beta|^3),$$

$$C^i_{js} = \delta_{s0}\delta_{ij} + \frac{\delta_{s1}\beta^-_{ji}}{(\omega'_{ij} + \omega)} + \frac{\delta_{s,-1}\beta^+_{ji}}{(\omega'_{ij} - \omega)} + \mathcal{O}(|\beta|^2), \qquad (2.48)$$

$$\omega^S_i \equiv \sum_j \frac{|\beta^-_{ji}|^2}{(\omega'_{ij} + \omega)} + \frac{|\beta^+_{ji}|^2}{(\omega'_{ij} - \omega)};$$

ω^S_j is the Stark shift of level i due to the electric field and is quadratic in the electric field amplitude. In deriving the above

expressions we had to assume: $|\beta^{\pm}_{ij}| \ll |\omega'_{ij}|$, and also that $|\omega'_{ij} \pm \omega| \gg \mathcal{O}(|\beta|)$; these assumptions will be discussed below.

First, however, it is of interest to substitute Eq. (2.48) into the expression for the photon emission rate S given by Eq. (2.31). The resulting expression for $S(\omega_\gamma)$ will contain cross terms of the form $\xi^k_j \xi^{k*}_{j'} \beta^{\pm}_{ji} \beta^{\pm *}_{j'i}$. In many cases of physical interest (discussed below) $\xi^k_j \xi^{k*}_{j'} \beta^{\pm}_{ji} \beta^{\pm *}_{j'i} \propto \delta_{jj'}$. In this case Eq. (2.31) reduces to

$$S^k_i(\omega_\gamma) = \frac{e^2}{2\pi\hbar c^3}\left[\omega_\gamma{}^3 \delta(\omega_\gamma - \omega'_{ik} - \omega^S_i)|\xi^k_i|^2 \right.$$

$$+ \omega_\gamma \delta(\omega_\gamma - \omega'_{ik} - \omega^S_i - \omega) \sum_j \frac{|\xi^k_j|^2 |\beta^-_{ji}|^2 \omega'^2_{ji}}{(\omega'_{ij} + \omega)^2}$$

$$\left. + \omega_\gamma \delta(\omega_\gamma - \omega'_{ik} - \omega^S_i + \omega) \sum_j \frac{|\xi^k_j|^2 |\beta^+_{ji}|^2 \omega'_{jk}}{(\omega'_{ij} - \omega)^2}\right]$$

$$+ \mathcal{O}(|\beta|^4). \qquad (2.49)$$

The spectrum given by expression (2.49) consists of three spectral lines: a line resulting from a dipole transition from i to k with resulting photon energy $\omega_\gamma = \omega'_{ik} + \omega^S_i$, and two weaker "satellites" with energies $\omega_\gamma = \omega'_{ik} + \omega^S_i \pm \omega$ which result from two-quantum transitions (one quantum absorbed from or emitted to the electric field). If a dipole transition from i to k is forbidden ($\xi^k_i = 0$), but the dipole matrix elements $\beta^{\pm}_{ji}$ and ξ^k_j are nonzero, then the spectrum is composed of just the two satellites. If $\xi^k_i \neq 0$, then, to lowest order, $S(\omega_\gamma)$ is just the usual spectrum for an "allowed"

dipole transition from i to k.

Expression (2.49) represents the usual perturbation solution to the high-frequency Stark effect. It was first calculated using standard time-dependent perturbation theory by Mozer and Barranger[1] for the case of zero magnetic field and extended to include a static magnetic field by Cooper and Hess.[8] Extensive discussion giving explicit expressions for the matrix elements for neutral helium lines useful in plasma diagnostics for the case of a linearly polarized electric field or a circularly polarized electric field are given in Hicks, Hess, and Cooper.[15] The latter also give profiles for various electric field polarizations relative to a static magnetic field.

We now discuss the assumptions made in deriving Eq. (2.49).

(1) The form of Eq. (2.49) depends on the assumption that the cross terms of the form

$$\omega'_{jk}\omega'_{j'k}\frac{\beta^{\pm}_{ij}\beta^{\pm *}_{ij'}\xi^{k}_{j}\xi^{k*}_{j'}}{(\omega'_{ij}\pm\omega)(\omega'_{ij'}\pm\omega)}, \qquad j\neq j',$$

can be ignored in the final expression for the spectrum $S(\omega)$. Before discussing situations in which this assumption holds, we note that due to the form of the denominators in Eq. (2.49), the leading contribution to the satellite intensities and positions will come from terms in the sums involving intermediate states whose energies lie close to the energy of state i. More distant states will have less effect and states for which the energy separation ω'_{ij} is much greater than the energy separation of the

nearest states can be ignored in computing the satellite intensities and positions. Similarly, cross terms for which j and j' do not both represent states near to the state i can be ignored, since they will not significantly modify the result give in Eq. (2.49) for the frequency spectrum.

We can identify two cases in which the assumption that the cross terms are negligible is valid.

(a) First, if for a given initial state i and final state k there exists only a single intermediate state j which is "near" to the state i and for which the matrix elements ξ_j^k and $\beta_{ij}^{\pm}$ are <u>both</u> nonzero, then the assumption is valid. This situation occurs for the singlet helium lines 4388 ($5^1D - 2^1P$) and 4922 ($4^1D - 2^1P$) for a linearly polarized electric field with either no magnetic field or polarized along the magnetic field, or an electric field circularly polarized perpendicular to the magnetic field. In the above cases, for a proper choice of coordinate system, each initial state (n, $\ell = 3$, m = -3, $\cdots$, 3) is coupled to only a single one of the nearby intermediate states (n, $\ell = 2$, m = -2, $\cdots$, 2) by the matrix element $\beta_{ij}^{\pm}$.

(b) Second, cross terms can be ignored when the time-averaged electric field is axially symmetric with respect to the magnetic field. Then, in the coordinate system with z-axis along the magnetic field, the cross terms vanish when an average is taken over the azimuthal angles of the electric field and of the emitted photon.

(2) $|\beta_{ij}^{\pm}| \ll |\omega_{ij}'|$, i.e., the weak-electric field approxi-

mation. If the electric field is not weak then the problem must be solved numerically by the methods of Sect. A and C. The validity of the perturbation theory as the electric field increases is further discussed in Chapter III. This condition requires that the zero-order energy levels not be degenerate.

(3) $|\omega'_{ij} \pm \omega| \gg |\beta^{\pm}_{ij}|$. If this condition is violated then the perturbation expansion (2.48) is no longer valid, since one of the "small" terms ($\propto \beta^{\pm}$) becomes comparable to the leading term. Since resonant denominators of the form $\omega'_{ij} \pm \omega$ also appear in the perturbation expressions for higher-order terms ($|s| > 1$), we can no longer be sure that the higher-order terms which were ignored in calculating Eq. (2.48) will be weaker than the terms kept.

As noted by Autler and Townes,[16] perturbation theory also breaks down if a higher-order resonance condition is satisfied. If we consider the case most often used in plasma diagnostics where a dipole transition from $i \to k$ is forbidden and a dipole transition from $j \to k$ is allowed, then in the weak-electric-field limit for which perturbation theory is valid the condition for an nth-order resonance can be written as

$$\frac{1}{|\omega'_{ij}|}\,|\omega'_{kj} + \omega^S_i - \omega^S_j \pm n\omega| \lesssim \left(\frac{|\beta^{\pm}_{ij}|}{|\omega'_{ij}|}\right)^n \equiv \epsilon^n, \quad n = 3, 5, \cdots.$$

As can be seen from the above resonance condition, an nth-order resonance occurs when the Stark-shifted position of the nth satellite of the forbidden transition $i \to k$ (the forbidden transi-

tion has only odd-numbered satellites) is separated from the Stark-shifted position of the allowed line $j \rightarrow k$ by a distance of the order of $|\omega'_{ij}|\epsilon^n$. Then the intensity of this satellite (which would normally be much less than the intensity of the allowed line) can be comparable to the intensity of the allowed line. Numerical calculations show that when a resonance occurs two spectral lines separated by a distance of the order of $|\omega'_{ij}|\epsilon^n$ appear at approximately the position of the allowed line predicted by the perturbation theory. A similar situation occurs at the predicted positions of the satellites of the forbidden transition $i \rightarrow k$, where a higher-order satellite of the allowed line (which has only even-number satellites) can be comparable in intensity to the generally much more intense first-order satellites. For weak electric fields the separation between the two lines in each pair is very small and will not be seen in a real experiment with finite resolving power and broadened spectral lines. For stronger electric fields, the separation will be observable only for the lowest-order resonances. If the separation cannot be resolved, then each pair will be observed as a single "satellite" with an intensity equal to the sum of the individual intensities and an average position given by the average of the position of each component weighted by its intensity; numerical calculations using the multi-level theory developed above indicate that the sum intensity and average position are given correctly by Eq. (2.49).

G. Hydrogen-Like Limit

In Chapter II.C We exhibited an exact solution of Eq. (2.12)

which applies in the limit of degenerate energy levels. This solution has the following properties:

(1) The satellite positions are at $\pm n\omega$, relative to the unperturbed spectral line position (n an integer);

(2) the satellite intensities are functions of the frequency ω and the electric field strength E_0 only through the ratio E_0/ω; and

(3) the satellite intensity pattern is symmetric with respect to the unperturbed spectral line position.

The condition necessary to attain this limit can best be determined by referring to Eq. (2.12) and noting that one may write (remember that $\alpha_{jj'}$ was assumed to equal $\alpha_j \delta_{jj'}$ and $\omega_j' \equiv \omega_j + \alpha_j$)

$$\omega_j' = \omega_0 + (\omega_j' - \omega_0) \equiv \omega_0 + \epsilon_j, \qquad j = 1, \cdots, N,$$

where ω_0 is some suitably chosen 'average' energy of the system of N levels. If

$$\omega_{jj'}' \equiv \omega_j' - \omega_{j'}' \ll \omega, \qquad j, j' = 1, \cdots, N \tag{2.50}$$

then each ϵ_j will be a small number and we may solve Eq. (2.12) by standard perturbation-theory techniques. The 'zero'-order problem is just the hydrogen problem whose solution is given by Eq. (2.34). The next higher-order correction will be of order ϵ and hence will be small if condition (2.50) is satisfied. The mechanism of the hydrogen-like limit can be observed in Eq. (2.49) for the weak-field case. In the limit (2.50), Eq. (2.49) predicts

that both the far and near satellites are of equal intensity proportional to $(E_0/\omega)^2$, and are equally spaced about the common position of the two levels [this latter since the Stark shift goes to zero in the limit (2.50)].

III. NUMERICAL CALCULATIONS

A. General Description

In this section we present results of numerical calculations using the theory given in Chapter II.

We do not have an analytical solution to the infinite set of Eqs. (2.12). Instead, we use a numerical method of solution suggested by the physical interpretation.

For weak electric fields, the multiple absorption of s photons becomes less likely as $|s|$ increases (negative values of s correspond to emission) since the larger values of $|s|$ correspond to higher-order terms in the perturbation series. The probability of the absorption of one photon is given by second-order perturbation theory, two photons by third-order theory, etc. As the strength of the electric field increases, the probability of multiple absorption also increases, and higher-order satellites will become observable. However, it is reasonable to assume that even for strong fields the probability of absorbing s photons becomes negligible for $|s|$ sufficiently large. Since this probability is proportional to $|C_{js}|^2$, we assume that

$$C_{js} = 0 \text{ for } \quad |s| > S, \quad j = 1, 2, \cdots, N. \tag{3.1}$$

Then the infinite set of equations (2.12) is reduced to a finite set:

$$\sum_{j'=1}^{N} (\alpha_{jj'}C_{j's} + \beta^{+}_{jj'}C_{j',s+1} + \beta^{-}_{jj'}C_{j',s-1}) + (\omega_j - s\omega - \lambda)C_{js} = 0, \tag{3.2}$$

$j = 1, 2, \cdots, N,$

$s = -S, \cdots, +S.$

Equations (3.2) can be viewed as an eigenvalue equation:

$$\underline{X}\vec{D} = \underline{\lambda}\vec{D}, \tag{3.3}$$

where $\vec{D}$ is an $N(2S + 1)$-dimensional column vector whose elements are in a one-to-one correspondence with the coefficients C_{js}, $j = 1, 2, \cdots, N$ and $s = -S, \cdots, +S$; $\underline{X}$ is an $N(2S + 1) \times N(2S + 1)$ matrix whose elements are chosen so that the set of equations represented by (3.3) is the same set given in (3.2). An example for the case $S = 1$ and $N = 3$ is given in Fig. B-1 in Appendix B. One can easily show that $\underline{X}$ is Hermitian when H is Hermitian. Let $\underline{Z}$ represent the unitary matrix which diagonalizes $\underline{X}$; we have

$$\underline{Z}^{\dagger}\underline{X}\,\underline{Z} = \underline{X}', \tag{3.4}$$

where $\underline{X}'$ is the diagonal matrix whose nonzero elements are the eigenvalues of $\underline{X}$ and hence the solutions for $\underline{\lambda}$. The columns of $\underline{Z}$ are the eigenvectors of $\underline{X}$; they are solutions for $\vec{D}$ and hence for the C's. We can construct a solution for Eq. (2.1) from each of the $N(2S + 1)$ eigenvalues and eigenvectors of $\underline{X}$. As discussed in Chapter II.A, only N of these solutions are to be used in the complete wave function and, as before, the solutions may be divided into N sets, each set now containing $2S + 1$ members. For the infinite set of equations (2.12) all of the solutions within a set can be found from any one member of the set by using the

transformation (2.13); this will only be approximately true in the case of the finite set of equations (3.2) because of the approximation made in truncating the matrices. We must be careful in selecting which eigenvalues and eigenvectors to use. As one method we could choose the solution in each set most accurately fulfilling condition (3.1) above, or we could choose the solution described in the previous section where s has the physical meaning of the net number of photons absorbed or emitted and $\lambda_i - \omega_L m_i - \omega_i$ is the Stark shift. For low electric fields these two choices will be the same.

The solution of Eq. (3.2) generally involves several steps. First those eigenstates which must be included in the expansion of the wave function must be determined. To do this it is helpful to consider the perturbation solution, Eq. (2.48). Because of the resonant denominators, for a given initial state i, the most important intermediate states j to consider are those for which $|\omega'_{ij}| - \omega$ is smallest and β_{ij} is nonzero. However, for strong electric fields, all nearby intermediate states should be included even if β_{ij} is zero, since multiple quantum transitions may be important and two states i and j can be coupled through other intermediate states. For instance, for the 4388-Å He I ($5^1D - 2^1P$) line the 5G level must also be included, since it introduces satellites and strongly affects the position and intensities of the satellites originating from the 5D and 5F levels. If there are intermediate states for which $|\omega'_{ij}| \lesssim \omega$ and β_{ij} is nonzero, then states for which $|\omega'_{ij}| \gg \omega$ can be neglected, unless

very strong fields are present or great accuracy is desired. The best method to determine whether a particular state need be included is to perform the calculations with and without the state and compare results. It should be noted that if there are no 'nearby' states which are coupled to the state i by dipole matrix elements then that state is unaffected by the electric field.

Fortunately, for spectral lines considered for plasma diagnostics and at electric field strengths found in the laboratory the choice of eigenstates is usually straightforward. For hydrogen, it is sufficient and in general necessary to retain all states with the same principal quantum number in calculating both the upper level and the lower level of an optical transition. For helium it is usually sufficient to consider singlet and triplet states independently, the states with principal quantum numbers ≤ 3 to be unaffected by the electric field and to retain only the high angular momentum states (P, D, F, etc.) for principal quantum numbers ≥ 4. For other elements the problem is not determining which states to retain but in finding two states which are both coupled by dipole matrix elements and nearly degenerate enough to give observable satellites. For instance, Ya'akobi and Bekefi[6] have observed plasma satellites of the forbidden lithium transition 3P - 2P near the allowed lithium spectral line at 6103.6 Å (3D - 2P) due to high-frequency electric fields produced by an exploding lithium wire.

Having determined the appropriate states to use, the next step is to calculate the matrix elements α and $\beta^{\pm}$. To do this

we need the unperturbed wave functions $\{U_j\}$. Since, except for hydrogen, these wave functions are not known exactly, some approximation must be made. For the calculations in the following section for helium we have assumed that hydrogenic wave functions are good approximations to the actual wave functions in calculating the α and the $\beta^{\pm}$ matrix elements.

For hydrogenic wave functions the H_1 term is diagonal if the external magnetic field is chosen along the z axis. If the total electron spin of the atom is zero, then $H_1 = \omega_L L_z$, where L_z is the z component of the orbital angular momentum of the excited electron. H_2, the interaction energy of the high-frequency electric field, is

$$H_2 = - (\vec{\mu}\cdot\vec{E}/\hbar) = + |e|(\vec{r}\cdot\vec{E}/\hbar), \tag{3.5}$$

where $\vec{\mu}$ is the electric dipole moment. For linear polarization of the electric field, $\vec{E}(t) = \vec{E}_0 \cos\omega t$ and

$$\beta^{+}_{jj'} = \beta^{-}_{jj'} = (|e|/2\hbar)\langle j|\vec{r}\cdot\vec{E}_0|j'\rangle. \tag{3.6}$$

For circular polarization perpendicular to the magnetic field, $\vec{E}(t) = E_{rms}(\hat{x}\cos\omega t \pm \hat{y}\sin\omega t)$ and

$$\beta^{+}_{jj'} = (|e|E_{rms}/2\hbar)\langle j|x \mp iy|j'\rangle, \tag{3.7}$$

$$\beta^{-}_{jj'} = (|e|E_{rms}/2\hbar)\langle j|x \pm iy|j'\rangle. \tag{3.7}$$

The upper sign corresponds to right-hand circular polarization and the lower sign corresponds to left-hand circular polariza-

tion relative to the magnetic field.

The final quantity to be determined in Eq. (3.2) is the unperturbed energy of each state. For hydrogen the energy can be exactly calculated. For non-hydrogenic atoms some other method must be used. For the helium calculations in the next section we have used experimentally determined values for the unperturbed energy levels.

B. Helium Calculations

We have used our theory to investigate extensively two optical transitions of parahelium, the 4922-Å ($4^1D - 2^1P$) and 4388-Å ($5^1D - 2^1P$) He I lines. For the upper levels in these two cases, the only states which need be included in calculations for electric fields $E_{rms} < 20$ kV/cm and frequencies $\omega, \omega_L < 75$ GHz are the 4P, D, and F, and the 5P, D, F, and G, respectively. The lower states (n = 2) are negligibly affected by the electric field because the 2P, m = 0, $\pm$ 1 states are not coupled by the $\beta^{\pm}$ matrix elements and the 2P levels are widely separated from any other levels. However, the 2P levels are split by a static magnetic field.

For our calculations, we have used Martin's values[32,33] for the eigenvalues of H_0 and hydrogen-like eigenfunctions for the $\{U_j\}$.

In the calculations which are presented below, we have not included a magnetic field. A thorough treatment of the effects of a magnetic field is given in Ref. 15, and the new phenomena which arise when the perturbation treatment is not valid are

similar to those which are shown below for the case of electric field alone. That is, higher-order satellites and Stark shifts become important.

Figures 3-1 and 3-2 show calculated Stark profiles of He 4922 Å and He 4388 Å for an electric field frequency of 35.1 GHz (1.17 cm^{-1}) for various field strengths. This frequency was chosen because it is the one used in the experiment described in Chapter IV. In the calculations we have set S = 10 for $E_{rms} \leq 6$ kV/cm and S = 15 for stronger fields. These values were determined by performing the calculations for varying S until an increase did not significantly change the satellite intensities and positions. The resulting matrix $\underline{X}$ has then been numerically diagonalized using a CDC 6600 computer. Since for strong electric fields there are a great many satellites which contribute significantly to the spectrum, the main features of the spectrum are more easily seen if the multitude of theoretical lines predicted by our calculations are "smoothed" by folding with an "instrument" function. To obtain the profiles shown in the figures we have used the function

$$I = 10^{-4x^2/(x^2+\alpha^2)}, \tag{3.8}$$

where x is the distance in angstroms from a line center and α has been set to give a full width at half-maximum of 0.2 Å. This instrument function produces a line shape which is often observed experimentally for nonhydrogenic lines: Gaussian at the center and Lorentzian in the wings, with a weak continuum

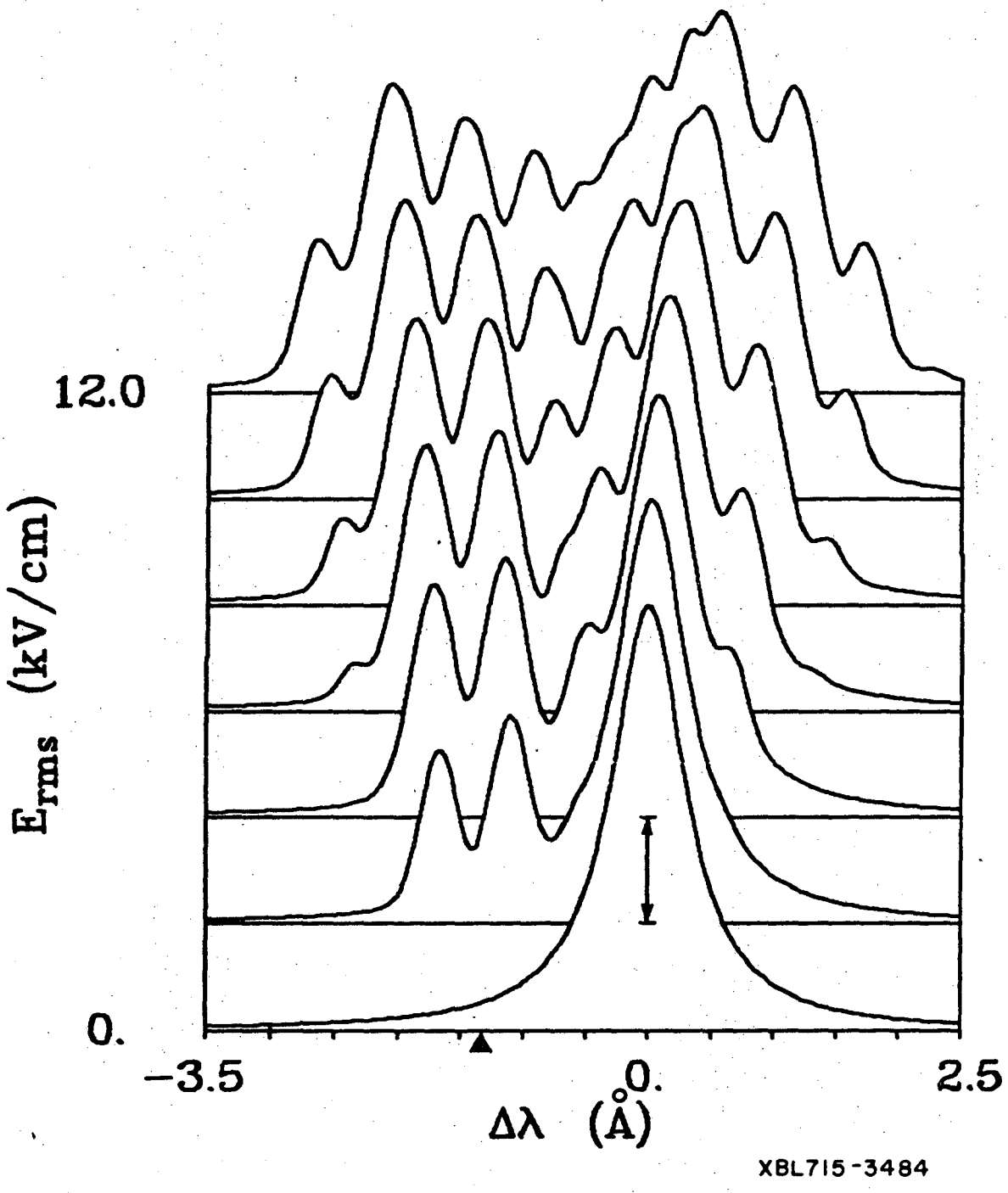

Fig. 3-1. For legend, see page 40a.

Fig. 3-1. Calculated Stark profiles in the vicinity of the 4922-Å spectral line of He I for the case of no magnetic field and a linearly polarized electric field of frequency 1.17 cm^{-1} and for various electric field strengths, all for direction of observation perpendicular to $\vec{E}$. Each profile is the result of folding the theoretical line spectrum with an instrument function of FWHM of 0.2 Å and is shown plotted logarithmically; a single decade is shown in the figure by a double-ended arrow. $\Delta\lambda = 0$ is the unperturbed position of the allowed line $4^1D \rightarrow 2^1P$; ▲ denotes the unperturbed position of the forbidden transition $4^1F \rightarrow 2^1P$.

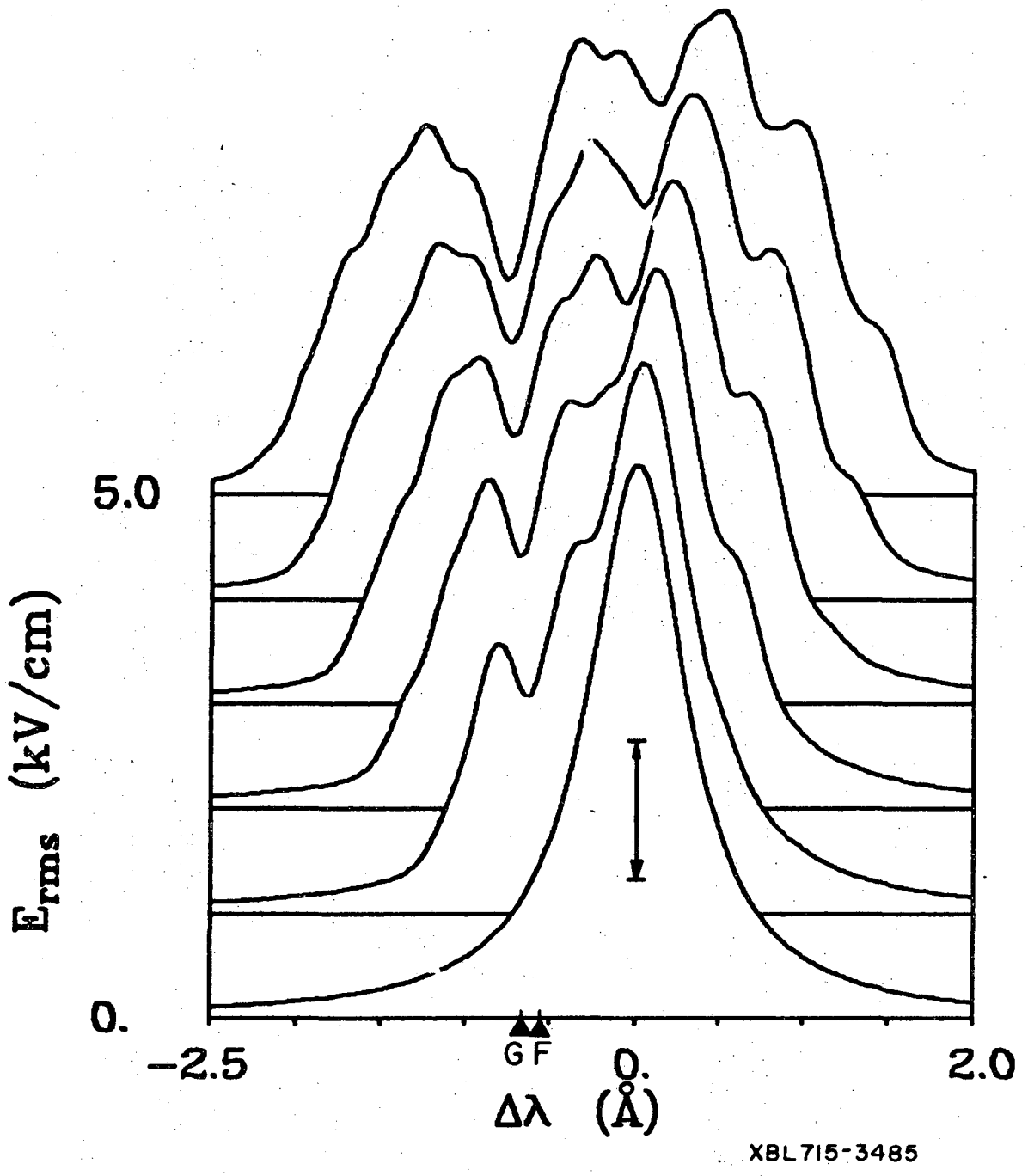

Fig. 3-2. For legend, see page 41a.

Fig. 3-2. Calculated Stark profiles in the vicinity of the 4388-Å spectral line of He I for the case of no magnetic field and a linearly polarized electric field of frequency 1.17 cm^{-1} and for various electric field strengths, all for direction of observation perpendicular to $\vec{E}$. Each profile is the result of folding the theoretical line spectrum with an instrument function of FWHM of 0.2 Å and is shown plotted logarithmically; a single decade is shown in the figure by a double-ended arrow. $\Delta\lambda = 0$ is the unperturbed position of the allowed line $5^1D \rightarrow 2^1P$; $\blacktriangle_F$ and $\blacktriangle_G$ denote the unperturbed positions of the forbidden transitions, $5^1F \rightarrow 2^1P$ and $5^1G \rightarrow 2^1P$, respectively.

background. The half-width and background chosen are approximately those of the experiment described in Chapter IV. In each figure the profiles are plotted lined up behind each other and the intensity of each profile is plotted logarithmically. The first profile in each figure is the instrument function, i.e., the profile for zero electric field.

For weak field strengths the profiles calculated by using the multilevel theory of Chapter II agree with those predicted by perturbation theory (see Chapter II.F). For He 4922 and He 4388, the pattern consists of an intense allowed line arising from the $n^1D - 2^1P$ transition and two weak satellites centered about the position of the forbidden transition $n^1F - 2^1P$ and separated by twice the field frequency. In the following discussion we will follow standard notation, referring to either the 'far' ('weak') satellite or the 'near' ('strong') satellite, the former designation for each satellite coming from its proximity to the allowed line (and the latter from its relative intensity).

For higher electric field strengths other satellites appear and grow until they dominate the spectral pattern. The additional satellites are due to multiple photon transitions from the upper set of states to the 2P level. In Fig. 3-1 the allowed line ($4^1D - 2^1P$) has satellites associated with it which are due to an even number of photons being absorbed or emitted from the external field, while the forbidden transition ($4^1F - 2^1P$) has associated with it satellites due to an odd number of photons being

emitted or absorbed; these additional satellites are separated from the positions of the corresponding transitions by even and odd multiples of the field frequency, respectively. Figure 3-1 also shows the effect of the Stark shift of the 4D and 4F levels: The satellites of the allowed line shifted towards longer wavelengths and the satellites of the forbidden line are shifted towards shorter wavelengths.

The spectra shown in Fig. 3-2 for the 4388-Å line are more complex than those of Fig. 3-1 due to coupling of the 5^1D and 5^1F levels to the nearby 5^1G level. This coupling not only modifies the positions and intensities of satellites arising from the 5^1D and 5^1F levels but also produces an additional group of satellites associated with the forbidden transition ($5^1G - 2^1P$) and separated from it by even multiples of the field frequency. The Stark shift of the 5^1G level and its associated satellites is in the same sense as that of the 5^1F level, i.e., toward shorter wavelengths and "away" from the red-shifted allowed line.

In the limit of very strong electric fields ($\beta_{ij} \gg \omega_i - \omega_j$), the usual characterization of a spectral transition as "forbidden" or "allowed" ceases to be valid. For such a field the levels are strongly coupled and the spectral patterns arising from transitions involving such levels can differ markedly in general structure from the weak field case. Such a situation can be seen in Fig. 3-1, where the very asymmetric weak-field spectral pattern becomes nearly symmetric as the 4^1D and 4^1F levels become more strongly coupled by an increasing electric field.

Figures 3-3 and 3-4 and Table III-1 show the results of further calculations on the 4922-Å He I line, again with a linearly polarized electric field and no magnetic field. The calculation of the data used to produce Table III-1 and Figs. 3-3 and 3-4 requires some discussion. Because we have chosen the electric field polarized parallel to the z axis, each satellite and the allowed line have five uncoupled components, one component arising from a transition from each magnetic quantum level of the ^4D state: 0, ± 1, ± 2, to the 2P state. In general, the spectral intensity and position of each component will be different. Although, in principle, these components might be resolved, their separation is such that at moderate field strengths $\leq$ 10 kV/cm they would appear as a single line when viewed by most optical instruments. Therefore, in calculating entries for the table we have summed the amplitudes of the five components of the appropriate satellite or of the allowed line. Figures 3-3 and 3-4 were plotted from the data of Table III-1 with the following exception. For the case of electric field frequency equal to 3 cm^{-1} a resonance occurred for the higher values of the rms electric field strength. The effect of this resonance is to decrease the intensities of the satellites and the allowed lines at the expense of other satellites (see the end of Chapter II.F). This effect can be most clearly seen from Fig. 3-4 where the ratio of the near satellite to the allowed line decreases rapidly with increasing field strength for the higher field strengths shown. In fact, for 10 kV/cm, the resonant lines are comparable to or

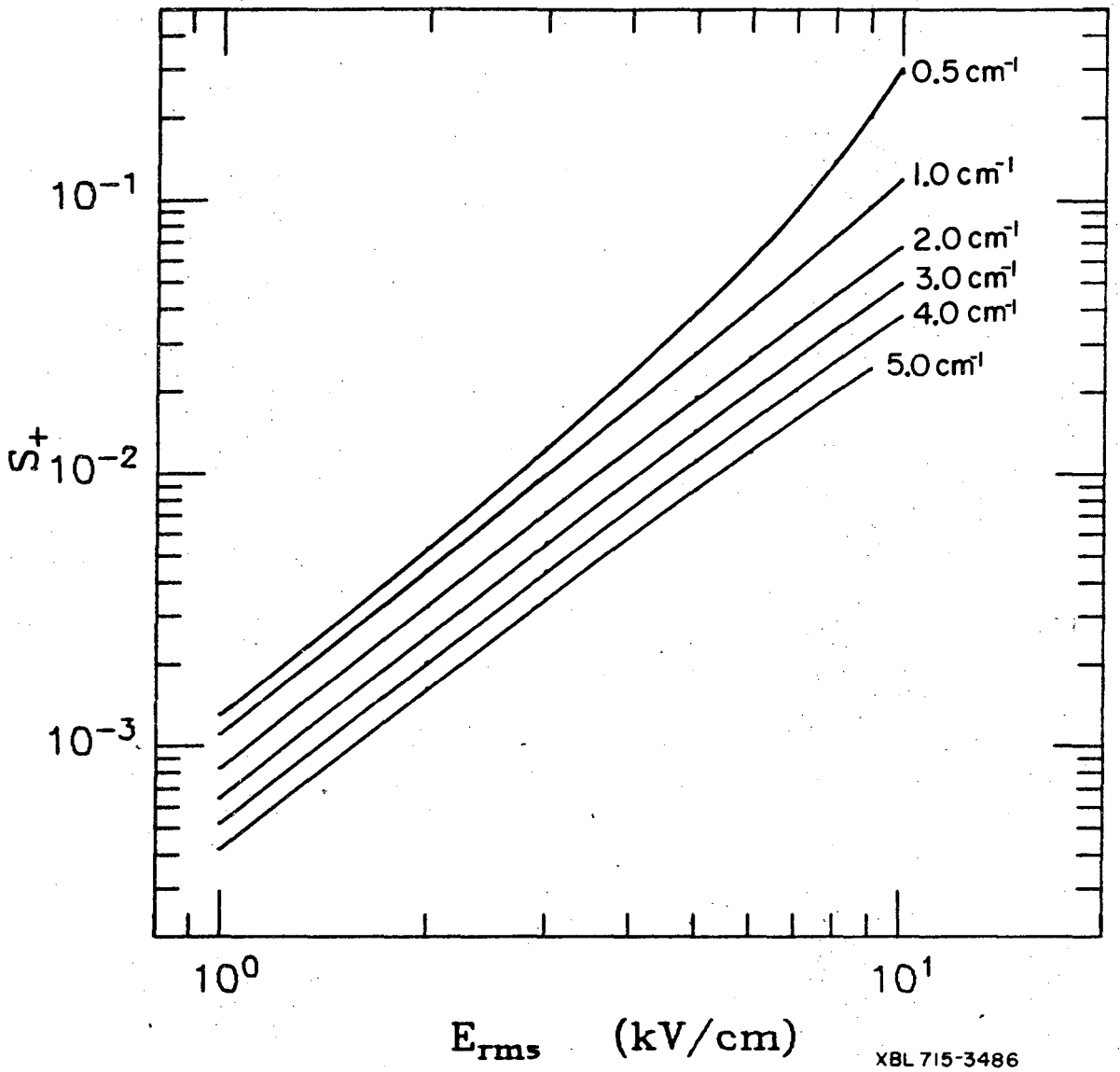

Fig. 3-3. Calculated intensity ratio S_+ of the far satellite of the forbidden transition $4^1F \rightarrow 2^1P$ to the allowed line $4^1D \rightarrow 2^1P$ in He I as a function of rms electric field strength for several electric field frequencies, for a linearly polarized electric field $\vec{E}$, and for direction of observation perpendicular to $\vec{E}$.

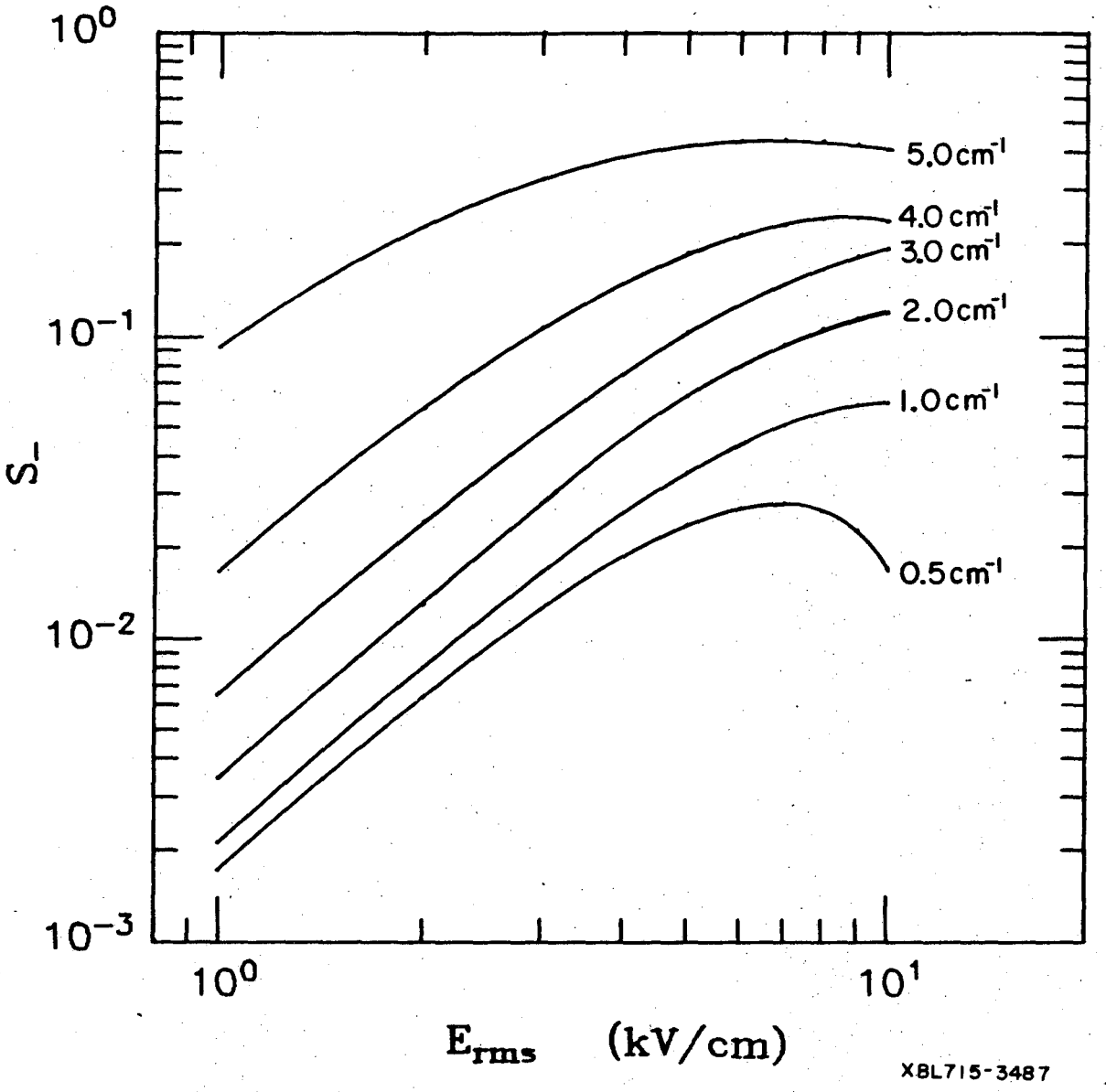

Fig. 3-4. Calculated intensity ratio S_- of the far satellite of the forbidden transition $4^1F \rightarrow 2^1P$ to the allowed line $4^1D \rightarrow 2^1P$ in He I as a function of rms electric field strength for several electric field frequencies, for a linearly polarized electric field $\vec{E}$, and for direction of observation perpendicular to $\vec{E}$.

Table III-1. S_+ and S_- for helium 4922 for various electric field frequencies (in cm^{-1}) and strengths (in kV/cm).

S_-

E_{rms} \ f	0.5	1.0	2.0	3.0	4.0	5.0
1.0	1.78×10^{-3}	2.20×10^{-3}	3.58×10^{-3}	6.77×10^{-3}	1.72×10^{-2}	9.43×10^{-2}
2.0	6.55×10^{-3}	8.29×10^{-3}	1.34×10^{-2}	2.50×10^{-2}	5.93×10^{-2}	2.37×10^{-1}
3.0	1.29×10^{-2}	1.70×10^{-2}	2.87×10^{-2}	4.98×10^{-2}	1.09×10^{-1}	3.38×10^{-1}
4.0	1.93×10^{-2}	2.68×10^{-2}	4.65×10^{-2}	7.61×10^{-2}	1.56×10^{-1}	3.98×10^{-1}
5.0	2.45×10^{-2}	3.64×10^{-2}	6.52×10^{-2}	1.00×10^{-1}	1.93×10^{-1}	4.32×10^{-1}
6.0	2.77×10^{-2}	4.50×10^{-2}	8.17×10^{-2}	1.19×10^{-1}	2.20×10^{-1}	4.48×10^{-1}
7.0	2.86×10^{-2}	5.22×10^{-2}	9.63×10^{-2}	1.30×10^{-1}	2.39×10^{-1}	4.52×10^{-1}
8.0	2.72×10^{-2}	5.75×10^{-2}	1.08×10^{-1}	1.29×10^{-1}	2.48×10^{-1}	4.47×10^{-1}
9.0	2.33×10^{-2}	6.12×10^{-2}	1.17×10^{-1}	1.15×10^{-1}	2.50×10^{-1}	4.37×10^{-1}
10.0	1.75×10^{-2}	6.22×10^{-2}	1.22×10^{-1}	nr	2.46×10^{-1}	4.23×10^{-1}

S_+

E_{rms} \ f	0.5	1.0	2.0	3.0	4.0	5.0
1.0	1.29×10^{-3}	1.10×10^{-3}	8.24×10^{-4}	6.43×10^{-4}	5.15×10^{-4}	4.17×10^{-4}
2.0	5.31×10^{-3}	4.39×10^{-3}	3.26×10^{-3}	2.53×10^{-3}	2.01×10^{-3}	1.60×10^{-3}
3.0	1.24×10^{-2}	9.88×10^{-3}	7.20×10^{-3}	5.54×10^{-3}	4.36×10^{-3}	3.45×10^{-3}
4.0	2.33×10^{-2}	1.76×10^{-2}	1.25×10^{-2}	9.55×10^{-3}	7.46×10^{-3}	5.85×10^{-3}
5.0	3.89×10^{-2}	2.76×10^{-2}	1.90×10^{-2}	1.44×10^{-2}	1.12×10^{-2}	8.75×10^{-3}
6.0	6.08×10^{-2}	3.99×10^{-2}	2.66×10^{-2}	2.01×10^{-2}	1.55×10^{-2}	1.21×10^{-2}
7.0	9.15×10^{-2}	5.49×10^{-2}	3.52×10^{-2}	2.65×10^{-2}	2.03×10^{-2}	1.58×10^{-2}
8.0	1.36×10^{-1}	7.28×10^{-2}	4.48×10^{-2}	3.38×10^{-2}	2.55×10^{-2}	1.98×10^{-2}
9.0	2.00×10^{-1}	9.38×10^{-2}	5.53×10^{-2}	4.21×10^{-2}	3.13×10^{-2}	2.41×10^{-2}
10.0	2.98×10^{-1}	1.18×10^{-1}	6.68×10^{-2}	nr	3.75×10^{-2}	2.88×10^{-2}

even more intense than the original satellites and the spectral pattern is unrecognizable (i.e., so complicated than an experimenter who measured such a pattern could not possibly identify the weak satellite and near satellite by visual inspection), and so the entry for this case has been denoted 'nr' in the table. However, from the calculations it is possible to identify the weak and far satellites and also the satellites of the allowed level in resonance with them. For the figures we have calculated S_+ and S_- for the resonant cases by summing the contributions to the satellite intensities and allowed lines of all nearby resonant components in order to illustrate the discussion given at the end of Chapter II.F, even though in an actual experiment the difference components would be resolvable. This procedure leads to a set of curves of $S_\pm$ vs E_{rms} which appear to change smoothly as a function of frequency.

In Figs. 3-3 and 3-4 the rms electric field is plotted against S_+ (S_-), the ratio of the far (near) satellite to the allowed line, for various frequencies (labeled in inverse centimeters). Perturbation theory predicts straight lines on a log-log plot (S_+ and S_- are each proportional to E_{rms}^2) which are tangent to the curves of Figs. 3-3 and 3-4 at low electric fields. For stronger fields there are increasing deviations from the results of perturbation theory. Figures 3-3 and 3-4, and also Fig. 3-1, show that the intensity of the far satellite is growing faster than the intensity of the near satellite, until at about 8 kV/cm the far satellite is actually stronger. As is noted in

Refs. 8 and 4, and as is clear from Figs. 3-3 and 3-4, the near satellite deviates much more than the far satellite from the predictions of perturbation theory, and the effects of the higher-order terms are to decrease the amplitude of the near satellite relative to the perturbation theory results.

From Figs. 3-3 and 3-4 and from Table III-1, it is, in principle, possible to determine the frequency and amplitude of an electric field from an experimentally measured spectrum. However, the appearance of additional satellites may confuse the spectral pattern even for relatively low field strengths.

For instance, consider Fig. 3-5, which shows a set of profiles of the 4922-Å line of He I for a frequency of 4.0 cm^{-1}. It is not clear from the figure which are the far and the near satellites, even for weak electric fields. The line marked with an arrow is actually a satellite of the allowed line. Another situation where confusion could result is at very low frequencies, since the two satellites will then merge into a single line at the position of the forbidden line. Furthermore, in a plasma the forbidden line is always present due to the quasistatic Coulomb fields of the ions and it may be confused with the satellites if its intensity is comparable to satellite intensities. One might also see only a single satellite if the field frequency is close to the energy separation of the 4D and 4F levels; then the near satellite will be buried in the "wings" of the allowed line. For these reasons we emphasize that unless the features of the spectrum are clearly identifiable, extreme caution must

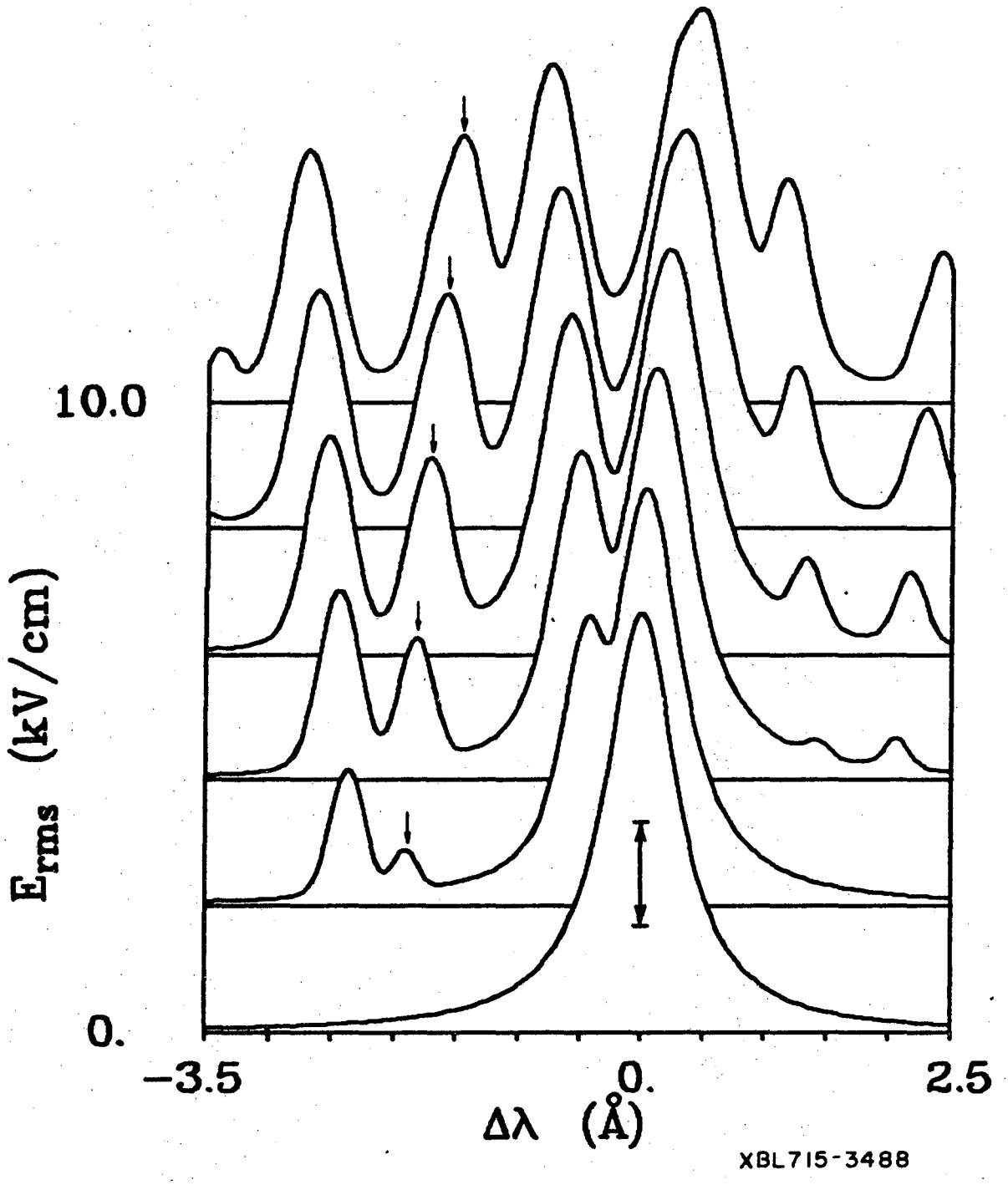

Fig. 3-5. For legend, see page 50a.

Fig. 3-5. Calculated (instrument-broadened) Stark profiles in the vicinity of the 4922-Å spectral line of He I for the case of no magnetic field and a linearly polarized electric field of frequency 4.0 cm^{-1} and for various electric field strengths, all for direction of observation perpendicular to $\vec{E}$. Each profile is plotted logarithmically; a single decade is shown by the double-ended arrow. $\Delta\lambda = 0$ is the unperturbed position of the allowed line $4\,^1D \rightarrow 2\,^1P$ and the single-ended arrow denotes one of its satellites.

be observed in using the perturbation calculations or Figs. 3-3 and 3-4.

The amplitude of the electric field can also be determined by measuring the Stark shift of the lines.[14] It is usually most convenient to measure the total Stark shift, which we define as the change in the separation of the forbidden and allowed lines (compared with their separation with no external fields). The Stark shift of the allowed line can also be used if one can determine its unshifted position. For low fields Eq. (2.48) can be used to find the Stark shifts; for high fields the theory of Chapter II must be used. From Eq. (2.48) we can see that for linear polarization the Stark shift is proportional to

$$1/(\omega_{ij}'^2 - \omega^2),$$

and therefore for $\omega < |\omega'_{ij}|$ it is a rather weak function of the frequency. In this case, a precise knowledge of the frequency is unnecessary; for other polarizations, however, the dependence of the Stark shift on the frequency is stronger.

C. Hydrogen Calculations

One can approach the calculation of hydrogen spectral profiles in the presence of a high-frequency electric field on either of two levels of sophistication. The first and simplest approach is to assume that the energy levels corresponding to the same principal quantum number 'n' are degenerate. Then, following the discussion of Chapter II.C [Eq. (2.32) and following], one chooses for the unperturbed eigenstates used to

calculate the matrix elements for Eq. (2.12), the particular set which satisfies

$$\langle i|E\cdot r|i'\rangle = \Delta_i \delta_{ii'}, \tag{3.9}$$

$$\Delta_i \equiv \frac{eE_0}{\hbar\omega}\langle i|r_E|i\rangle,$$

where r_E is the component of $\vec{r}$ parallel to $\vec{E}$, and where i and i' correspond to different eigenstates of the same principal quantum level. The profile of a spectral line arising from an optical transition between the eigenstates of two different principal quantum levels can then be found by summing Eq. (2.35) over the final states (k) and averaging over the initial states (i):

$$dA = \sum_{i,k} dA_{ik} \propto \sum_{i,k} |\xi_i^k|^2 \sum_{s=-\infty}^{\infty} \omega_\gamma \delta(\omega_\gamma - \Delta\omega - s\omega) J_s^2(\Delta_{ik}), \tag{3.10}$$

where we have assumed, following the discussion of Chapter II.D, that the initial states are equally populated. Equation (3.10) implies the usual Blochinzew type spectral pattern[18] composed of satellites spaced at integral values (denoted by s) of the electric field frequency from the unperturbed spectral line position ($\omega_\gamma = \Delta\omega$), and with intensities given in terms of Bessel functions. Each term in the sum of Eq. (3.10) corresponding to a given initial state i and a given final state k implies an entire spectrum of satellites with a 'characteristic width' which increases proportionally to the electric field strength E_0. We can see this by noting that $J_s(\Delta_{ik})$ as a function of s has the property that it is relatively constant for $s < \Delta_{ik}$ and falls off rapidly

to zero for $s > \Delta_{ik}$.[18] Defining the width w_{ik} to be two times the separation of the unperturbed line position and the position of the satellite (with corresponding $s = \bar{s}$) where this rapid decrease occurs for a particular i and k yields:

$$w_{ik} = 2\bar{s}\omega = 2\Delta_{ik}\omega = \frac{2eE_0}{\hbar\omega}\left(\langle i|r_E|i\rangle - \langle k|r_E|k\rangle\right), \tag{3.11}$$

and hence the width is proportional to E_0 with the proportionality constant a function of the particular initial and final state. For the entire profile we can define the average width $\bar{w}$ by averaging w_{ik} over the entire set of initial and final states. The result

$$\bar{w} = \sum_{i,k} |\xi_i^k|^2 w_{ik} \tag{3.12}$$

will also be proportional to E_0 and hence, even if one cannot resolve the individual satellites of the spectral pattern, one can still use the width of the spectral profile to measure the electric field strength. This method has been exploited by several authors.[22-25] The determination of the electric field frequency, however, does require the observation of the various satellites of the spectral pattern. It should be noted that the proportionality constant in Eq. (3.11) can be zero, in which case that particular component of the spectral profile does not contribute to an increase in broadening of the total profile with an increase in the electric field strength. In using the width

of spectral profiles for which this is the case (H_α, H_γ, H_ϵ, etc.) to measure the electric field strength, one must be careful to correct for such unshifted components. One further property of the spectral profile implied by Eq. (3.10) should be noted: if the electric field strength and frequency are scaled together, i.e., if we set

$$\omega' = \epsilon\omega$$

$$\text{and} \qquad E_0' = \epsilon E_0, \tag{3.13}$$

then the satellite intensities are unchanged, but the width of the satellite pattern is increased or decreased, depending on whether $\epsilon > 1$ or $\epsilon < 1$. This scaling property implies that a calculation performed for a particular frequency is really more general since it also applies to other frequencies and electric field strengths as given by Eq. (3.13).

Profiles calculated from Eq. (3.10) for an electric field frequency of 1.17 cm^{-1} and for several electric field strengths are shown in Figs. 3-6 and 3-7 (H_α and H_β, respectively). As in the previous section, we have assumed that (1) there is no magnetic field present, (2) the high-frequency electric field is linearly polarized in the $\hat{z}$ direction, and (3) the spectral profile is viewed in the direction perpendicular to the high-frequency field. The profiles have been calculated by folding at the expected satellite positions an appropriately normalized instrument function of the type of Eq. (3.8). The profiles have been plotted, as in Chapter III.B, lined up behind each other

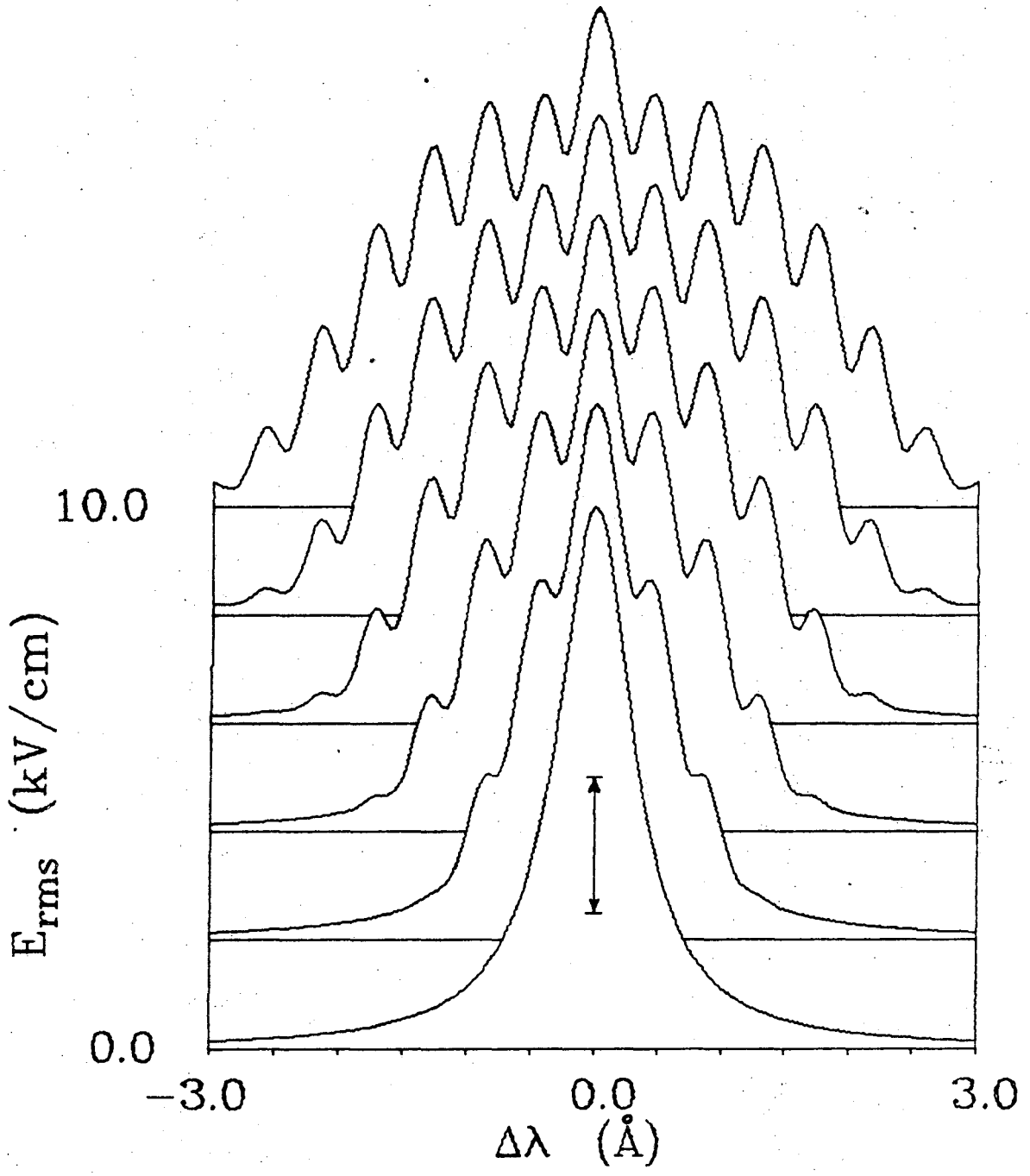

XBL 7311-1484

Fig. 3-6. Calculated Blochinzew Stark profiles in the vicinity of H_α for the case of no magnetic field and a linearly polarized electric field of frequency 1.17 cm^{-1} and for various electric field strengths, all for direction of observation perpendicular to $\vec{E}$. Profiles are plotted similarly to those in Fig. 3-2.

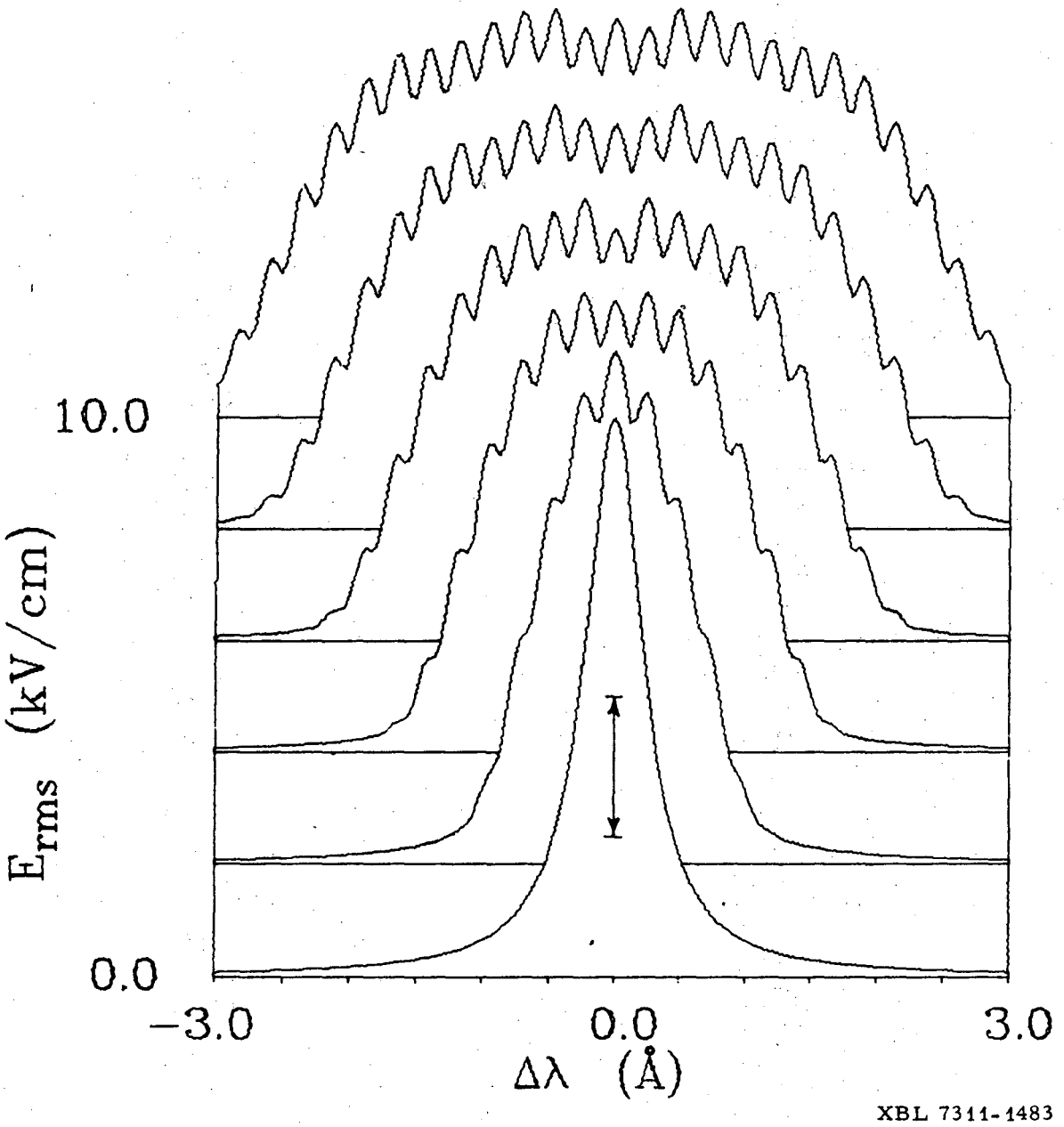

Fig. 3-7. Calculated Blochinzew Stark profiles in the vicinity of H_β for the case of no magnetic field and a linearly polarized electric field of frequency 1.17 cm^{-1} and for various electric field strengths, all for direction of observation perpendicular to $\vec{E}$. Profiles are plotted similarly to those in Fig. 3-2.

with the intensity of each profile plotted logarithmically. Both sets of profiles show a broadening proportional to the electric field strength. For H_β the satellite intensities between the 'fall off' points remain reasonably constant in relative intensity with that intensity decreasing for increasing electric field strength (all profiles calculated in a single figure have the same area). However, for H_α the central component of the profile does not show a decrease as the electric field increases, showing that a significant contribution to its intensity is due to transitions for which $\Delta_{ik} = 0$. The other components of H_α do follow an intensity pattern similar to H_β. It should be noted that if the satellite pattern of H_α could not be resolved due to a wider instrument function then a measure of the half-width of the resulting profile would very likely given an erroneous value for the electric field strength since one would be measuring the width of the central unbroadened component of the spectral profile. This indicates that care must be taken in observing the entire profile before deducing the width used in calculating the electric field.

So far we have discussed only the degenerate case. In a more complete calculation, consideration must be given to shifts of the unperturbed energy levels which destroy the degeneracy. There are three primary sources of such energy shifts: a magnetic field, a dc electric field, and fine structure shifts of the energy levels due to spin-orbit coupling and a relativistic mass correction of the electron. We consider these in turn:

(1) For a finite magnetic field $\vec{B}$ the energy levels of hydrogen are shifted by an amount which depends on the magnetic quantum number m of the particular level:

$$\text{shift} = m \frac{e|\vec{B}|}{m_e c} .$$

One can distinguish two cases: $\vec{E}$ parallel to $\vec{B}$, and $\vec{E}$ not parallel to $\vec{B}$. In the first case the extension of the Blochinzew solution is trivial, since the eigenfunctions of L_E (the component of the angular momentum in the electric field direction) are also the eigenfunctions which satisfy Eq. (3.9). Hence the magnetic field just shifts the various patterns calculated for a particular i and k relative to the others but leaves the satellite intensities unchanged. The total pattern becomes more complicated but still simple to calculate. For the second case a coupling occurs between the <u>different</u> eigenfunctions satisfying Eq. (3.9) and the more general methods outlined in Chapter II must be used to calculate the satellite intensities and positions. We shall not consider this case further but instead the similar case presented by a dc electric field.

(2) For a finite dc electric field $\vec{E}_{dc}$, the energy levels of hydrogen are shifted from their unperturbed positions by an amount proportional to the dc electric field strength. We can again distinguish two cases: $\vec{E}_{dc}$ parallel to $\vec{E}$, and $\vec{E}_{dc}$ not parallel to $\vec{E}$. The first case is again trivial as the presence of a parallel dc electric field merely leads to a shift of the satellite pattern calculated for a particular initial and final

state but leads to no change in the intensity of the pattern. For the second case eigenstates which have different energies due to the dc Stark effect are coupled by the high-frequency electric field and we must use the general methods outlined in Chapter II to calculate satellite positions and intensities (in Ref. 28 the problem of the Lyman alpha spectral profile in the presence of a high-frequency electric field and a perpendicular dc electric field is solved using an entirely different method).

We will consider the special problem of $\vec{E}_{dc}$ perpendicular to $\vec{E}$: We choose $\vec{E}_{dc}$ to lie in the $\hat{x}$ direction, and then choose for the eigenstates [which will be used to evaluate the matrix elements $\beta_{jj'}$ in Eq. (2.12)] those for which the operator 'X' (corresponding to the spatial x coordinate) will be diagonal. The appropriate energy levels ω_j to use in Eq. (2.12) are then the dc Stark shifted energy levels:

$$\omega_j = \omega_0 + f_j n\omega_S,$$

where ω_0 is the unperturbed energy level, n is the principal quantum number, f_j is an integer which depends on the particular eigenstate, and ω_S is given by

$$\omega_S = \frac{3eE_{dc}a_0}{2\hbar} \tag{3.14}$$

where a_0 is the Bohr radius. With the matrix elements and energy levels determined, Eq. (2.12) can be solved numerically for the satellite intensities and positions in the manner outlined in

Chapter III.A. Before presenting the results of such calculations it is interesting to note that this case satisfies a scaling law similar to that for the simple Blochinzew case [i.e., Eq. (3.13)]. Namely, if we set

$$\begin{aligned} \omega' &= \epsilon\omega, \\ E_0' &= \epsilon E_0, \\ E_{dc}' &= \epsilon E_{dc}, \end{aligned} \tag{3.15}$$

then Eq. (2.12) has the solution

$$\begin{aligned} \omega' &= \epsilon\omega, \\ C_{js}' &= C_{js}, \end{aligned}$$

i.e., the spectral pattern is unchanged except for a change in scale.

In Figs. 3-8a to 3-8d we present numerically calculated profiles for H_α, and in Figs. 3-9a to 3-9d we present similarly calculated profiles for H_β. In both cases the high-frequency electric field (frequency 1.17 cm^{-1} and field strength 5.0 kV/cm, 3.54 kV/cm rms) was assumed to be in the $\hat{z}$ direction. The different figures correspond to different assumed values of the dc electric field strength: E_{dc} = 0.0, 1.0, 2.5, 5.0 kV/cm; the direction of the dc electric field was assumed random but confined to the plane perpendicular to the high-frequency electric field. The direction of observation was perpendicular to the high-frequency electric field. The instrument function used to produce the figures had a full-width at half-maximum of 0.2 cm^{-1}

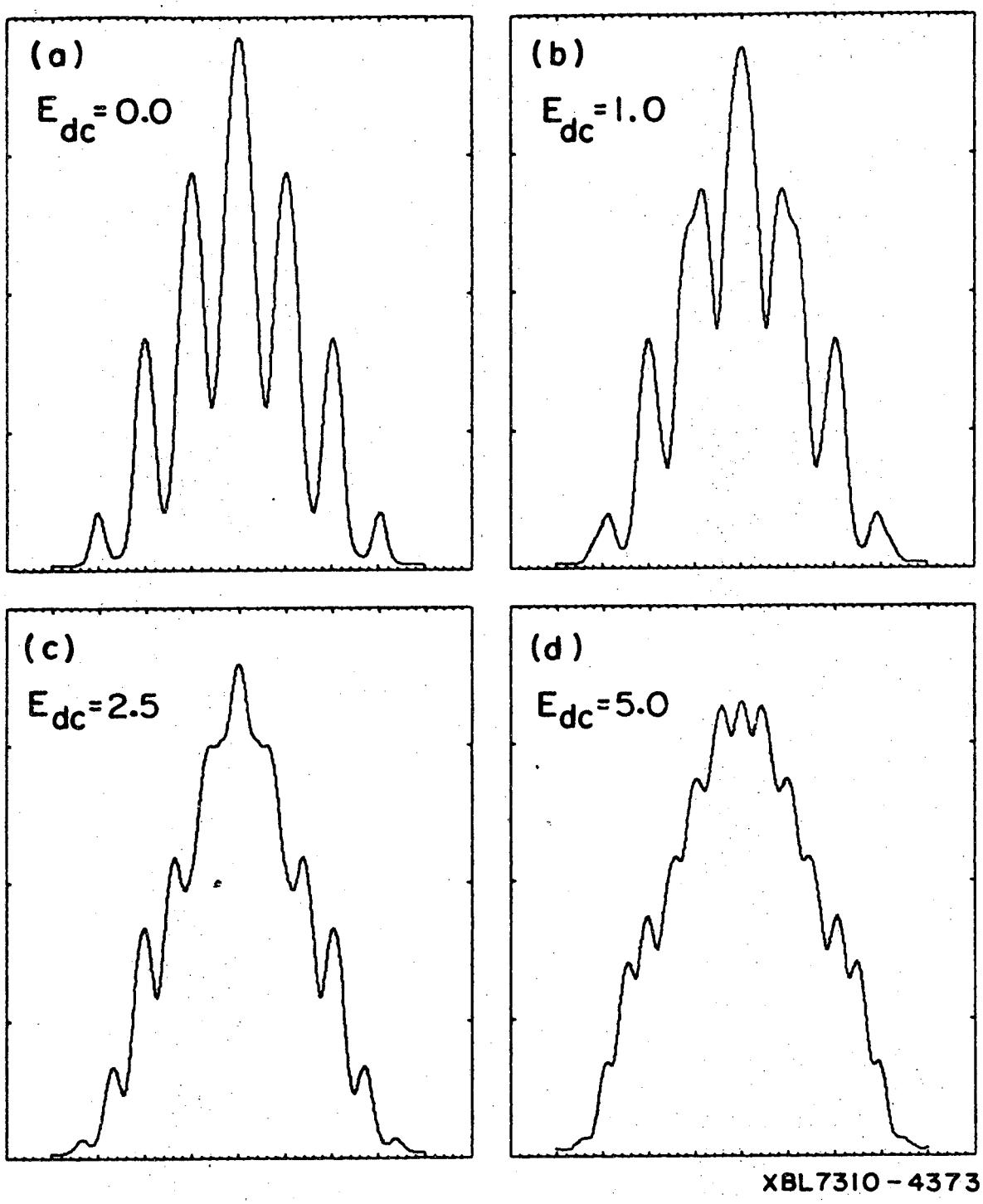

Fig. 3-8. For legend, see page 61a.

Fig. 3-8. Calculated Stark profiles in the vicinity of H_α for the case of no magnetic field, a linearly polarized high-frequency electric field of frequency 1.17 cm^{-1} and field strength 3.54 kV/cm rms, and for various dc electric fields (as noted, in kV/cm). Along the horizontal axis in each figure, one large division (= 5 small divisions) equals 0.5 Å.

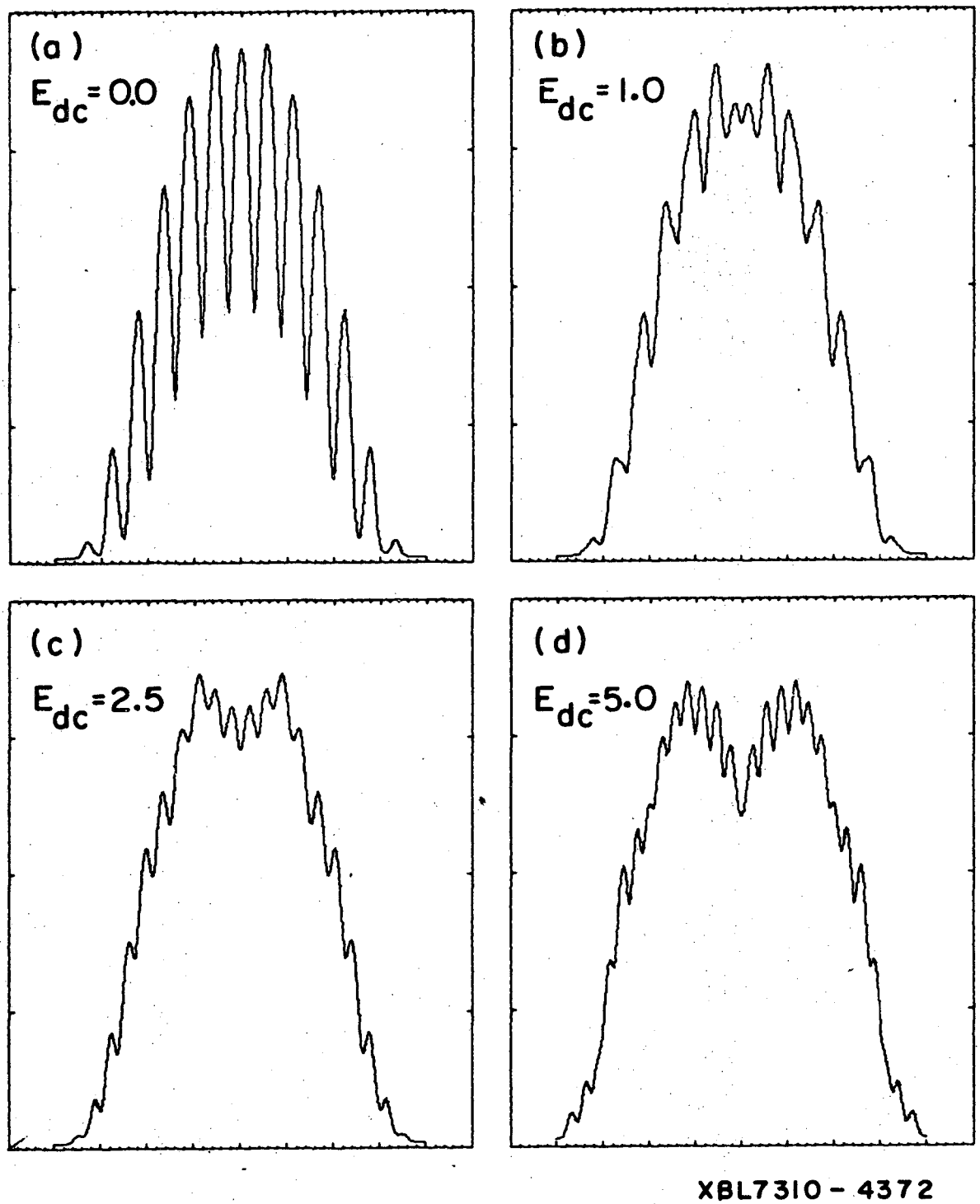

Fig. 3-9. For legend, see page 62a.

Fig. 3-9. Calculated Stark profiles in the vicinity of H_β for the case of no magnetic field, a linearly polarized high-frequency electric field of frequency 1.17 cm^{-1} and field strength 3.54 kV/cm rms, and for various dc electric fields (as noted, in kV/cm). Along the horizontal axis in each figure, one large division (= 5 small divisions) equals 0.5 Å.

and was then 'Doppler broadened' for a temperature of 0.4 eV ($440^{\circ}K$).

In discussing these figures it is useful to refer to Table III-2 which contains calculated values of ω_s for the various energy levels involved in the transitions leading to H_α and H_β. For weak electric field strengths the separation of the energy levels will be small and we expect the calculated profiles to nearly approximate the Blochinzew profiles shown in Figs. 3-8a and 3-9a. The meaning of 'small' in this context was discussed in Chapter II.G where the condition for a nearly hydrogen-like (i.e., degenerate energy level) solution was found to be Eq. (2.50) :

$$\omega_j - \omega_{j'} \ll \omega. \tag{3.16}$$

Referring to Table III-2, we see that this condition should be satisfied for both the initial and final energy levels for the case shown in Fig. 3-8b (H_α, $E_{dc} = 1.0$) and to a lesser extent for the case shown in Fig. 3-9b (H_β, $E_{dc} = 1.0$). These two figures bear out this assertion: The Blochinzew pattern is essentially maintained with the presence of the dc electric field leading to a broadening of the individual satellites due to a relative shift of the energy levels. The effect of increasingly higher electric fields can be observed by comparing successive figures. As can be seen by comparing Figs. 3-8a to 3-8c, the primary effect of a moderate dc electric field (i.e., one for which $\omega_j - \omega_{j'} < \omega$) appears to be a shift of the components which

Table III-2. DC Stark shift (ω_S) in inverse centimeters for n = 1 to 4 and for various electric field strengths in kV/cm.

n	ω_S (E_{dc} = 0.0)	ω_S (E_{dc} = 1.0)	ω_S (E_{dc} = 2.5)	ω_S (E_{dc} = 5.0)
1	0.0	0.0	0.0	0.0
2	0.0	0.13	0.32	0.64
3	0.0	0.19	0.48	0.96
4	0.0	0.26	0.64	1.28

make up a Blochinzew satellite. This can best be seen by observing the effect of the increasing electric field on the satellites which in Fig. 3-8a lie on either side of the main peak. In Fig. 3-8b these satellites have become broadened into two nearly resolvable peaks, and for the electric field represented by Fig. 3-8c (2.5 kV/cm) the two components of each satellite have become widely separated, one of which is nearly unresolvable from the main peak. The sum intensity of the two components, however, can be seen to remain relatively constant. For the highest field case represented by Fig. 3-8d the profile has ceased to reflect the Blochinzew pattern. These figures indicate that measurement of the frequency of a high-frequency electric field using the satellite separations is made nearly impossible by a dc electric field which does not satisfy Eq. (3.16). The situation for the H_β profiles shown in Figs. 3-9b to 3-9d is even worse, as can be seen by referring to the values of ω_S for the appropriate upper levels and lower levels of the transition. For the weak electric field case shown in Fig. 3-9b the profile still remains essentially the Blochinzew pattern with the main change being the splitting of the central peak into two components of approximately half the intensity of the original peak. For the higher dc electric field cases shown in Figs. 3-9c and 3-9d the profiles have become very complicated and, in fact, have become dominated by the dc electric field, as can be seen by the prominent dip in the center of the profile, characteristic of the dc Stark profile of H_β.

It should be noted that the complicated appearance of these

profiles is in some extent due to the narrow instrument width chosen to display the profiles. A broader instrument function would tend to smooth out the profiles, which in some cases could facilitate the interpretation of the profiles. For instance, with a wider instrument function, the profile corresponding to that shown in Fig. 3-9b would closely approximate the Blochinzew pattern of Fig. 3-9a.

(3) Finally, we consider the effect of fine structure on high-frequency Stark spectral profiles. This problem is very similar to that of case 2. The hydrogen energy levels are shifted due to spin-orbit coupling and a relativistic mass correction to the electron. The fine structure shift in a given energy level is given by the expression:

$$\omega_F = \frac{Z^4\alpha^2}{2n^4}\left(\frac{3}{4} - \frac{n}{j + 1/2}\right) \times \text{Rydberg}, \qquad (3.17)$$

where α is the fine structure constant, j is the total angular momentum of the electron (including electron spin), and Z is the atomic number (for hydrogen Z = 1). The value of ω_F for the first four principal quantum levels of hydrogen is given in Table III-3. The relevant parameter for this discussion is not the absolute shift, but instead the relative shift between the different levels of a given principal quantum number (noted in the table as the 'maximum relative shift').

As can be seen by referring to Eq. (3.17) or the table, fine structure energy shifts decrease rapidly with increasing

Table III-3. Fine-structure shifts (ω_F) in inverse centimeters for n = 1 to 4.

n	j	ω_F (cm^{-1})	Maximum relative shift (cm^{-1})
1	1/2	-1.5	0.
2	1/2	-0.46	
	3/2	-0.09	0.37
3	1/2	-0.16	
	3/2	-0.054	
	5/2	-0.018	0.14
4	1/2	-0.073	
	3/2	-0.028	
	5/2	-0.013	
	7/2	-0.006	0.08

principal quantum number. For the particular frequency 1.17 cm^{-1} for which we have performed the calculations presented in this section, reference to Eq. (3.16) shows that the only energy level for which fine structure shifts are important in calculating the Stark profiles is n = 2, i.e., the lower level of the transitions H_α and H_β. Furthermore, a comparison of Table III-2 and Table III-3 shows that if a dc electric field of intensity greater than ~ 3 kV/cm is present, then its effect on the n = 2 energy levels is greater than that of fine structure. In the limit of a high electric field > 3 kV/cm one can, to a good approximation, ignore the effect of fine structure.

In Figs. 3-10a to 3-10d and 3-11a to 3-11d we show calculated profiles for which the fine structure has been included as well as an increasing electric field. To simplify the numerical calculations, we have assumed that the lower level is split only by the fine structure, and the upper level is only split by the dc electric field. The four figures in each set correspond to the assumed electric field values: E_{dc} = 0.0, 0.5, 1.0, and 2.5. For higher electric field strengths the dc electric field dominates the energy splitting of the lower level and the spectral pattern should more closely approximate those shown in previous figures. The first figure in each set shows the effect of fine structure alone on the spectral profiles: The different satellites are split into two components corresponding to the two different fine structure shifts. Finally, it should be noted that the effect of fine structure splitting is to produce asymmetric Stark profiles.

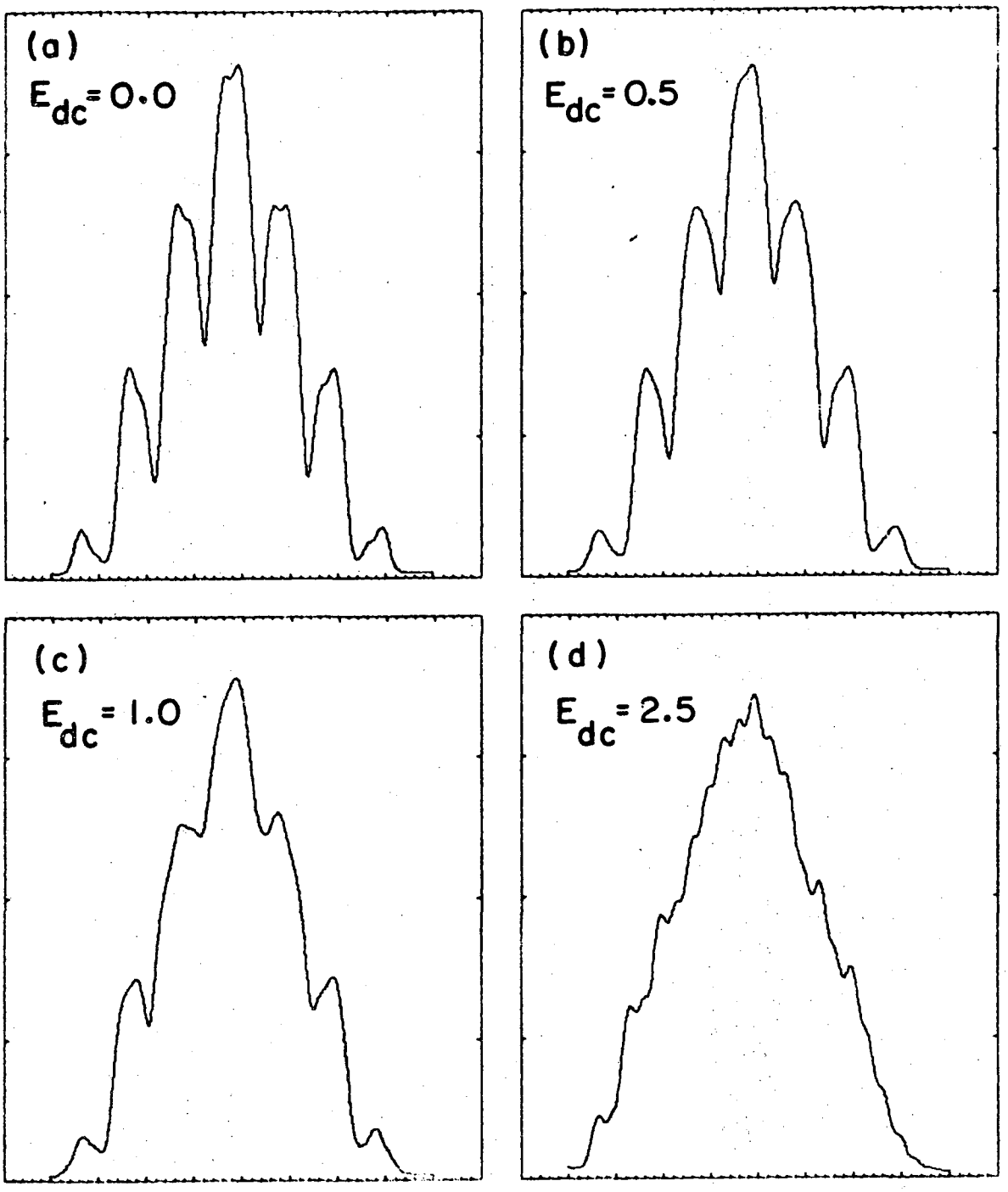

Fig. 3-10. For legend, see page 69a.

Fig. 3-10. Calculated Stark profiles, including fine structure splitting of the lower level, in the vicinity of H_α, for the case of no magnetic field, a linearly polarized high-frequency electric field of frequency 1.17 cm^{-1} and field strenth 3.54 kV/cm rms, and for various dc electric fields (as noted, in kV/cm). Along the horizontal axis in each figure, one large division (= 5 small divisions) equals 0.5 Å.

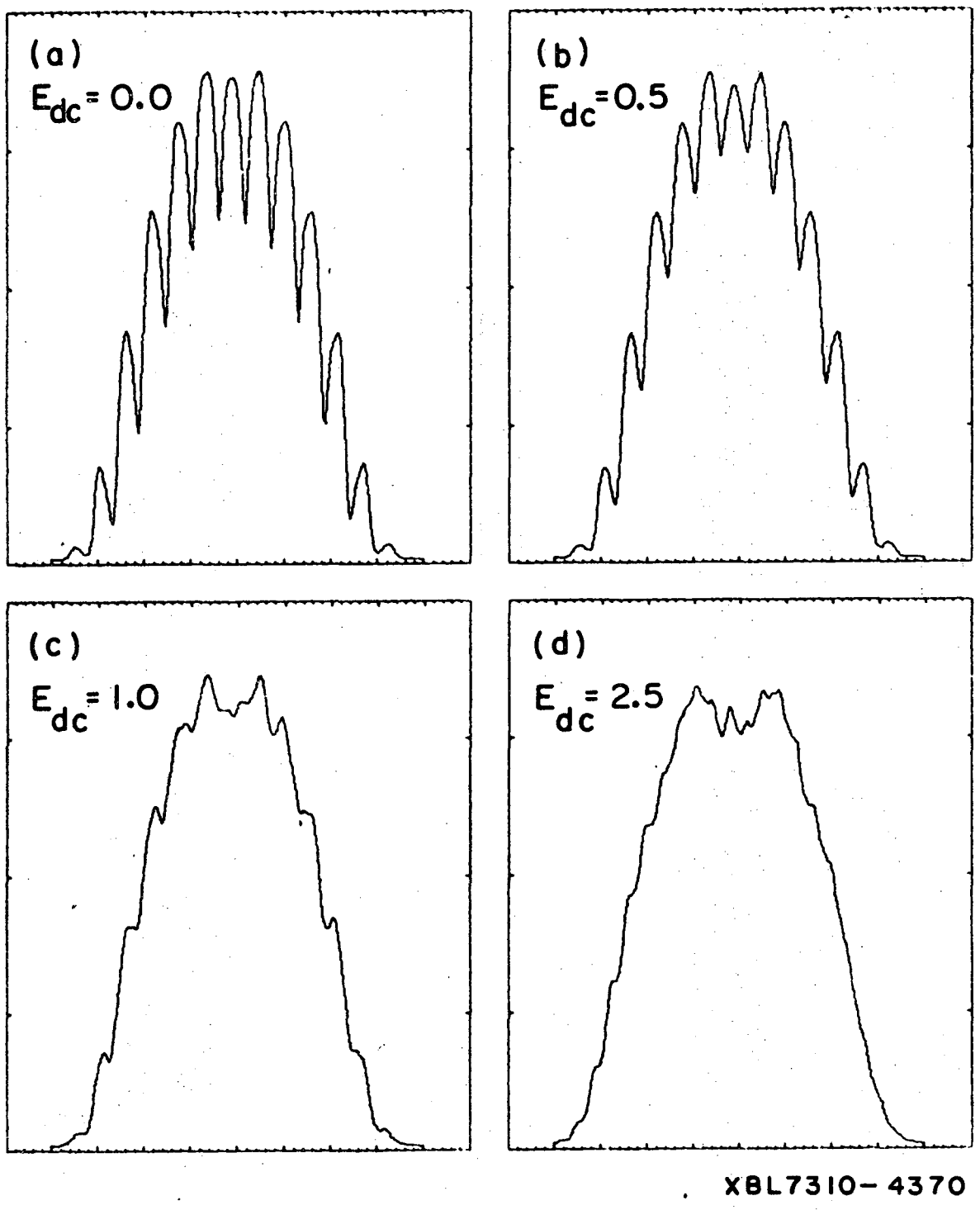

Fig. 3-11. For legend, see page 70a.

Fig. 3-11. Calculated Stark profiles, including fine structure splitting of the lower level, in the vicinity of H_β, for the case of no magnetic field, a linearly polarized high-frequency electric field of frequency 1.17 cm^{-1} and field strength 3.54 kV/cm rms, and for various dc electric fields (as noted, in kV/cm). Along the horizontal axis in each figure, one large division (= 5 small divisions) equals 0.5 Å.

IV. EXPERIMENTAL APPARATUS

Figure 4-1 shows the apparatus used in the experiment. We generate the high-frequency electric field in a cylindrical microwave cavity and apply it to a plasma produced by a dc discharge in a quartz capillary which threads the axis of the cavity. The cavity (0.609 cm in diameter and 0.865 cm in length) is excited by a 10 W cw Elliott-Litton Model 8TFK9 Klystron and oscillates in the TM_{010} mode with the electric field parallel to the axis of symmetry and electric-field strength maximum along the axis of the cavity. Mode identification was verified by calculating the resonant frequency of cavity plus quartz capillary, which agreed to within 1% with the measured frequency of 35.2 GHz, and also by measuring the relative electric field intensity as a function of position along the axis of the cavity. This latter measurement was done by measuring the change in resonant frequency of the cavity-quartz capillary system as a small quartz plug was pushed into the cavity down the inside of the quartz capillary. The calculated electric field intensity variation over the inside cross section of the capillary (o.d., 0.85 mm; i.d., 0.40 mm) is $< 5\%$ of the value on the axis.

In operation with a plasma, gas flow is maintained continuously through the capillary: Typically, the pressure at the high-pressure end of the capillary is 3 Torr, and the pressure at the low-pressure end is 1 Torr. Other typical dicharge parameters are current, 3.5 mA, i.e., current density, 2.7 A/cm^2; and electron density, 2×10^{11} cm^{-3}. The electron density is

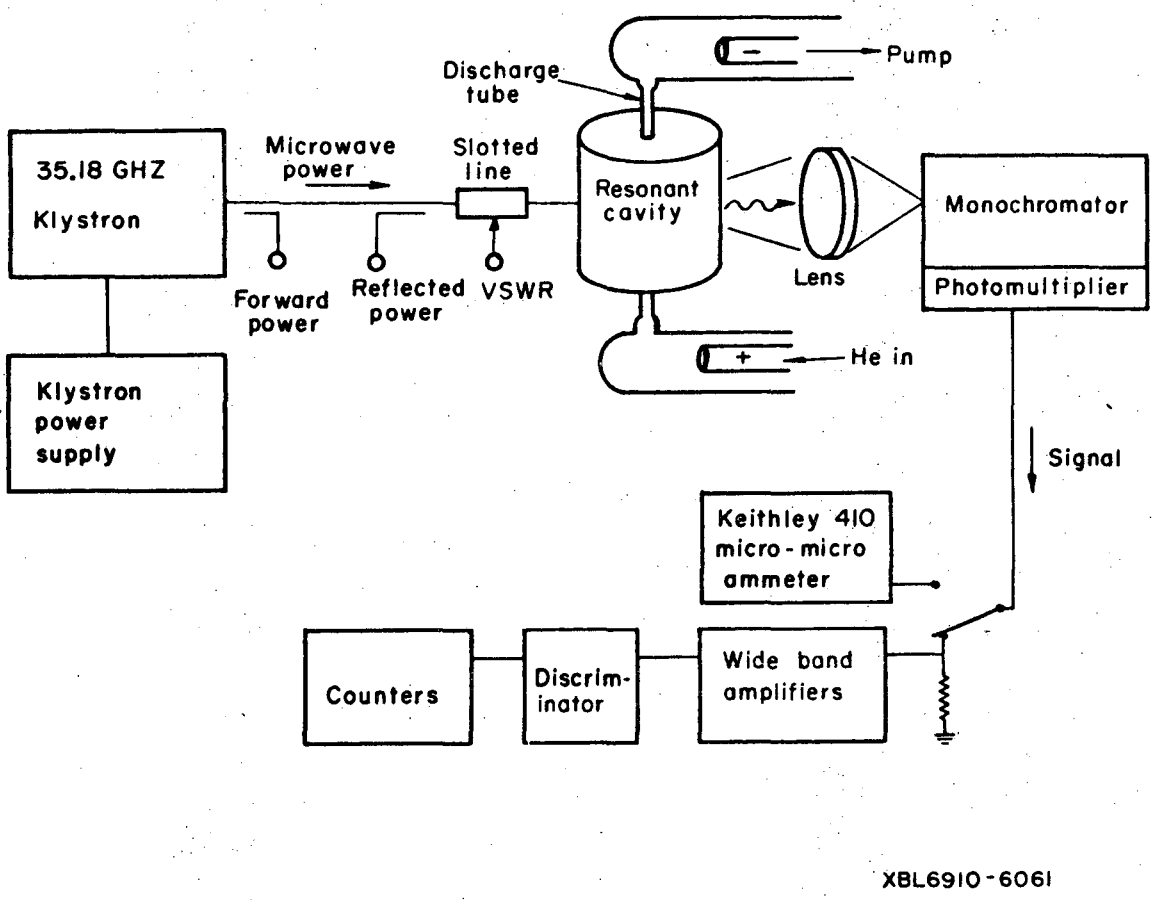

Fig. 4-1. Schematic diagram of the experiment.

determined by measuring the change of resonant frequency of the microwave cavity due to the presence of the plasma. The field frequency is much greater than either the plasma frequency or the electron collision frequency, so that the microwave field has no noticeable effect on the plasma other than stimulating otherwise forbidden multi-quantum transitions.

Light emitted by the discharge in a direction perpendicular to the electric field direction is viewed through a small slit in the microwave-cavity wall, spectrally resolved using a Jarrel-Ash Co. Model 82-000 0.5-meter monochromator, and photoelectrically detected, using an uncooled EMI 6256-S photomultiplier. For fine spectral line measurements the observed wavelength can be set to an accuracy of $\lesssim 0.01$ Å (maximum tuning range ~ 10 Å) by tilting a micrometer-adjusted quartz plate placed on the grating side of the exit slit of the monochromator. Light intensity at a given wavelength is measured by use of standard photon counting techniques. Peak intensities for the strongest lines measured represent 10^4 to 10^5 counts/sec.

V. EXPERIMENTAL RESULTS

A. Comparison of Theory and Experiment for Neutral Helium Lines

We have experimentally studied the effect of a linearly polarized high-frequency electric field on eigenstates of He I by observing optical transitions in the vicinity of three allowed lines, which we will refer to as

case I: 4922 Å (4^1D, etc. - 2^1P),

case II: 4388 Å (5^1D, etc. - 2^1P),

case III: 4144 Å (6^1D, etc. - 2^1P),

and by comparing the observed spectrum with the spectrum calculated by using the methods of Chapters II and III. In all cases there is no magnetic field. Figures 3-1 and 3-2 show the theoretical profiles predicted by the multilevel theory of Chapter II for cases I and II for the experimentally measured electric field frequency and for various field strengths.

For a direct comparison of the theoretical calculations with our measured line profiles, we have folded the theoretical results, which consist of a discrete line spectrum, with a realistic "instrument function" obtained from measurements taken on the same apparatus but with microwave power turned off. Discussion of the instrument function is given in Appendices D and E. Figures 5-1 and 5-2 show comparisons of experimental results with various theories, all calculated for observation at right angles to the direction of the electric field and for a peak field strength

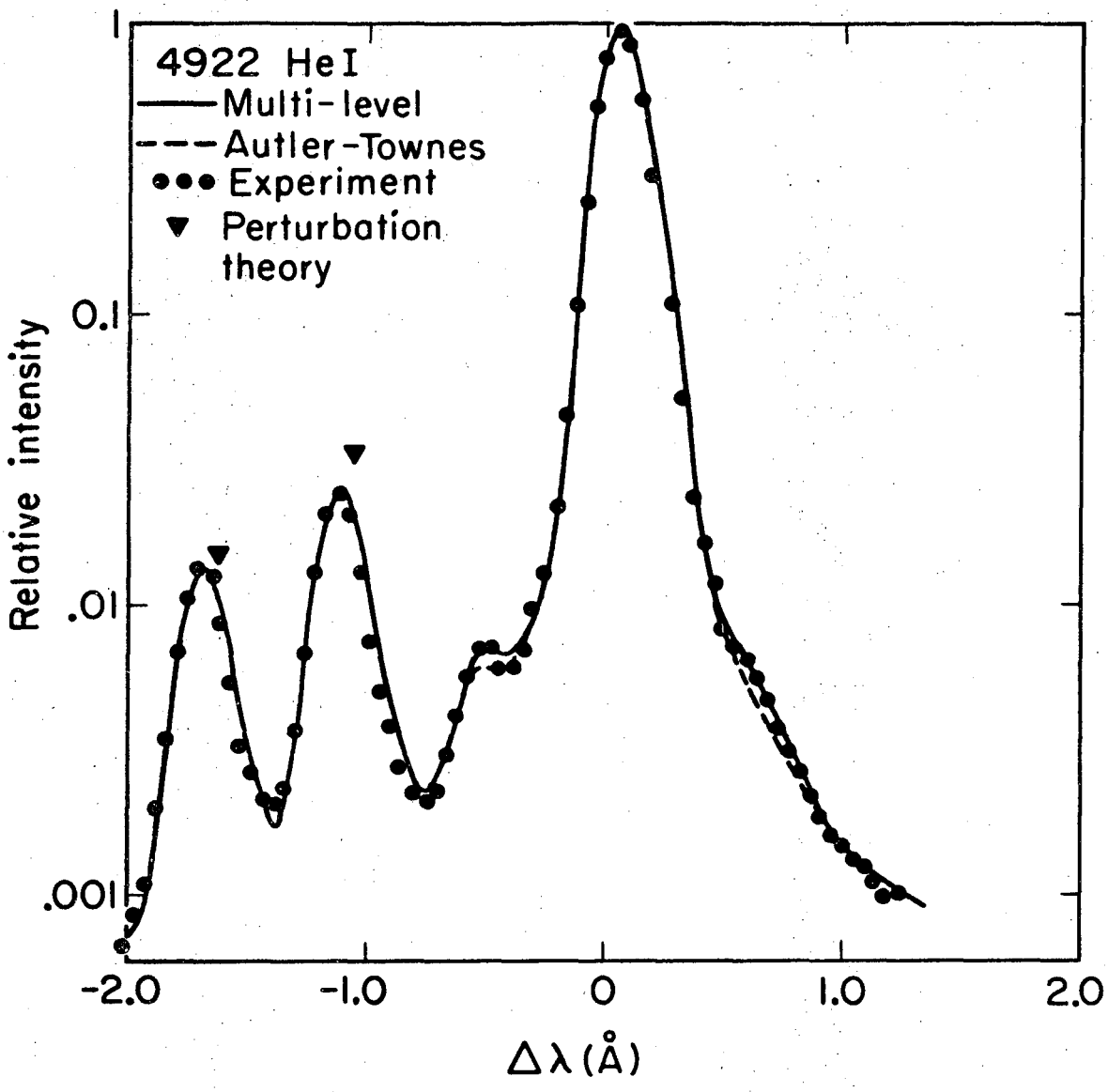

XBL703-2461A

Fig. 5-1. For legend, see page 75a.

Fig. 5-1. Comparison of experiment and various theories for case I (4^1D, etc. $\rightarrow 2^1P$), 4922-Å He I for the case of no magnetic field and a linearly polarized electric field of frequency 1.17 cm^{-1}, and for direction of observation perpendicular to the electric field.

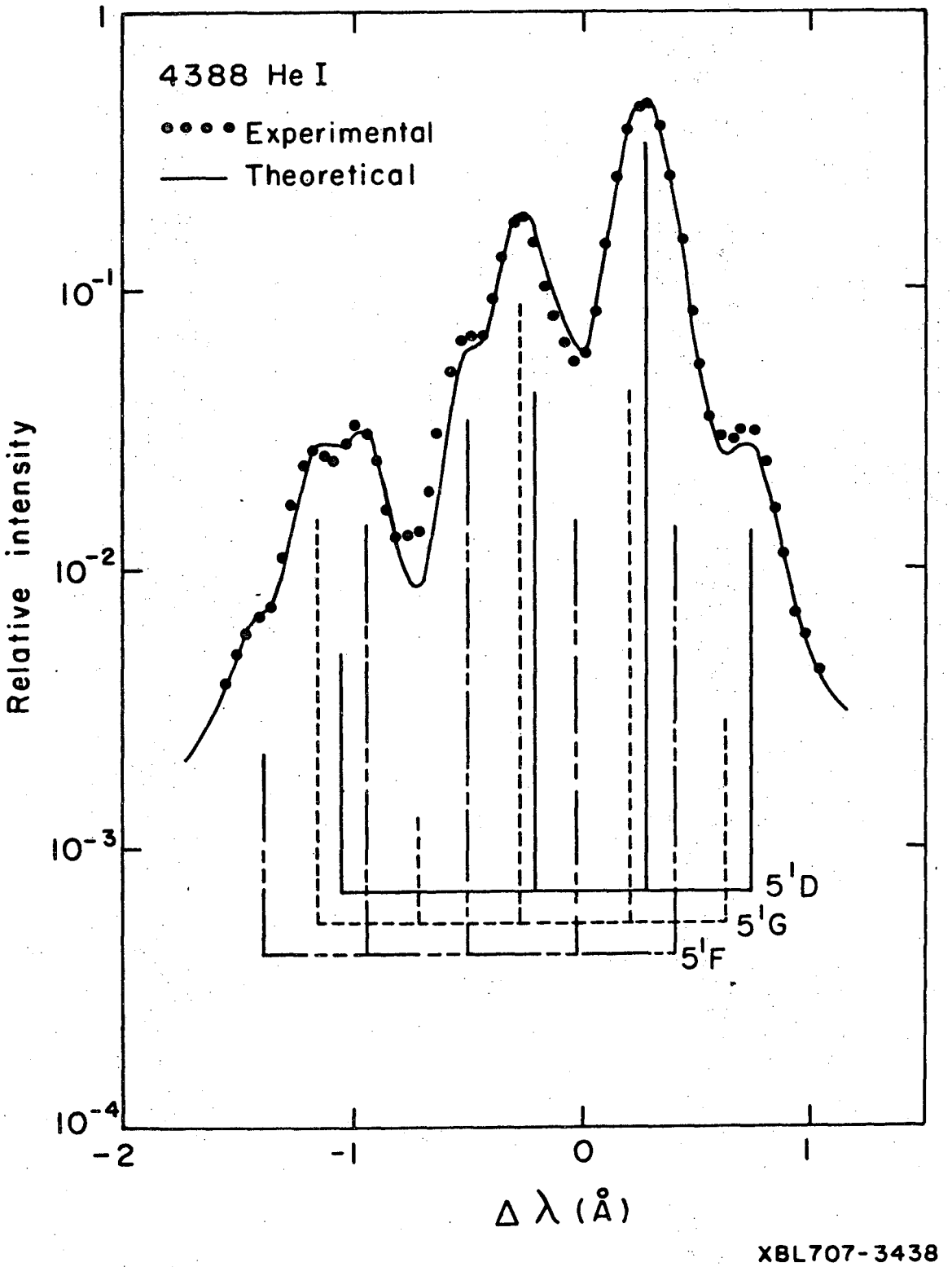

Fig. 5-2. For legend, see page 76a.

Fig. 5-2. Comparison of experiment and various theories for case II (5^1D, etc. $\rightarrow 2^1P$), 4388-Å He I for the case of no magnetic field and a linearly polarized electric field of frequency 1.17 cm^{-1} and rms electric field strength of 3.54 kV/cm, and for direction of observation perpendicular to the electric field. The sets of vertical lines labeled 5^1D, 5^1F, and 5^1G indicate the positions and relative intensities of spectral components originating from those levels.

of 5.0 kV/cm (3.54 kV/cm rms). In all cases $\Delta\lambda = 0$ is the position of the allowed line in the absence of the perturbing electric field. All "bumps' on the theoretical profiles are produced by one or more satellites and not by irregularities in the instrument function. All satellites stronger than 10^{-5} of the total intensity of the pattern were retained in the calculations (the number of satellites so kept is noted in the discussion of each figure).

Figure 5-1 shows a comparison between experimental and theoretical results for case I. The multilevel theory outlined above, the Autler-Townes theory, and the perturbation theory of Barranger and Mozer all give nearly the same results for the predicted spectrum; the major discrepancy between them comes from the neglect of the Stark shift in the perturbation calculation. The slight difference between the Autler-Townes and the multilevel theories is due to the retention of the 4P energy level in the latter. For both the multilevel and the Autler-Townes calculations we have included 18 satellites. Agreement of multilevel theory with experiment is excellent, and even the other two theories agree quite well with experiment for this field strength and frequency (note that agreement between experiment and perturbation theory would be substantially improved by including the lowest order correction to the Stark shift, Eq. (B9) in Appendix B, in calculating the relative position of the far and near satellites and the allowed line).

Case II, shown in Fig. 5-2, is a much more severe test of

the various theories owing to the following: (a) The matrix elements $\beta^{\pm}$ increase with n (principal quantum number), hence the effect of a given electric field is greater on the 4388-Å line than on the 4922-Å line. (b) The energy levels of n = 5 are closer together, so that more satellites (i.e., higher-order transitions) become important. (c) For n = 5 there is a G energy level very near the F energy level, and the two interact strongly.

In Fig. 5-2, we compare the measured line profile for the 4388-Å line with theoretical ones calculated from our multilevel theory and from the Autler-Townes theory, again using a field strength of 5.0 kV/cm. Agreement between the multilevel calculations and the measured data is very good, whereas experiment and the Autler-Townes calculations sharply disagree, not only in satellite positions and intensities but also in the Stark shift of the allowed line. This disagreement graphically illustrates the need to include additional upper levels, since this is the only significant different in the two theories. Perturbation calculations, not shown, disagree even more strongly with measurements. In the Autler-Townes calculation we have included 42 satellites; 58 were used in the multilevel calculations.

In Fig. 5-2 we have also indicated the major satellites originating from the three upper levels, 5^1D, 5^1F, 5^1G. Each vertical line in the figure corresponds to a "satellite" and denotes the average position and the sum intensity of the five components (one component arising from each magnetic quantum

level of the ^4D states: 0, ± 1, ± 2) comprising that satellite.

Case III, shown in Fig. 5-3, is an even stronger test of the multilevel theory than the first two cases. This arises for the same reasons given above in discussing He 4388 and because of the added presence of a new-high-angular momentum energy level not present in the prior case. For n = 6 the three highest-angular momentum energy levels, F, G, and H, have a total energy separation of 0.3 cm^{-1} (if the 6D level is included the total energy separation is 2 cm^{-1}) compared to the experimental frequency of 1.17 cm^{-1} and the electric field coupling constant $\beta^{\pm} \simeq 2$ cm^{-1} (for E_0 = 5 kV/cm). Thus these levels are strongly coupled to each other by the electric field and, following the discussion of Chapter II.G, could be described as hydrogen-like. Because of this strong coupling any theory which does not explicitly consider these levels (such as perturbation or Autler-Townes) would give results which were grossly in error.

Several features distinguish Fig. 5-3 from the previous figures. Firstly, this is the first example shown of measured data which has been fit using the least-squares fitting program PISA. The two previous figures for He 4922 and He 4388 were fit by hand by comparing the measured data with a set of calculated profiles at various field strengths and at the measured frequency. For this particular case, the frequency was fixed at the measured value and the program adjusted the electric field to give a best fit. The field strength so determined was 5.15 kV/cm. A second case in which PISA was allowed to fit the frequency as well as

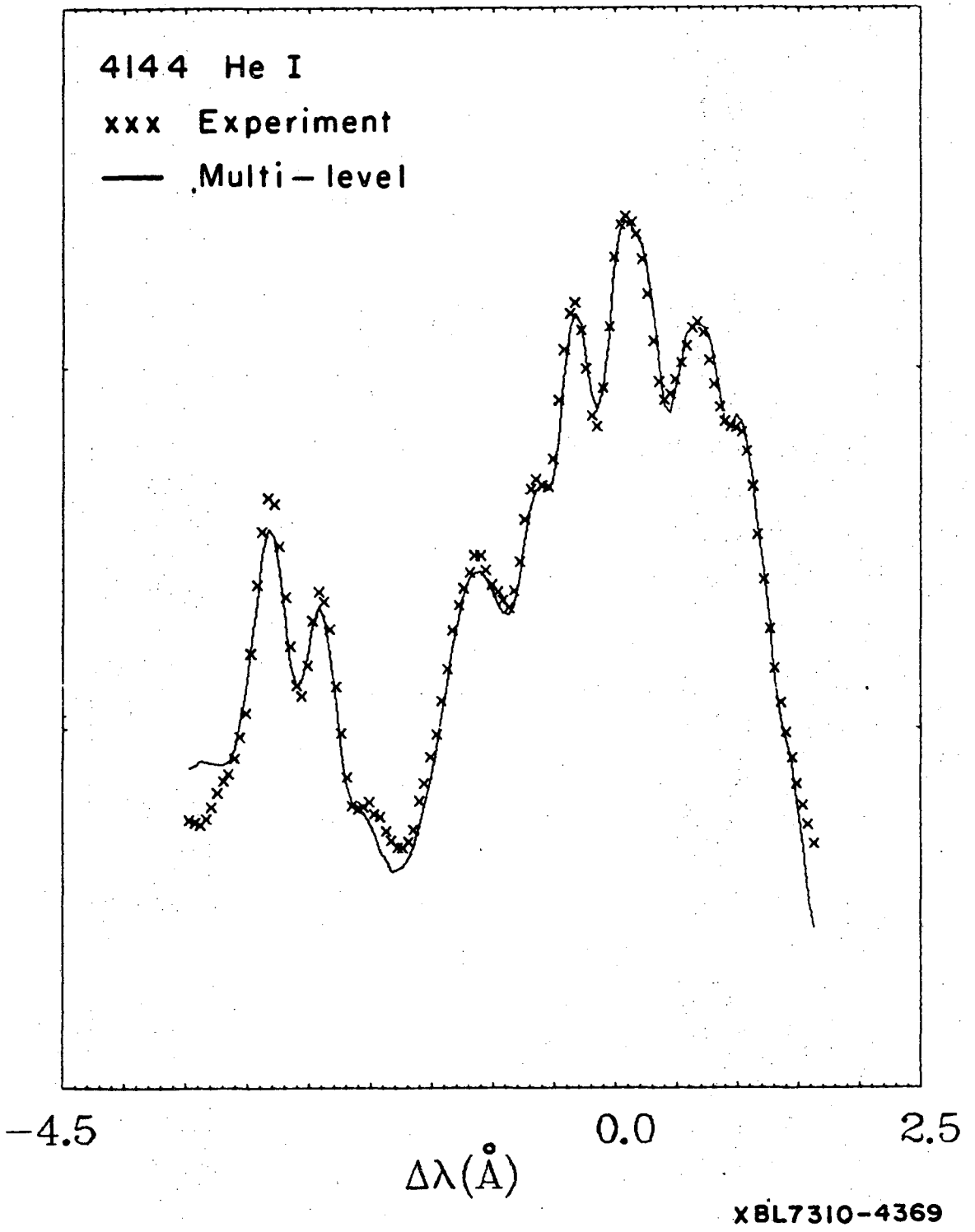

Fig. 5-3. For legend, see page 80a.

Fig. 5-3. Comparison of experiment and the multilevel theory for case III (6^1D, etc. $\rightarrow 2^1P$), 4144-Å He I for the case of no magnetic field and a linearly polarized electric field of frequency 1.17 cm^{-1} and rms-electric-field strength of 3.65 kV/cm, and for direction of observation perpendicular to the electric field.

the electric field did not give significantly different results, and has not been shown.

The second feature unique to this figure is the presence of satellites of the 6P - 2P transition. These two satellites which greatly resemble the 'usual' perturbation-type profile (i.e., two satellites separated by twice the field frequency) lie at the left of the figure and arise because of the coupling of the 6P energy level to the 6D energy level by the electric field. One deviation from the perturbation picture should be noted: For this particular field strength and frequency the far satellite is more intense than the near satellite and this reversal of the perturbation picture occurs in <u>both</u> the measured and the calculated results. Calculations show that this reversal in intensity ratio is an effect of the increasing electric field and at somewhat weaker field strengths the two satellites are given by the perturbation result, Eq. (2.49).

Finally, we note that if one ignores the two satellites arising from the 6P - 2P transition in Fig. 5-3 the remainder of the profile is remarkably symmetric, which is consistent with the discussion given in Chapter II.G and Chapter III.B.

In Fig. 5-4 (and Table V-1) we summarize the results of many measurements of neutral helium spectral profiles taken on the experimental apparatus of Fig. 4-1. The data are presented as a log-log plot of E_0 (the electric field in the discharge measured using the methods of Chapters II, III, and IV) vs the input

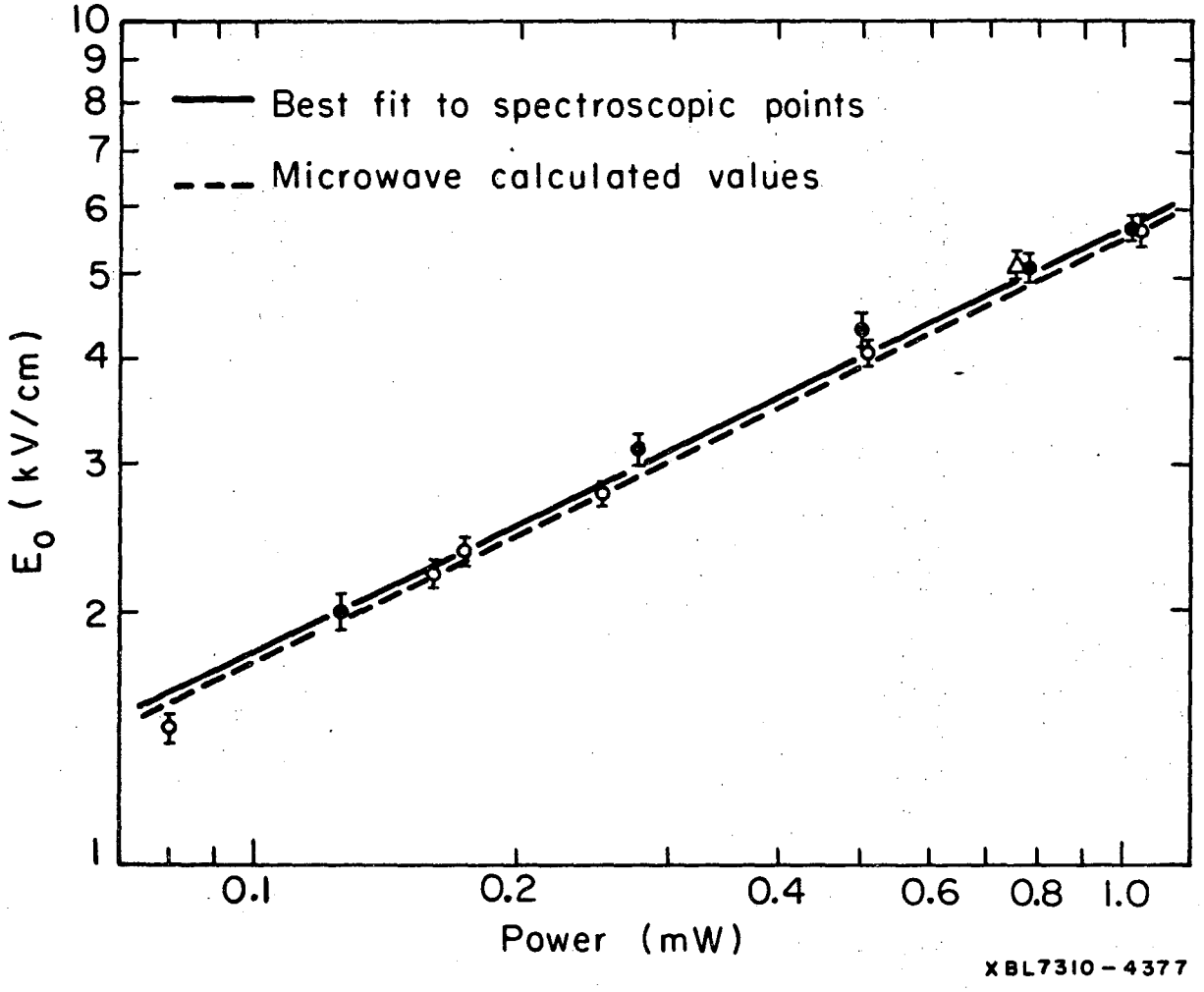

Fig. 5-4. A comparison of the electric field strength measured spectroscopically, with the calculated microwave-electric field in the cavity. The different symbols correspond to electric field data obtained from the spectral lines: ⏀, He 4922; ⏀, He 4388; and ⏃, 4144. Spectroscopic electric-field data is shown for a range of greater than ten in microwave power.

Table V-1. A comparison of electric field parameters measured spectroscopically versus electric field parameters measured using standard microwave techniques.

Line	Power[a] (mW)	Calculated E_0 (kV/cm)	Calculated Frequency (cm^{-1})	Method[b]	Measured Frequency[c] (cm^{-1})
He 4922	1.03	5.65±.15	1.17±.01	S	1.163
He 4922	0.78	5.10±.20	1.18±.01	S	1.173
He 4922	0.50	4.30±.20	1.15+.01	S	1.166
He 4922	0.28	3.10±.15	1.15±.01	S	1.166
He 4922	0.13	2.00±.10	1.16±.01	S	1.166
He 4388	1.04	5.62±.10	1.18±.01	P	1.163
He 4388	0.51	4.04±.10	1.19±.01	P	1.163
He 4388	0.25	2.78±.05	1.14±.01	P	1.163
He 4388	0.17	2.37±.05	1.13±.01	P	1.163
He 4388	0.16	2.23±.05	1.14±.01	P	1.163
He 4388	0.08	1.45±.06	1.15±.01	P	1.163
He 4144	0.76	5.15±.10	1.17±.01	C	1.166

[a]Power measured at the Hewlett-Packard power meter--power at cavity is found by multiplying value shown by 6604.

[b]Methods: 'S', E_0 found from measured intensity of far and near satellites relative to that of the allowed line using Table III-1, and frequency from the separation of the far and near satellites; 'P', both E_0 and frequency found from least-square fit

of measured profile using PISA; 'C', E_0 found by PISA (setting frequency equal to measured frequency), frequency found from separation of far and near satellites of the 6P - 2P transition.

[c] Measured using cavity wavemeter; values varied due to use of different Geissler tubes.

microwave power into the cavity. This latter was measured on a Hewlett-Packard 431C power meter by using a directional coupler to monitor a small portion of the forward microwave power. This reading was then adjusted to give the value at the cavity by correcting for microwave losses in the waveguide and the attenuation of the directional coupler.

Before discussing the figure itself, we will briefly review how E_0 was obtained:

(1) A scan of the profile on one of the spectral lines: He 4922, He 4388, or He 4144 was taken using the 'tiltable' quartz plate method described in Appendix D.

(2) Before and after the scan the following reference data were taken: the dark current of the photomultiplier tube and a short scan (about 5-6 points) of some reference peak--usually the peak of the profile itself.

(3) The reference data were then used to correct for position drifts and for systematic intensity variations that occurred during the scan, and to subtract out the dark current contribution of the measured intensity.

(4) The intensity data were also corrected for systematic variations due to the quartz plate, and for 'dead time' losses of the scalars and the discriminator.

(5) The position scale which was measured using a micrometer was converted to a wavelength scale by referring to Fig.D-4 for the appropriate conversion factor.

(6) This corrected experimental profile was then compared

to a theoretical profile and E_0 (and also the frequency) extracted using one of the following methods:

(a) For helium 4922, the intensities of the far and near satellites of the forbidden line were calculated by subtracting the wing intensity of the allowed line at each satellite peak position from the measured peak intensity. The ratios, S_+ and S_-, were then determined, and E_0 calculated from data similar to Table III-1. The frequency was determined from the separation of the two satellites.

(b) For He 4388 and He 4144, PISA (see Appendix G) was used to vary the electric field strength and frequency until a best fit in the least-squares sense was obtained. In each case the calculated profile used by PISA consisted of folding an appropriate instrument function with a satellite spectrum calculated using the methods of Chapters II and III.

The results calculated using either method (a) or (b) are displayed in Table V-1 and in Fig. 5-4. Each point represents a measurement of E_0 as described above. The figure includes measurements using three helium lines, 4922, 4388, and 4144, and over a range of input microwave power of 10 (or range of 3 in electric field strength). The upper limit represents the maximum power available from the present Klystron. The lower limit represents the lowest electric field at which electric field data could be reliably extracted from the optical data in this experiment. This limit arose from two factors. For the He 4922 line this limit represents the point at which the satellites become

'lost' in the wing of the allowed line and the continuum background. For He 4388 and He 4144 the satellite intensities should be relatively greater and should provide a method of measuring weaker electric fields. However, in this particular experimental setup the high dc ambipolar electric field in the discharge tube produces spectral lines at the positions of the normally forbidden transitions, $n^1F - 2^1P$, $n^1G - 2^1P$, which interfered with the satellites. These lines were particularly evident in profiles taken with the microwave power off and had to be numerically removed from the instrument profile before doing curve fitting. The effect of these normally forbidden lines on profiles taken at a high electric field strength ($\simeq$ 5 kV/cm) can be seen in Figs. 5-1 and 5-2, where the slight dip in the calculated profile (relative to the measured profile) at V $\simeq$ -1.4 Å for He 4922 and at $\simeq$ -0.8 Å for He 4388 almost certainly arise from the neglect of the forbidden line intensity in the calculations.

The data presented in Fig. 5-4 show the expected linear dependence of E_0 on the square root of the microwave power, i.e., all data points fall near a line of slope 1/2. (The solid line shown on the graph is the best such line in the least-squares sense. We can compare the optically derived value of E_0 with the electric field calculated using standard microwave techniques by referring to Eq. (C12). The microwave data are represented on the graph by the dashed line and lie 3.5% lower than the optical data.

B. Comparison of Theory and Experiment for Hydrogen Spectral Lines

We have also studied the effect of a high-frequency electric field on the hydrogen spectral lines: H_α, H_β, H_γ, and H_δ. The method used is similar to that described in the previous section for helium spectral lines: i.e., we compare spectral profiles measured as described in the previous section with profiles calculated as discussed in Chapter III. In all cases shown the calculated profiles have been fit to the measured profiles using PISA (Appendix G). Before presenting these comparisons as figures, two aspects of the hydrogen problem require further discussion.

In Chapter III.C we have presented two methods of calculating the high-frequency Stark effect of hydrogen profiles. The first was applicable if the energy levels of hydrogen could be considered degenerate, where the condition of degeneracy was given by Eq. (3.16). The second, and more complicated, method explicitly included non-degeneracy of the hydrogen energy levels due to a dc electric field and fine-structure splitting. For the purpose of the comparison shown in Figs. 5-5 to 5-8, we have chosen to use the simple Blochinzew theory to calculate the profiles. This choice requires some discussion. As noted in the discussion of Chapter III.C and also in Table III-3, fine-structure splitting can be ignored for the frequency of this experiment, 1.17 cm^{-1}, for all hydrogen energy levels except for the n = 2 energy level which forms the final state for the transitions corresponding to the Balmer lines studied in this section. The relative energy

shift produced by fine-structure splitting was 0.37 cm^{-1}, which was less than or comparable to the instrumental width of the spectrometer at the wavelengths of these lines. There was also a dc electric field, as discussed in Appendix E, due to ambipolar diffusion of the electrons and ions to the walls of the quartz capillary. This field had an average intensity of ~ 0.6 kV/cm as measured from the Stark broadening of the lines H_γ and H_δ with the high-frequency electric field turned off. As can be seen by reference to Table III-2, for this electric field the splitting of the hydrogen energy levels is less than the corresponding splitting due to fine structure and hence is less than the instrumental width. We have used the above considerations to simplify the calculations in the following way. In producing profiles for comparison to the measured profiles, we have implicitly incorporated fine structure and a dc electric field (as well as Doppler broadening) not into the theory but, instead, into the instrument function as an additional broadening beyond the true instrumental broadening. We have done this by using the measured profile of each hydrogen spectral line taken with the high-frequency electric field turned off, as the 'instrumental' profile which is folded with the line spectrum calculated by the Blochinzew theory. Since the high-frequency electric field could influence the width of the instrument function determined in this way [for instance, it could affect (1) the ambipolar electric field or (2) the neutral temperature of the discharge and hence the Doppler broadening], we have allowed PISA to fit not only the usual electric field parameters (frequency, field strength) but also a parameter which varies the instrument width.

The results of using PISA to produce a least-square fit of hydrogen profiles calculated using the method above to measured profiles are shown in Table V-2 and in Figs. 5-5 to 5-8 (H_α, H_β, H_γ, and H_δ, respectively). As can be seen from the figures there is good agreement between the calculated and measured spectral profiles. In each case the calculated 'quality of fit' was nearly optimum, i.e., the value of X-square as defined for Table V-2 was nearly one. The experimental error used in calculating X-square (and also in performing the least-square optimization) mainly came from

counting error (square root of the number of counts) +

a 1% error due to line intensity fluctuation from the discharge +

an error in the profile intensity due to the error in the wavelength measurement.

The poorest fit occurs for the last case, H_δ, shown in Fig. 5-8 where the major discrepancy occurs at the center of the profile where the measured data lie below the calculated profile. In Chapter III.C we noted a similar effect in the calculation for H_β for a high-dc electric field ($E_{dc} \geq 2.5$ kV/cm), i.e., the calculated profile showed a strong dip at the center which was not present in the profile calculated using the simple Blochinzew theory. For the much weaker dc electric field in this experiment one does not see this effect for H_β, but for H_δ, where the effect of a dc electric field is greater (the dc Stark splitting is proportional to the principal quantum number), the effect might be

Table V-2. Electric field data derived from fits of hydrogen profiles calculated using Blochinzew theory to corresponding experimentally measured profiles.

Line	Fig.	Frequency (cm^{-1})	E_0(kV/cm)	Power[a]	A[b]	X-Square[c]
H_α	5-5	1.156±.002	5.96±.03	1.0.±.01	1.03±.00	1.41
H_β	5-6	1.164±.004	5.76±.04	0.95±.01	1.04±.01	0.85
H_γ	5-7	1.161±.004	5.94±.03	1.01±.01	1.09±.01	0.73
H_δ	5-8	1.158±.008	5.95±.05	1.01±.01	1.24±.03	2.87

[a]Power in milliwatts measured at the Hewlett-Packard power meter. For conversion to power at the cavity see Table V-1.

[b]Narrowing parameter: Instrument width used by PISA for a best fit was 'measured width'/A, i.e., A = 1.03 means PISA used an instrument width 3% narrower than that measured with the microwave field off.

[c]X-square is defined by

$$\left[\sum_{i=1}^{N_p} (\Delta I)^2/(\delta I)^2\right]/N_p,$$

where the sum is over the N_p points at which the profile is measured, ΔI represents the deviation at the point 'i' of the calculated intensity from the measured intensity, and δI is the experimental error at the point i. An optimum fit corresponds to X-Square $\simeq$ 1.

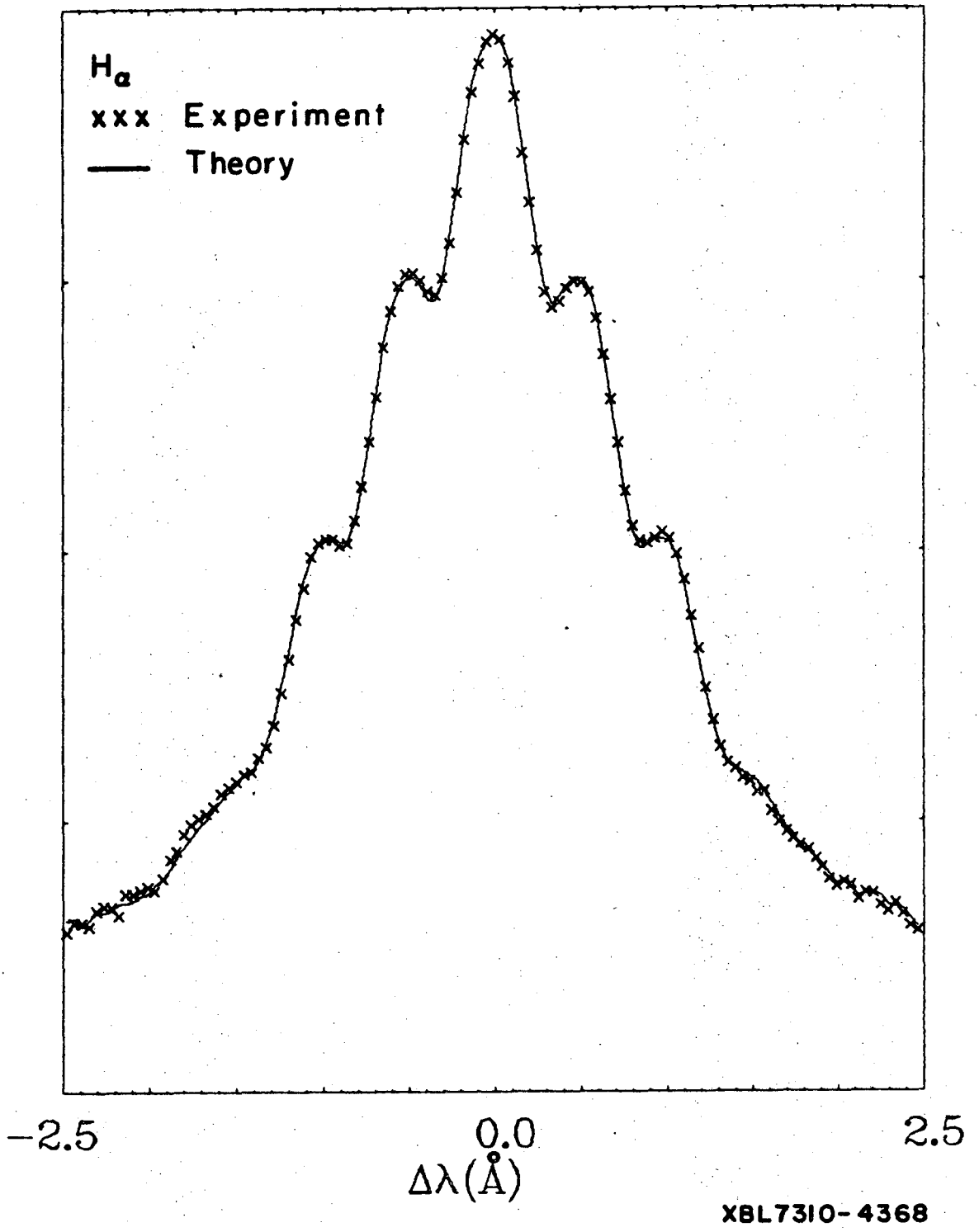

Fig. 5-5. For legend, see page 91a.

Fig. 5-5. Comparison of experiment and the Blochinzew theory for H_α for the case of no magnetic field, a linearly polarized high-frequency electric field, and direction of observation perpendicular to the electric field. The parameters determining the theoretical profile have been varied for a best least-square fit to the experimental data (see Table V-2).

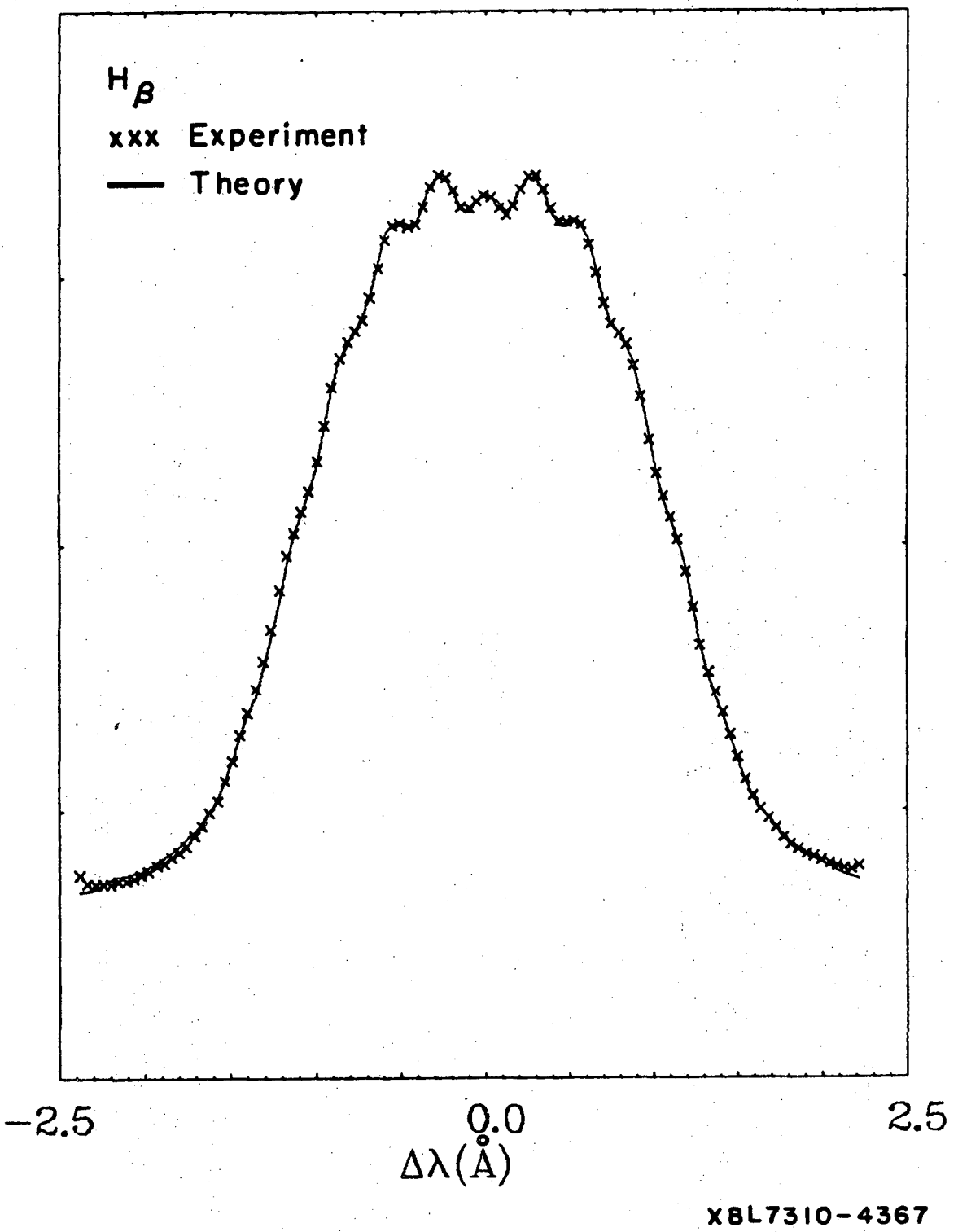

Fig. 5-6. For legend, see page 92a.

Fig. 5-6. Comparison of experiment and the Blochinzew theory for H_β for the case of no magnetic field, a linearly polarized high-frequency electric field, and direction of observation perpendicular to the electric field. The parameters determining the theoretical profile have been varied for a best least-square fit to the experimental data (see Table V-2).

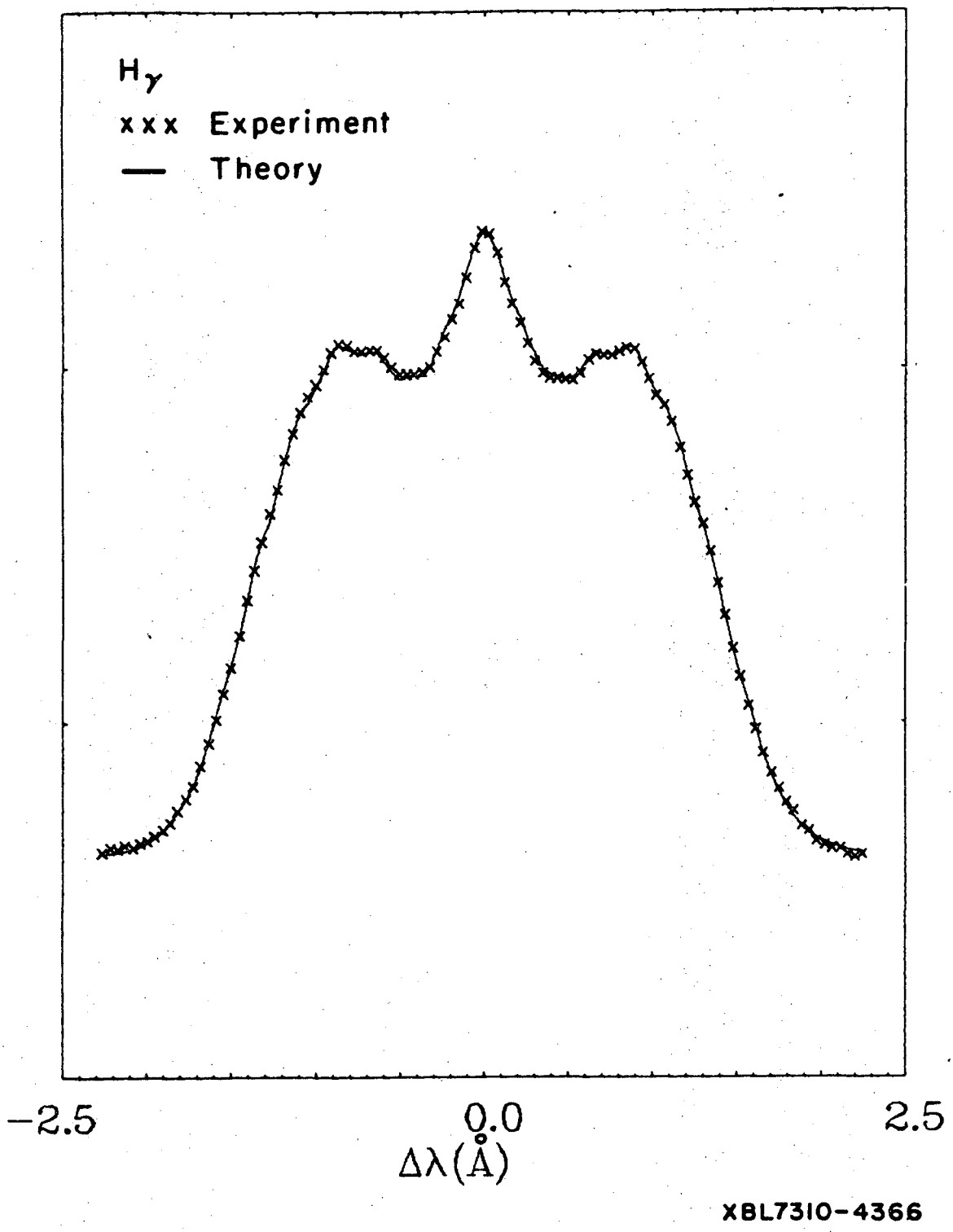

Fig. 5-7. For legend, see page 93a.

Fig. 5-7. Comparison of experiment and the Blochinzew theory for H_γ for the case of no magnetic field, a linearly polarized high-frequency electric field, and direction of observation perpendicular to the electric field. The parameters determining the theoretical profile have been varied for a best least-square fit to the experimental data (see Table V-2).

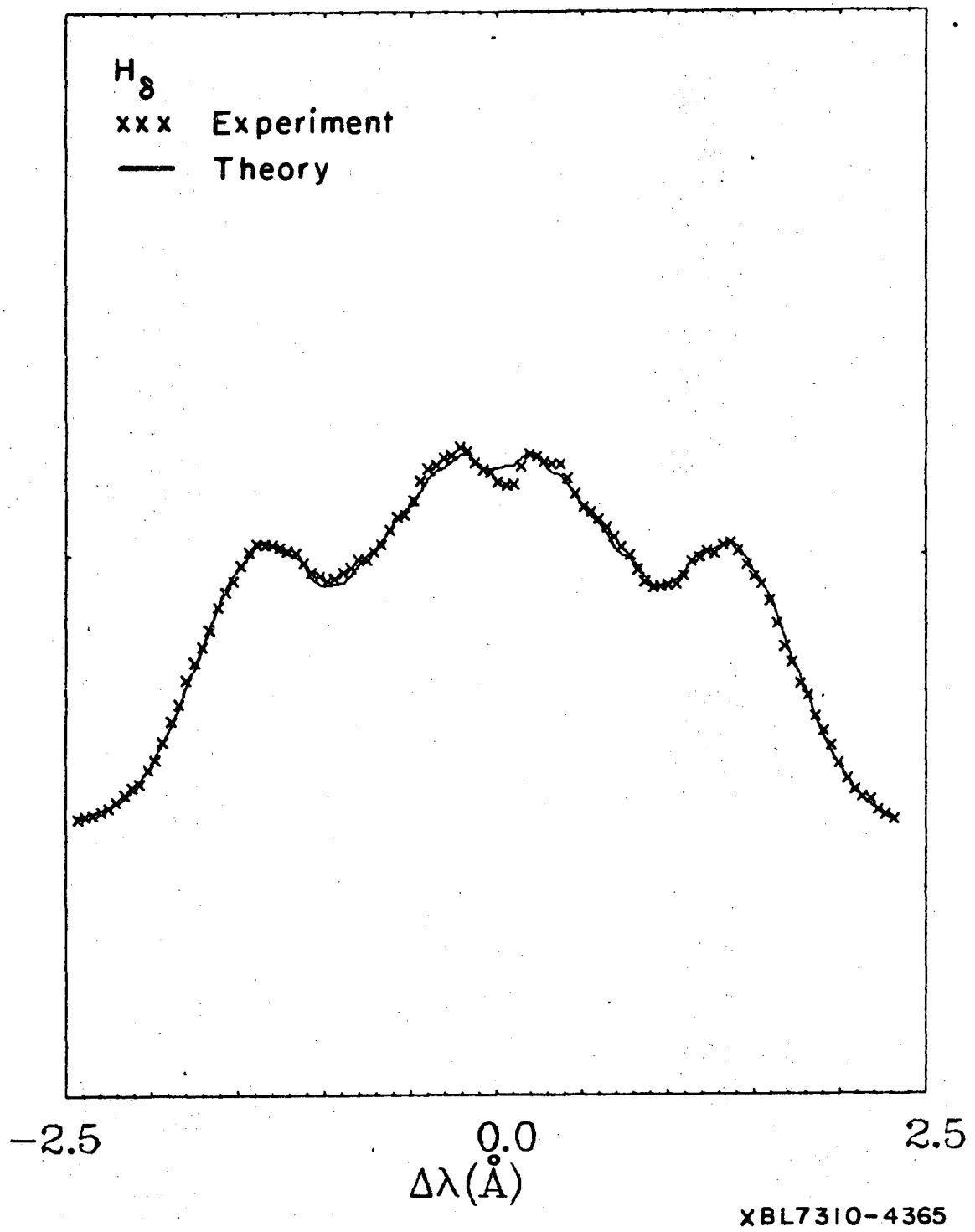

Fig. 5-8. For legend, see page 94a.

Fig. 5-8. Comparison of experiment and the Blochinzew theory for H_δ for the case of no magnetic field, a linearly polarized high-frequency electric field, and direction of observation perpendicular to the electric field. The parameters determining the theoretical profile have been varied for a best least-square fit to the experimental data (see Table V-2).

visible. Unfortunately, calculating H_δ correctly, using the more complete theory of Chapter III.C, was prohibitively expensive and could not be done to check this assertion.

Table V-2 reviews the best-fit parameters as found by PISA for the four Balmer lines considered in this section. As can be determined from the table, the best-fit values for the frequency agree very well with each other (except for H_α to within the calculated experimental error) and with the value of the electric-field frequency measured using a cavity wavemeter, 1.162 cm^{-1}. The values of the electric-field strength all lie within experimental error (note that one must correct for the different microwave power used for H_β) and agree very well with the values of the electric field at the corresponding power as determined from the helium data in the previous section (Fig. 5-4). An interesting aspect of the best fit solution is the 'narrowing' of each line required in each case for a best fit. The pattern of the systematic change in the instrument width with principal quantum number seems to indicate that the presence of the microwave electric field reduces the mean ambipolar electric field and hence the dc Stark broadening.

VI. CONCLUSION AND FINAL REMARKS

In the body of this paper we have investigated the effect of a monochromatic high-frequency electric field on the spectral profiles of hydrogen and helium. We have shown that using a numerical solution of a very general theory we could get very good agreement between calculated and measured profiles for both hydrogen and helium spectral lines. However, the general problem of the application of the high-frequency Stark effect to plasma diagnostics involves many further considerations. In this final section we will discuss some of them.

1. Finite Frequency Spread

In general, the electric fields in a plasma will not be monochromatic, they will have some characteristic frequency spread $\Delta\omega$, and some characteristic central frequency ω_0. For this case, the methods used to solve Schrödinger's equation must be considerably different. Instead of expanding the time dependence of the wave function, $T_j(t)$, in terms of a Fourier series as we have done, it must be expressed in terms of a Fourier transform $T_j(\omega')$, which will be a continuous function of frequency. The fundamental equation (2.12) will then take on the form of an integral equation: relating $T_j(\omega')$ to the folding integral of $T_j(\omega - \omega')$ and the Fourier transform of the electric field $E(\omega')$. Such an equation cannot be solved in the manner described in Chapter II, although it should be noted that in the limit that the frequency spread becomes very small relative to the central frequency, i.e., when $E(\omega) \to \delta(\omega - \omega_0)$, the integral equation reduces to Eq. (2.12) if

we define $C_{js} = T_j(s\omega_0)$. Hence we expect for $\Delta\omega \ll \omega_0$ that the solutions of Eq. (2.12) will give good approximations to the actual solutions. We can consider some aspects of the more complex case of a finite frequency spread which is comparable to the central frequency by referring to the model developed in Chapter II.E, which described the high-frequency Stark effect in terms of multi-quantum transitions. The presence of a spectrum with a finite frequency spread leads to two new effects not seen in the monochromatic electric field case: a broadening of the individual satellites due to the finite spread, and a modification in the satellite pattern due to coupling of the electric field at different frequencies. The first case involves transitions in which the quantum which is emitted or absorbed is always of the same frequency. For this case there is no coupling between the electric field at different frequencies and we may treat each frequency component of the spectrum independently: solving Eq. (2.12) for each frequency, and then performing a superposition of the different solutions to get the complete solution. The resultant satellite spectrum will then consist of satellites which lie at different positions and a consequent broadening of the individual satellites will result. For a very broad frequency spectrum ($\Delta\omega \simeq \omega_0$), the satellites will overlap and the satellite pattern will be smeared out and not useful for plasma diagnostics. It should be noted that for the particular cases of helium considered in Chapter V.A, the profiles of the far and near satellites of the forbidden line in the perturbation limit directly reflect the electric energy

spectrum since the intensity of each of these satellites is proportional to E^2_{rms}.

In the above, we considered the case in which the same frequency quantum is emitted or absorbed at each (virtual) exchange of a quantum between the electric field and the atom. One can also consider the case that the quantum emitted or absorbed at each step is of a different frequency than at a previous step. Since, in our model, the energy of the optical photon, which results when the atom undergoes an eventual real decay to a lower state, is the unperturbed energy difference of the two states plus the net energy retained from the electric field, we see that this type of transition produces new satellites in the high-frequency spectrum at the beat frequencies of the various frequency components of the electric field spectrum, and hence also leads to a new source of broadening as well as a change in the calculated intensities of the normal satellites. The actual calculation of such effects must await a more general theory than that presented above. However, from this model one conclusion can be drawn: Since the second type of effect is of higher-order in the electric field strength, i.e., it involves at least two different quanta from the electric field, one can ignore its effect for weak electric fields. Considering as a special case the helium profiles examined in Chapter V.A, this means that, as long as the satellite spectrum is composed only of the allowed line and the lowest order 'far' and 'near' satellites of the forbidden transition, one can ignore the complications introduced by coupling within the electric field

spectrum and can treat the satellite spectrum as though each frequency component was independent.

2. Effect of the Plasma

In order to make the best use of the high-frequency effect for plasma diagnostics, one must be able to identify the individual satellites. Unfortunately, spectral lines produced within a plasma tend to be broadened by the plasma. The various methods of broadening have been much discussed[33] and will not be described further. However, it should be noted that these broadening mechanisms produce limitations to the applicability of the high-frequency Stark effect to plasma diagnostics in plasmas with too great a density (due to pressure broadening) and with too great a temperature (due to Doppler broadening). The use of the method could also be limited by a strong gradient in the density of the plasma if it led to different regions of the plasma emitting at different frequencies (for instance, if the emission was at the respective plasma frequencies). An optical method useful for making local measurements within the plasma has been discussed in Ref. 34. As a final note to this section we will remark that the problem of plasma broadening of helium spectral lines will always be less critical than the corresponding problem for hydrogen, and hence the use of helium for plasma diagnostics is to be preferred. Furthermore, the wide variety of potential helium lines suitable for the application of the high-frequency Stark effect, makes the method suitable for a wide variety of electric field frequencies and electric field strengths.

3. Background

One of the problems of the use of the high-frequency Stark effect in helium for plasma diagnostics is the necessity of observing relatively weak satellites which are near to a strong allowed line. The satellites are often buried in the line wing and difficult to observe. This puts an effective lower limit which differs with particular spectral line and frequency of the electric field, but which generally is of the order of 1 kV/cm electric field strength. Use of phase-sensitive techniques, when applicable, can lower this minimum value to 200 V/cm (lowest value of electric field so far measured using the technique[3]). Two interesting methods which appear to increase sensitivity have been reported by Burrell and Kunze, both using a tunable dye laser to illuminate the plasma.[35,36]

ACKNOWLEDGMENTS

The author wishes to thank all the members of the Berkeley plasma physics group for their help throughout the course of this work. The author especially wishes to thank Prof. Wulf B. Kunkel and Dr. William S. Cooper for their guidance, E. B. Hewitt for his help on the experiment, and Margaret R. Thomas for her help in typing this manuscript.

APPENDICES

A. Evaluation of Transition Rate Integral for an Atom in an Oscillating Electric Field

We wish to evaluate

$$I_k^{iu} \equiv \int_{\omega_-}^{\omega_+} d\omega_\gamma |\Gamma_k^{(1)}|^2 \rho(\omega_\gamma) d\Omega \tag{A1}$$

where $\omega_\pm = \lambda_{ik} + u\omega \pm \Delta$ and where $1/(t - \tau)$, Δ, ω satisfy $1/(t - \tau) \ll \Delta \ll \omega, \lambda_{ik}$. The integrand of expression (A1) is a product of rapidly varying terms [$|\Gamma_k^{(1)}|^2$ varies on the $1/(t - \tau)$ frequency scale] and a slowly varying term [$\rho(\omega_\gamma)$ varies on the λ_{ik} frequency scale]. Over the range of integration

$$\rho(\omega_\gamma) = \rho(\lambda_{ik} + u\omega) + \mathcal{O}\left(\frac{\Delta}{\lambda_{ik} + u}\right) \simeq \rho(\lambda_{ik} + u\omega).$$

Hence in evaluating the integral we set $\rho(\omega_\gamma) = \rho(\lambda_{ik} + u\omega)$ and take it outside the integral. The resulting expression for I_k^{iu} is a sum of terms with resonant type denominators:

$$I_k^{iu} = 2\rho(\lambda_{ik} + u\omega)d\Omega(t - \tau)\left[K_{uu}^{ik}A_0 + \sum_{\substack{s=-\infty \\ s\neq u}}^{\infty} (K_{us}^{ik} + K_{su}^{ik})A_1 + \sum_{\substack{s,s'=-\infty \\ s,s'\neq u}}^{\infty} K_{ss'}^{ik}A_2\right], \tag{A2}$$

where A_0, A_1, and A_2 are given by [$\xi \equiv \frac{1}{2} u\omega(t - \tau)$]

$$A_0 = \int_{-\Delta(t-\tau)}^{\Delta(t-\tau)} d\xi \, \frac{\sin^2\xi}{\xi^2} ,$$

$$A_1 = \int_{-\Delta(t-\tau)}^{\Delta(t-\tau)} d\xi \, \frac{\sin\xi}{\xi} \, \frac{\sin\left[\frac{1}{2}(s-u)\omega(t-\tau)+\xi\right]}{\left[\frac{1}{2}(s-u)\omega(t-\tau)+\xi\right]}$$

$$A_2 = \int_{-\Delta(t-\tau)}^{\Delta(t-\tau)} d\xi \, \frac{\sin\left[\frac{1}{2}(s-u)\omega(t-\tau)+\xi\right]}{\left[\frac{1}{2}(s-u)\omega(t-\tau)+\xi\right]}$$

$$\times \, \frac{\sin\left[\frac{1}{2}(s'-u)\omega(t-\tau)+\xi\right]}{\left[\frac{1}{2}(s'-u)\omega(t-\tau)+\xi\right]} .$$

We now consider the evaluation of A_0, A_1, A_2. The integrand of A_0 is a sharply peaked function of ξ; since $\omega(t-\tau) \gg 1$, the integrand is already small at the integral limits and hence only a small error $\left[\sim 1/\Delta(t-\tau)\right]$ is made in letting the limits of integration go to $\pm\infty$. A_0 is then a standard integral,

$$A_0 = \pi. \tag{A3}$$

In evaluating A_1 we first note that ξ is at most $\Delta(t-\tau)$. Hence over the entire interval of integration we may make the expansion

$$\frac{1}{\frac{1}{2}(s-u)\omega(t-\tau)+\xi} = \frac{1}{\frac{1}{2}(s-u)\omega(t-\tau)} \times \left(1 - \frac{\xi}{\frac{1}{2}(s-u)\omega(t-\tau)} + \cdots\right)$$

Next, expanding $\sin\left[\frac{1}{2}(s-u)\omega(t-\tau)\right] + \xi$ and eliminating terms from the resulting expression which are odd in ξ (and hence integrate to 0) yields: $A_1 = A_1^0 + A_1^1$.

$$A_1^0 = \frac{\sin\left[\frac{1}{2}(s-u)\omega(t-\tau)\right]}{\left[\frac{1}{2}(s-u)\omega(t-\tau)\right]} \int_{-\Delta(t-\tau)}^{\Delta(t-\tau)} d\xi \, \frac{\sin\xi \cdot \cos\xi}{\xi}$$

$$A_1^1 = \frac{\cos\left[\frac{1}{2}(s-u)\omega(t-\tau)\right]}{\left[\frac{1}{2}(s-u)\omega(t-\tau)\right]^2} \int_{-\Delta(t-\tau)}^{\Delta(t-\tau)} d\xi \, \sin^2\xi .$$

Now A_1^1 can be directly integrated and is of order Δ/ω relative to A_1^0 and hence can be ignored. As in the evaluation of A_0 above, the sharply-peaked nature of the integrand of A_1^0 allows the limits of integration to be extended to $\pm\infty$ [the error so incurred is $\sim 1/\Delta(t-\tau)$ times A_1^0 and hence is ignorable]. Then A_1^0 is a standard integral

$$A_1 = \frac{\pi}{2} \frac{\sin\left[\frac{1}{2}(s-u)\omega(t-\tau)\right]}{\left[\frac{1}{2}(s-u)\omega(t-\tau)\right]} . \qquad (A4)$$

An evaluation of A_2 similar to that of A_1 shows that $A_2 = \mathcal{O}\left[1/\omega^2(t-\tau)^2\right]$ and hence can be ignored relative to A_0 and A_1 which are of order 1 and $1/\omega(t-\tau)$, respectively. Thus to the order retained in the calculation

$$A_2 = 0. \qquad (A5)$$

Substituting Eqs. (A3)-(A5) into Eq. (A2) yields for I_k^{iu}

$$I_k^{iu} = 2\pi\rho(\lambda_{ik} + u\omega)d\Omega(t - \tau)\left[K_{uu}^{ik} + \frac{1}{2}\sum_{\substack{s=-\infty \\ s\neq u}}^{\infty}(K_{us}^{ik} + K_{su}^{ik}) \times \frac{\sin\left[\frac{1}{2}(s - u)\omega(t - \tau)\right]}{\left[\frac{1}{2}(s - u)\omega(t - \tau)\right]}\right]$$

$$= \pi\rho(\lambda_{ik} + u\omega)d\Omega(t - \tau)\sum_{s=-\infty}^{\infty}(K_{us}^{ik} + K_{su}^{ik}) \frac{\sin\left[\frac{1}{2}(s - u)\omega(t - \tau)\right]}{\left[\frac{1}{2}(s - u)\omega(t - \tau)\right]}.$$

Since $(K_{us}^{ik} + K_{su}^{ik}) = 2\,\mathrm{Re}(K_{us}^{ik})$, I_k^{iu} is a real quantity.

B. Perturbation Solution of Equation (2.12)

We consider the case:

(1) $\alpha_{jj'} \equiv \alpha_j \delta_{jj'}$, then $\omega_j' = \omega_j + \alpha_j$ [see Eq. (2.3)],

(2) β small, then following the discussion of Chapter III.A. we can ignore all coefficients except those with $s = 0, \pm 1$, i.e., $S = 1$. With these assumptions Eq. (2.12) can be represented by the eigenvalue matrix equation (shown explicitly for the special case $N = 3$ in Fig. B-1):

$$(M - \lambda)C = 0. \tag{B1}$$

By expanding in the usual way about column and row elements we can get an analytic expression for the determinant of $M - \lambda$ ($\equiv D$) accurate to order β^2. If we define

$$\Upsilon(\lambda) = \prod_{k=1}^{N} (\omega_k' + \omega - \lambda)(\omega_k' - \lambda)(\omega_k' - \omega - \lambda),$$

then

$$D(\lambda) = \Upsilon(\lambda)\left\{ 1 - \sum_{j=1}^{N} \sum_{j'=1}^{N} \left[\frac{\beta_{jj'}^{+}\beta_{jj'}^{-}}{(\omega_{j'}' - \lambda)(\omega_j' + \omega - \lambda)} + \frac{\beta_{jj'}^{+}\beta_{jj'}^{-}}{(\omega_{j'}' - \lambda)(\omega_j' - \omega - \lambda)} \right] \right\} \tag{B2}$$

(a) Solution of Eq. (B1) to zero-order in the parameter β.

In zero-order the eigenvalue condition, $D = 0$, reduces to

$$\Upsilon(\lambda^{[0]}) = 0.$$

Thus the zero-order eigenvalues are given by

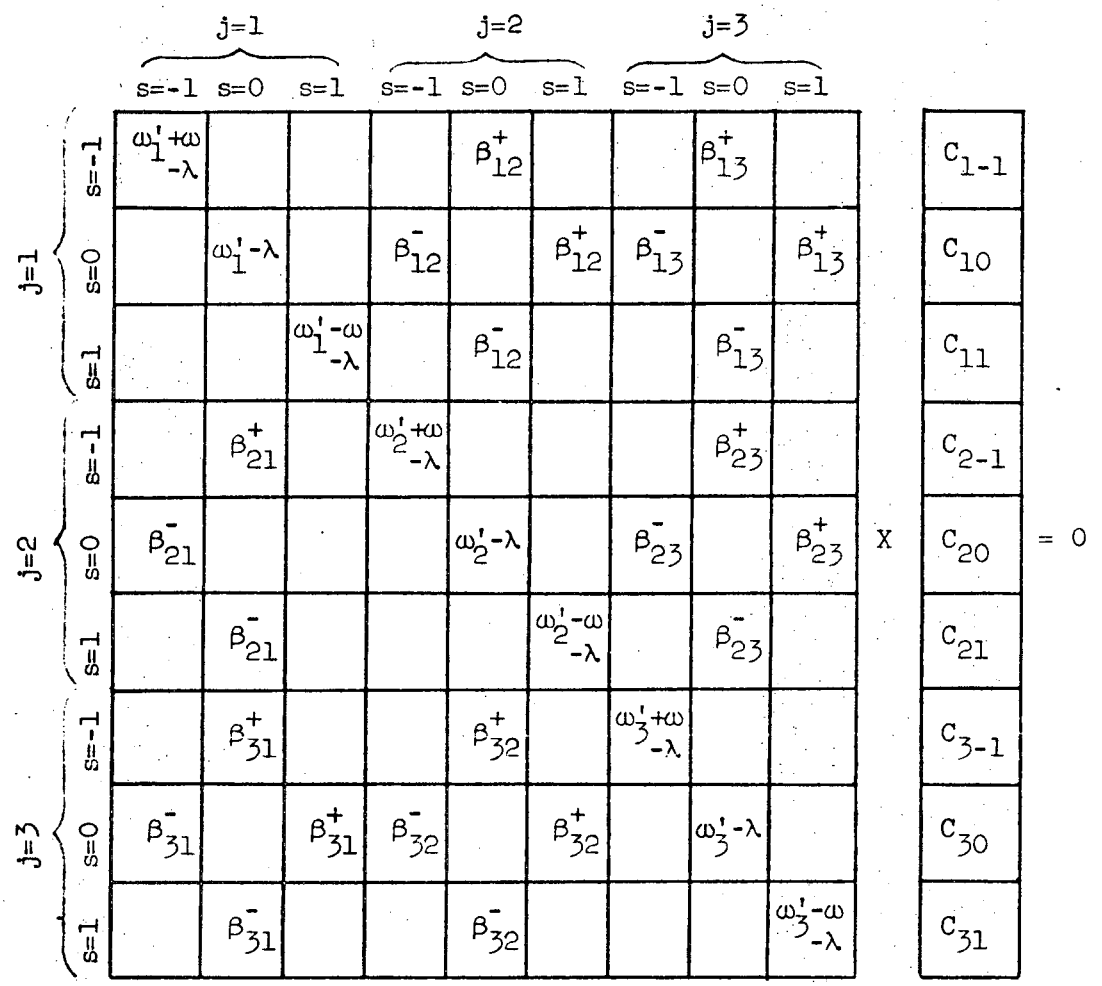

Fig. B-1. An explicit example of Eq. (B1) for the special case N = 3.

$$\lambda^{[0]} = \begin{cases} \omega_i' + \omega \\ \omega_i' \qquad , \; i = 1, \cdots, N. \\ \omega_i' - \omega \end{cases} \tag{B3}$$

Following the discussion of Chapter II.E we choose as our solution the case

$$\lambda_i^{[0]} = \omega_i'.$$

The components of the zero-order eigenvector can then be found from Eq. (B1) (with $\beta^{\pm} = 0$) and are given by

$$C_{js}^{i[0]} = \delta_{ij}\delta_{s0}.$$

(b) Solution of Eq. (B1) to first order

Setting $\lambda = \omega_i' + \lambda_i^{[1]}$ $\left[\lambda_i^{[1]} = \mathcal{O}(\beta)\right]$, the eigenvalue condition $D = 0$ becomes

$$\lambda_i^{[1]}(-\omega^2) \prod_{\substack{k=1 \\ k\neq i}}^{N} (\omega_{ki}'^2 - \omega^2)\omega_{ki}' + \mathcal{O}(\beta^2) = 0. \tag{B4}$$

If the energy levels are nondegenerate, i.e., if $\omega_{ki}' \neq 0$ and if $|\omega_{ki}' \pm \omega| \gg \mathcal{O}(\beta)$ for all $k \neq i$, then

$$\lambda_i^{[1]} = 0 \tag{B5}$$

and λ_i differs from $\lambda_i^{[0]}$ by at most terms quadratic in $\beta^{\pm}$. On the other hand, if $\omega_{ik}' = 0$ for some value of k, then $\lambda_i^{[1]}$ can be finite and the two levels i and k will exhibit a linear Stark shift. If $|\omega_{ki}' \pm \omega| \lesssim \mathcal{O}(\beta)$, perturbation theory does not hold (see discussion at end of Chapter II.F). Continuing with the

nondegenerate case, we calculate the first-order correction to the eigenfunctions. Substituting $\lambda = \omega'_i$ into Eq. (B1) yields

$$\left.\begin{aligned} &\pm C^{i\,[1]}_{i,\mp 1} = \mathcal{O}(\beta^2) \\ &\beta^{\pm}_{ji} + (\omega'_{ji} \pm \omega) C^{i\,[1]}_{j,\mp 1} = \mathcal{O}(\beta^2) \qquad j \neq i \\ &\omega'_{ji} C^{i\,[1]}_{j0} = \mathcal{O}(\beta^2) \end{aligned}\right\} \tag{B6}$$

Equations (B6) plus the normalization condition

$$\sum_{j=1}^{N} \sum_{s=-\infty}^{\infty} |C^i_{js}|^2 = 1$$

yield to order β:

$$\lambda_i = \omega'_i$$

$$C^i_{js} = \delta_{s0}\delta_{ij} + \frac{\delta_{s1}\beta^-_{ji}}{\omega'_{ij} + \omega} + \frac{\delta_{s,-1}\beta^+_{ij}}{\omega'_{ij} - \omega} \tag{B7}$$

(c) Solution of Eq. (B1) to second-order

Setting $\lambda = \omega'_i + \lambda^{[2]}_i \left[\lambda^{[2]}_i = \mathcal{O}(\beta^2)\right]$, the eigenvalue condition $D = 0$ becomes to second order in β:

$$0 = -\omega^2 \lambda^{[2]}_i \prod_{\substack{k=1 \\ k\neq 1}}^{N} (\omega'^2_{ki} - \omega^2)\omega'_{ki} - \sum_{\substack{j=1 \\ j\neq 1}}^{N} \omega^2 \sum_{\substack{k=1 \\ k\neq 1,j}}^{N} (\omega'^2_{ki} - \omega^2)\omega'_{ki}$$

$$\times \left[\omega'_{ji}(\omega'_{ji} - \omega)\beta^-_{ij}\beta^+_{ji} + \omega'_{ji}(\omega'_{ji} + \omega)\beta^+_{ij}\beta^-_{ji}\right]. \tag{B8}$$

Finally, noting that $(\beta^+_{ij})^* = \beta^-_{ij}$, we get for the second-order

correction to the eigenvalue

$$\lambda_i^{[2]} = \sum_{j=1}^{N} \frac{|\beta_{ji}^{+}|^2}{\omega_{ij}' - \omega} + \frac{|\beta_{ji}^{-}|^2}{\omega_{ij}' + \omega} . \qquad \text{(B9)}$$

C. The Microwave System--Calculations and Measurements

Figure C-1 shows a cutaway view of the microwave cavity and the quartz Geissler tube. The cavity is machined in a split block of brass and is gold-plated on the inside to enhance conductivity and to retard oxidation. The viewing slit has been constructed parallel to the direction of current flow so as to least disturb the operation of the cavity. The round holes through which the Geissler tube enters and leaves the cavity are below cutoff so as to be nonradiating. The various field and current directions for the TM_{010} cavity mode are noted on the figure. During operation dry nitrogen flows through the cavity and serves to cool the Geissler tube and cavity as well as further diminish any oxidation which might otherwise occur.

The presence of the quartz tube and its contained plasma will change the normal modes of the cavity. In general, for a cylindrical system with interfaces between two dielectrics, the boundary conditions

$$\epsilon E_n \text{ continuous, } E_t \text{ continuous}$$
$$B_t/\mu \text{ continuous, } B_n \text{ continuous} \qquad \text{(C1)}$$

across the interface do not allow the usual transverse magnetic and electric type modes; i.e., in general, the normal modes of a compound system of several dielectrics, even if it is a cylindrically symmetric system, will have both a component of E_z and B_z. However, for those modes which in the simple cavity case have azimuthal symmetry, i.e., m = 0 in the usual notation TM_{mnp} or TE_{mnp}, there are corresponding TE and TM modes which simultane-

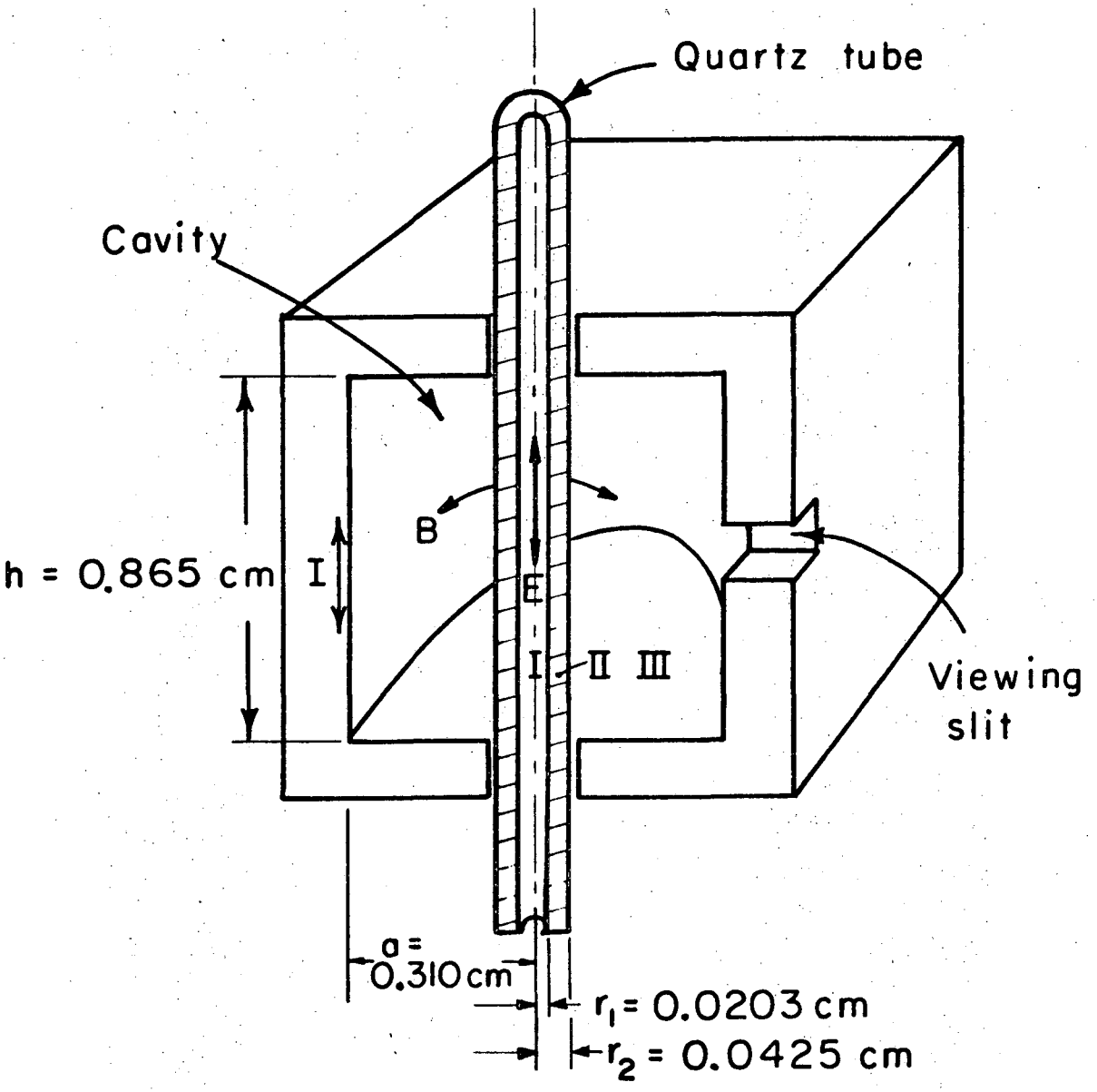

Fig. C-1. Schematic view of the microwave cavity and the quartz Geissler tube.

ously satisfy all the boundary conditions.[34]

These modes can be calculated by arguments similar to those used for the simple cavity (the notation used in the following is the same as Jackson, chapter 8). Consider modes of type TM_{0np} (azimuthally symmetric) for a compound system of nonpermeable dielectrics ($\mu = 0$). Within each dielectric region characterized by a permittivity ϵ_i the fields can be derived from the longitudinal electric field E_z, where E_z is given by

$$E_z = E_0(\rho) \cos(p\pi z/h) e^{-i\omega t}, \qquad (C2)$$

where $E_0(\rho)$ satisfies the Bessel equation

$$\frac{d^2E_0}{d\rho^2} + \frac{1}{\rho}\frac{dE_0}{d\rho} + \left(\gamma_i^2 - \frac{m^2}{\rho^2}\right) E_0 = 0, \qquad (C3)$$

with $m = 0$, and where γ_i^2 is given by

$$\gamma_i^2 = \epsilon_i \frac{\omega^2}{c^2} - \left(\frac{p\pi}{h}\right)^2 \equiv n_i^2 k^2 - \left(\frac{p\pi}{h}\right)^2, \qquad k \equiv \frac{\omega}{c} \qquad (C4)$$

and $n_i \equiv \sqrt{\epsilon_i}$ is the index of refraction of region 'i'. The z dependence has been chosen to explicitly satisfy the boundary conditions at the ends of the cavity and must be the same in each dielectric region to satisfy the boundary conditions at all points along the interfaces. Similarly the frequency ω (or the wavenumber k) must be the same in each dielectric region to satisfy the boundary conditions at all times. It is easy to show that with the above expression for E_z the boundary conditions

given in Eq. (C1) are equivalent to the two conditions:

$E_0(\rho)$ continuous across a boundary, and

$$\frac{dE_0}{d\rho}\frac{\epsilon_i}{\gamma_i^2} \text{ continuous across a boundary.} \qquad (C5)$$

Note that for the case, p = 0 (no variation of the fields in the z direction), the second boundary condition becomes simply $dE_0/d\rho$ continuous.

The solutions of Eq.(C3) are Bessel functions of order m = 0. Specializing to the specific case shown in Fig. C-1, the solution for $E_0(\rho)$ in each of the three regions will be given by:

$$\begin{aligned}
&\text{Region I:} && E_0(\rho) = \bar{E}_0 J_0(n_1 k\rho) && 0 \le \rho \le \rho_1 \\
&\text{Region II:} && E_0(\rho) = \bar{E}_0\left[A_1 J_0(n_2 k\rho) + B_1 N_0(n_2 k\rho)\right] && \rho_1 \le \rho \le \rho_2 \\
&\text{Region III:} && E_0(\rho) = \bar{E}_0\left[A_2 J_0(n_3 k\rho) + B_2 N_0(n_3 k\rho)\right] && \rho_2 \le \rho \le a, \qquad (C6)
\end{aligned}$$

where J_m and N_m are, respectively, Bessel functions of order m of the first and second kind. Use of the requirement of a finite valued solution at the origin has eliminated a term proportional to N_0 in region I. $\bar{E}_0$ represents the value of the electric field on the axis, i.e., for $\rho = 0$. There are five unknowns in Eqs. (C6), A_1, B_1, A_2, B_2, and k, whose values are to be determined by the five boundary conditions:

$$J_0(n_1 k\rho_1) = A_1 J_0(n_2 k\rho_1) + B_1 N_0(n_2 k\rho_1)$$

$$-n_1 k J_1(n_1 k\rho_1) = -n_2 k\left[A_1 J_1(n_2 k\rho_1) + B_1 N_1(n_2 k\rho_1)\right]$$

$$A_1 J_0(n_2 k\rho_2) + B_1 N_0(n_2 k\rho_2) = A_2 J_0(n_3 k\rho_2) + B_2 N_0(n_3 k\rho_2)$$

$$-n_2 k\left[A_1 J_1(n_2 k\rho_2) + B_1 N_1(n_2 k\rho_2)\right] = -n_3 k\left[A_2 J_1(n_3 k\rho_2) + B_2 N_1(n_3 k\rho_2)\right]$$

$$A_2 J_0(n_3 ka) + B_2 N_0(n_3 ka) = 0. \qquad (C7)$$

We have numerically solved Eqs. (C7) for the case: $n_1 = 1.0$, $n_2 = 1.94$ (index of refraction of fused quartz[35]), $n_3 = 1.0$, $\rho_1 = 0.0203$ cm, $\rho_2 = 0.0425$ cm, and $\rho_3 = 0.305$ cm, and for the TM_{010} mode. The resulting calculated mode frequency is 34.81 GHz; this is less than the resonant frequency of a simple cavity with the same outer dimensions, 37.62 GHz, and within 1% of the measured frequency 35.17 GHz. Figure C-2 shows the axial electric field dependence with radius and compares it to the case of a simple cavity. Both curves are normalized to the same stored energy U_0:

$$U_0 \equiv \frac{1}{8\pi}\int_V \epsilon E_0^2\, dv = \frac{1}{8\pi} V\bar{E}_0^2\eta, \qquad (C8)$$

where V is the cavity volume and η is a factor of order 1 [for the simple TM_{010} mode $\eta = J_1^2(2.405) = 0.2695$]. As can be seen from the figure the effect of the quartz is to flatten the profile near the axis of the cavity, to steepen the profile near the edge, and to increase the peak electric field on the axis by 3.4%. The calculated electric field variation over the inside of the Geissler tube is 0.5%. Similar calculations for the case of a plasma in the Geissler tube for which $\epsilon_1 = 1 - \omega_p^2/\omega^2$ have been carried out, but for densities of interest for this experiment the solution is essentially that given in Fig. 3-2 and the fre-

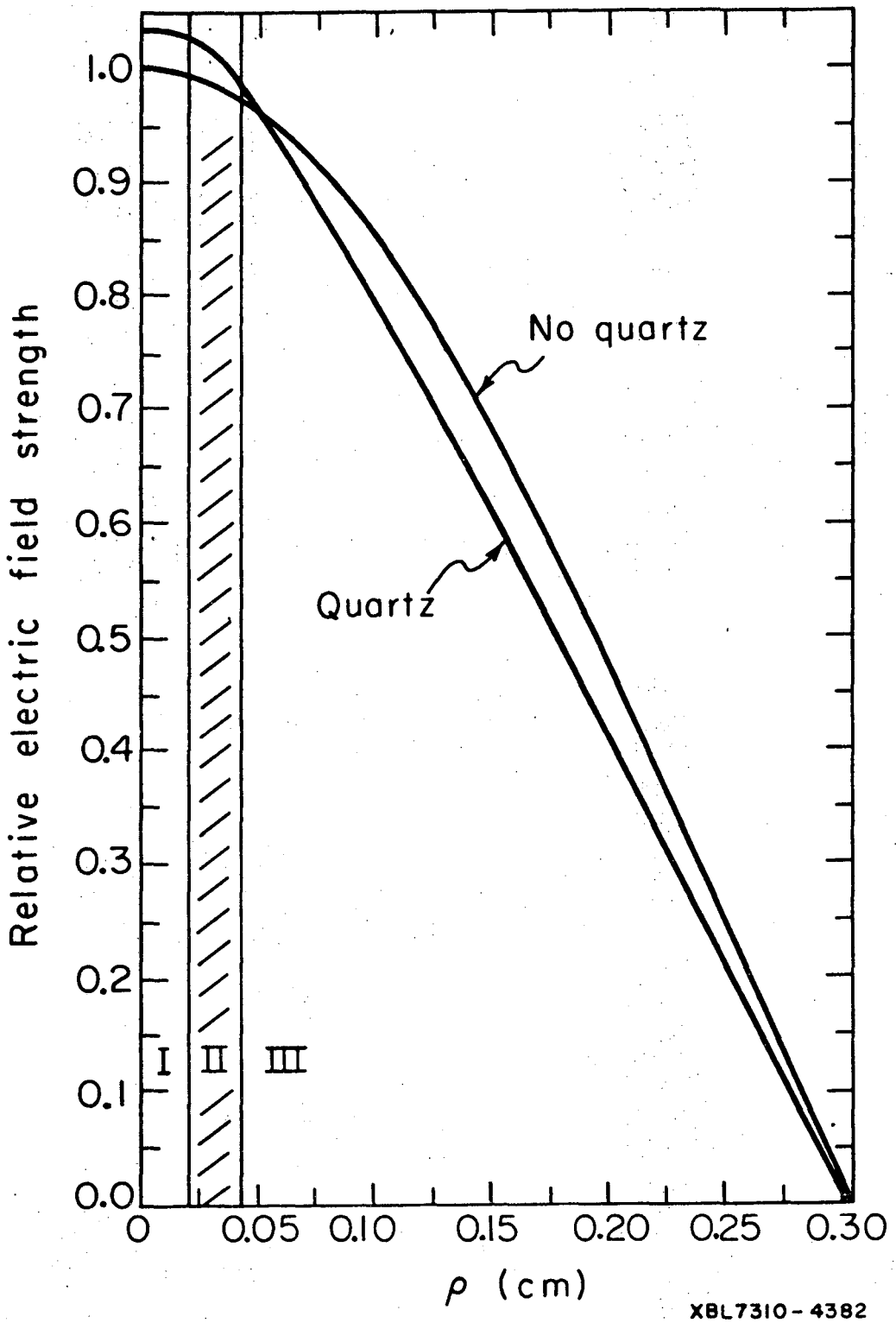

Fig. C-2. Axial electric field dependence on radius for the microwave cavity shown in Fig. C-1 in the TM_{010} mode.

quency is essentially unchanged from the no-plasma case (although the frequency difference can be used to measure the electron density of the plasma discharge; see below).

We have verified the z dependence of the axial electric field expected of the TM_{010} mode by passing a small quartz plug down the inside of the Geissler tube and measuring the frequency shift with position of the quartz plug. The results are shown in Fig. C-3. The theoretical profile expected for a z-independent electric field can be calculated from the perturbation expression for the frequency shift:[36]

$$\frac{\Delta f}{f} = \frac{\int_V \epsilon_0 E_0^2 (1 - n^2) dv}{16\, U_0} = \frac{(1 - n^2) V_{obj}}{2V\eta} , \qquad (C9)$$

where n is the index of refraction of the plug and V_{obj} its volume. This expression predicts that the frequency shift will be proportional to the length of the plug if the area is held constant. This dependence was checked by using plugs of different lengths and the expected result was seen. If the field was truly independent of z, then the expected frequency shift would be zero for the plug located outside the cavity, would decrease linearly with position to the value given by Eq. (C9) as the plug entered the cavity, and remain constant thereafter. Figure C-3 shows small deviations from this ideal picture. The finite Δf, even when the plug is outside the geometric boundary of the cavity, indicates that some microwave field escapes out of

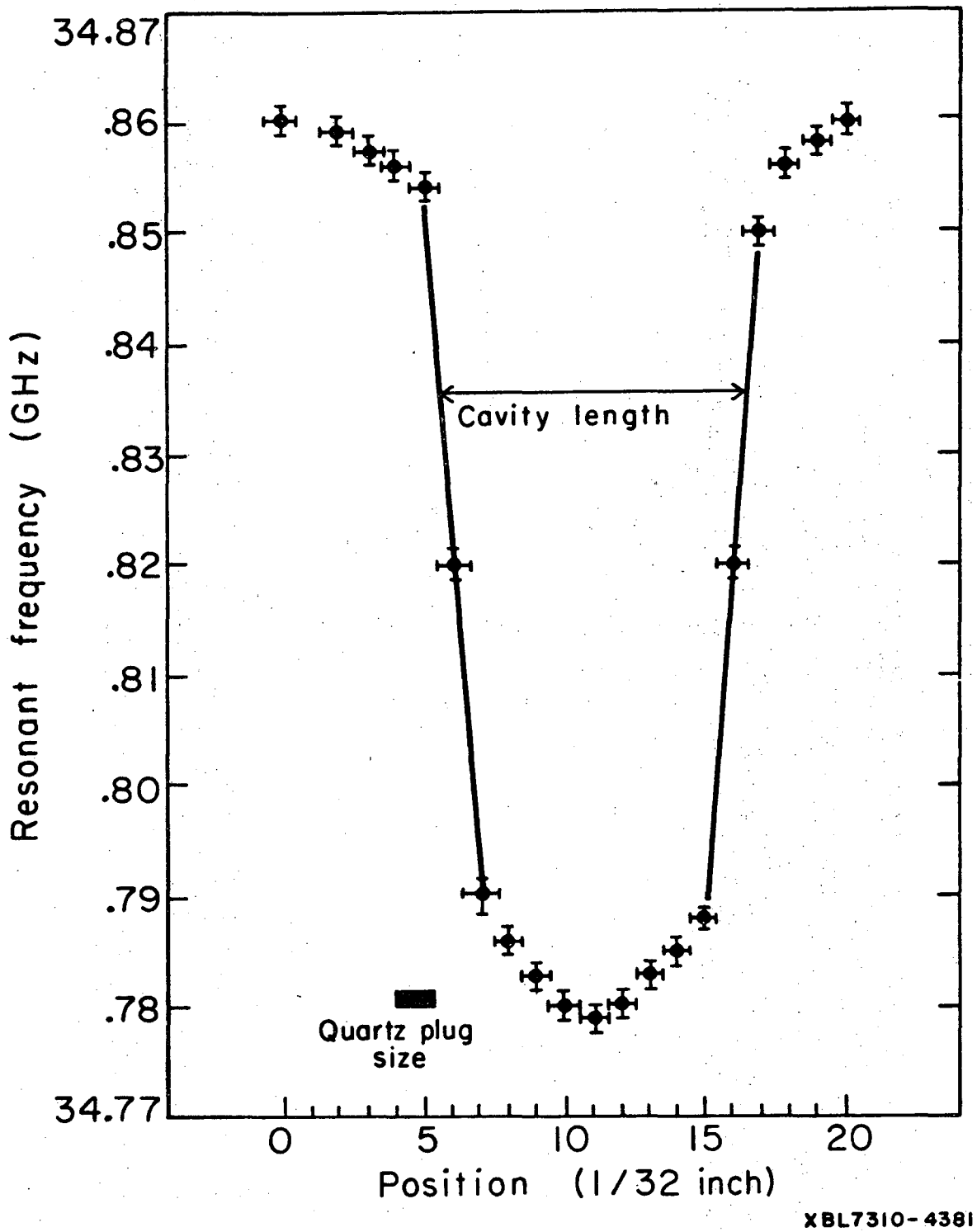

Fig. C-3. Measured resonant frequency of the microwave cavity as a function of the position of a perturbing quartz plug inserted into the cavity.

the cavity through the end holes. The unexpected behavior inside the cavity could have several causes: perturbations of the field distribution caused by the presence of the plug, a non-uniform cross section of the Geissler tube, or the specific way the cavity is excited; the coupling iris is on the midplane of the cavity (see Fig. C-1). The predicted maximum frequency shift can be calculated from Eq. (C9) and is 9.8×10^7 Hz for the plug used in the experiment. This compares to the measured value of 8.1×10^7 Hz in Fig. C-3.

To conclude this section on the microwave system we will calculate the electric field which exists in the discharge region inside the Geissler tube (region I in Fig. C-1) during steady state operation of the cavity with an input power P_0. As discussed above, this electric field is essentially $\bar{E}_0$, which is related to the stored energy in the cavity by Eq. (C8). In steady-state operation the stored energy is related to the input power by the unloaded 'Q', Q_0, of the cavity:[37]

$$Q_0 = \frac{\omega U_0}{P_0} . \tag{C10}$$

Using standard microwave techniques, Q_0 can be determined by measuring, near resonance, the VSWR (voltage standing-wave ratio) of the cavity as a function of frequency.[38] Equivalently, since

$$\text{VSWR} = \frac{1 + \sqrt{P_r/P_i}}{1 - \sqrt{P_r/P_i}} , \tag{C11}$$

where P_i is the power incident on the cavity and P_r is the power reflected by the cavity, one can measure P_r/P_i. Figure C-4 shows such a measurement for the cavity used in this experiment and for the case of no discharge. The data was obtained by using a directional coupler to monitor the power reflected from the cavity. At each frequency the incident power was measured by detuning the cavity with a piece of copper foil injected through the viewing slit: This procedure 'shorts out' the cavity and the incident power is totally reflected. From the data of Fig. C-4, the cavity coupling constant β (equal to the VSWR at resonance) and the loaded Q, Q_L (equal to the resonant frequency divided by the frequency separation between the half-power points) can be determined. Q_0 is then given by $(1 + \beta)Q_L$:

$$\beta = 1.27$$

$$Q_L = 1250$$

$$Q_0 = 2830.$$

For comparison, in Fig. C-5, we also present a second measurement of the loaded Q, performed by observing the power radiated out the viewing slit as a function of frequency. Figure C-5 contains two curves, one with the discharge on and one with the discharge off. The observed frequency separation of the two curves arises mainly because of heating of the quartz tube and cavity walls by the discharge. The loaded Q calculated from the separation of the half-power points is $\sim$ 1400 for both curves and indicates that the plasma discharge has little effect on the Q (at least

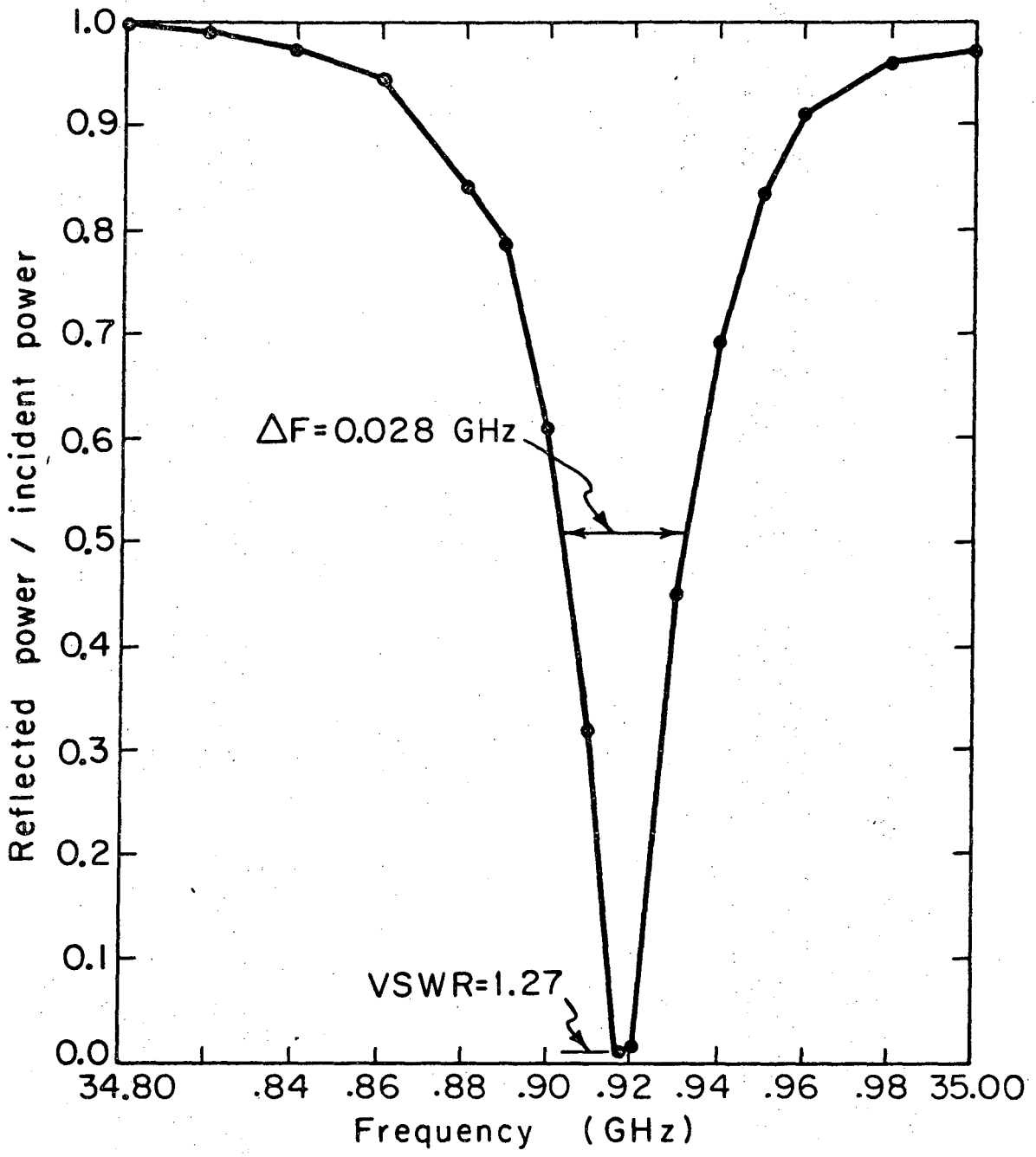

XBL742-2344

Fig. C-4. Measured ratio of microwave power reflected from the cavity to the incident microwave power as a function of the frequency.

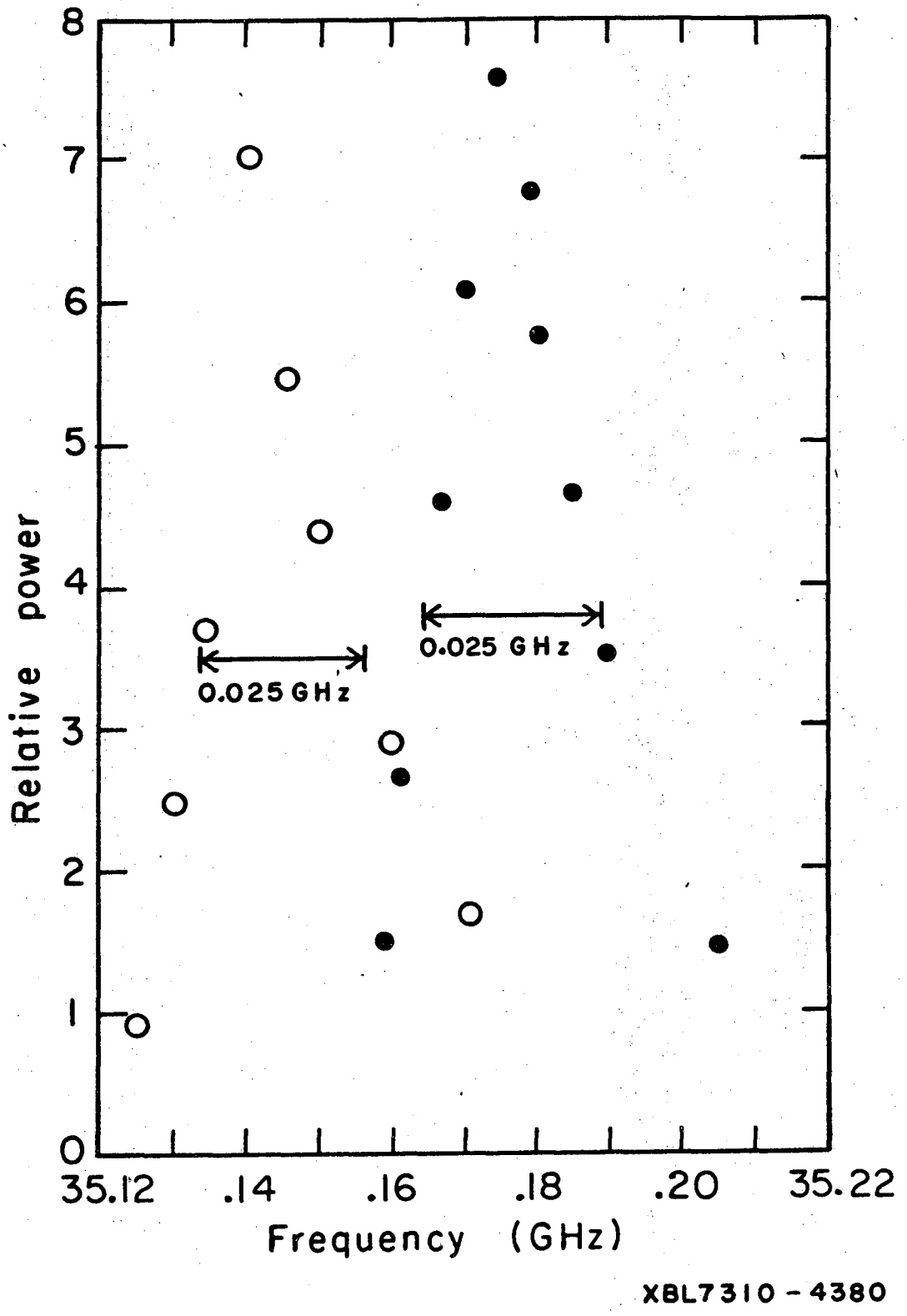

Fig. C-5. For legend, see page 122a.

Fig. C-5. Microwave power radiated from the viewing slit (Fig. C-1) of the microwave cavity versus frequency for two cases: o, discharge on; and •, discharge off.

for this set of discharge parameters). Therefore we may use Q_0 calculated above for the case of no plasma discharge to calculate $\bar{E}_0$ is a function of the input power. The result is

$$\bar{E}_0 \text{ (kV/cm)} = 2.14 \sqrt{P_0 \text{ (watts)}}. \qquad \text{(C12)}$$

D. Discussion of the Optical System

Figure D-1 shows a detailed schematic of the optical system used in this experiment. An initial 3.9 cm diameter achromatic lens is used to focus light coming from the viewing slit of the microwave cavity onto the entrance slit of a half-meter JACO Ebert monochromator. The light is diffracted by a 1200-lines ruling per mm grating, and a narrow wavelength band is selected by the exit slit for detection by an EMI 6256S photomultiplier tube located just beyond the exit slit. The spherical mirror serves to image the entrance slit onto the exit slit and to transform the diverging rays coming from the entrace slit into a parallel beam suitable for Fraunhofer diffraction. The slit height (both entrance and exit) can be continuously set at any value up to 1.35 cm. The wavelength selected for detection can be varied either by rotating the grating (coarse adjustment) or by rotating a quartz plate mounted just on the monochromator side of the exit slit (fine adjustment). A more detailed description of the operation of this latter method of tuning is given below.

A system such as shown in Fig. D-1 has several sources of 'instrumental' broadening which must be considered in calculating the 'best possible' resolution obtainable using the apparatus. Those being discussed below are: (1) the natural grating resolution, (2) finite slit width broadening, (3) diffraction due to a finite numerical aperture, (4) astigmatism, (5) curvature of the image of the entrance slit at the exit slit, and (6) an offset of the focal point due to the quartz plate used to do the fine wave-

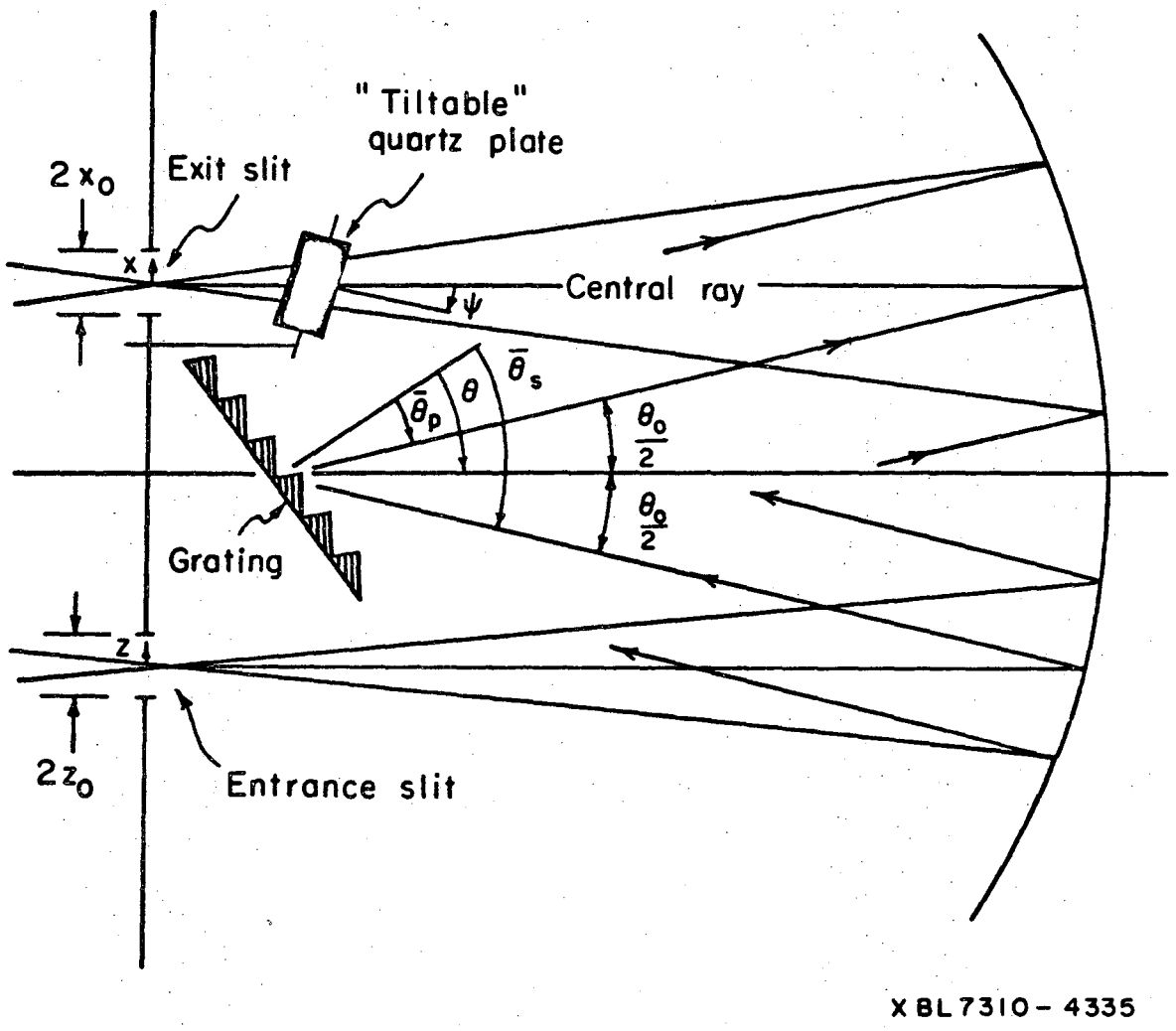

Fig. D-1. Schematic view of the optical system.

length tuning. Other sources of broadening due to the light source are discussed in Appendix E.

We begin by considering the apparatus of Fig. B-1 for the case of monochromatic light of wavelength λ incident on the entrance slit. We assume the the grating angle θ is such that light of wavelength λ which passes through the center (which we will designate as $z = 0$) of the entrance slit and is incident on the grating at the corresponding angle $\bar{\theta}_s$ and is diffracted into an angle $\bar{\theta}_p$, also passes through the center (which we will designate as $x = 0$) of the exit slit. θ, $\bar{\theta}_s$, and $\bar{\theta}_p$ must then satisfy the usual grating equation:

$$\frac{d}{\lambda}\left(\sin\bar{\theta}_s + \sin\bar{\theta}_p\right) = \frac{2d}{\lambda}\sin\theta\cos\theta_0/2 = m \qquad \text{(D1)}$$

where d is the spacing between rulings on the grating, m is the order of the grating maxima, θ_0 is the 'included angle', and

$$\bar{\theta}_p = \theta - \frac{1}{2}\theta_0, \qquad \bar{\theta}_s = \theta + \frac{1}{2}\theta_0.$$

The dispersion D giving the displacement at the exit slit corresponding to a unit change in the wavelength λ is then given by

$$D = \frac{dx}{d\lambda} = F\frac{d\bar{\theta}_p}{d\lambda} = \frac{mF}{d\cos\bar{\theta}_p}, \qquad \text{(D2)}$$

where F is the focal length of the spherical mirror. The intensity $I(x,z)$ at a position x (or for the diffracted angle θ_p) of the exit slit due to unit intensity of light of wavelength λ incident on the entrance slit at a position z (and corresponding incident

angle θ_s is given by:[31]

$$I(x,z) = \frac{1}{N}\frac{\sin^2(N\pi\delta')}{(\pi\delta')^2},\quad \delta' = \frac{d}{\lambda}(\sin\theta_s + \sin\theta_p) - \frac{d}{\lambda}(\sin\bar{\theta}_s + \sin\bar{\theta}_p)$$

$$= \frac{d}{\lambda}(\cos\bar{\theta}_s\,\Delta\theta_s + \cos\bar{\theta}_p\,\Delta\theta_p)$$

$$= \frac{d}{\lambda F}(z\cos\bar{\theta}_s + x\cos\bar{\theta}_p) \equiv \frac{d}{\lambda F}(z' + x') \qquad (D3)$$

where $\Delta\theta_s \equiv \theta_s - \bar{\theta}_s$, $\Delta\theta_p = \theta_p - \bar{\theta}_p$, N is the total number of rulings on the grating, and where we have used the property of a spherical mirror that for a small displacement 'z' the change in reflected angle $\Delta\theta_s$ is given by

$$\Delta\theta_s \simeq \frac{z}{F}$$

and similarly for x and $\Delta\theta_p$. In the last expression we have written I(x,z) in terms of $z' = x\cos\bar{\theta}_p$ and $z' = z\cos\bar{\theta}_s$, which are the slit positions as seen from the grating. Equation (D3) implies a width W_g (full-width at half-maximum intensity) given by

$$W_G = \frac{0.88\lambda D}{mN} \qquad (D4)$$

which places a limit on the resolution obtainable using the spectrometer.

The total intensity of light of wavelength λ received by the photomultiplier will be given by multiplying I(x,z) by the intensity distribution at the entrance slit J(z) and integrating the resulting expression over the entrance and exit slits, i.e., over x and z:

$$I(\lambda) = \int_{-x_0}^{x_0} dx \int_{-z_0}^{z_0} dz\ I(x,z)J(z). \qquad (D5)$$

The above expression for the intensity holds when 'geometric optics' holds, i.e., for the cases when we may calculate the path of a photon through the spectrometer by ray-tracing techniques. We may put Eq. (D5) into a more general form by defining the two quantities: $I_E(z')$, the 'effective' transmission of the entrance slit, and $I_X(x')$, the 'effective' transmission of the exit slit. Then, using Eq. (D3) to write $I(x,z)$ in terms of the single variable $\xi = x' + z'$, Eq. (D5) can be written as

$$I(\lambda) = \int_{-\infty}^{\infty} dx'\ I_X(x') \int_{-\infty}^{\infty} dz'\ I_E(z')I(x' + z')$$

$$= \int_{-\infty}^{\infty} I(\xi)S(\xi)d\xi$$

where we have now written $I(\lambda)$ as the integral of a grating function $I(\xi)$ containing the properties of the grating and a slit function $S(\xi)$,

$$S(\xi) \equiv \int_{-\infty}^{\infty} I_X(x')I_E(\xi - x')dx" \qquad (D6)$$

containing the properties of the other elements of the spectrometer, i.e., the slits, mirrors, lenses, and masks. For the simple geometric optics case of Eq. (D5), $I_E(z')$ is the intensity distribution at the entrance slit, and $I_X(x')$ is equal to unity over the exit slit and zero elsewhere.

The general problem of the form of the slit function has been extensively discussed in the literature.[39,40] The problem of an optical system illuminated through a slit was studied theoretically by von Cittert[41] who concluded that the image of the entrance slit when viewed through the optical system depended on two factors: (1) the type of illumination of the slit, coherent or noncoherent, and (2) the width W of the slit relative to W_D, the distance from the peak to the first diffraction minimum of the optical system. For the case of noncoherent illumination of a narrow slit, i.e., one satisfying

$$W \lesssim 0.5\ W_D, \qquad W_D = \lambda f \tag{D7}$$

(written in terms of the 'f' number of the optical system = focal length/smallest limiting aperture), the image of the slit is the single slit diffraction pattern of width W_D. In this limit an increase of the slit width increases the peak intensity of the pattern but does not change the width of the pattern. In the wide-slit limit,

$$W \gtrsim W_D, \tag{D8}$$

the image of the slit is the geometric image of the slit found by ray tracing through the optical system. In this limit an increase in width of the slit produces a corresponding increase in the width of the image of the slit; the peak intensity remains nearly constant, oscillating slightly about its average value as the slit width is increased. The case of coherent illumination

follows essentially the same pattern but with the following variations: (1) the diffraction limit occurs for wider slits, the corresponding condition to (D7) is $W \lesssim W$, (2) for the geometric limit the image width is somewhat less for the same slit width and the oscillations in the peak intensity are significantly greater. The conditions for noncoherent versus coherent illumination are discussed by Stockbarger and Burns.[42]

The discussion above has been general, pertaining to either a general optical system or to spectrometers. We now consider the type of spectrometer used in this experiment. Von Planta[43] has measured the slit function of an Ebert-type spectrometer for both infrared and optical spectral lines by replacing the grating by a mirror. His results showed agreement with the calculations of von Cittert. For thin slits the slit function was diffraction limited to width W_D and for wide slits the slit function width increased in proportion to the slit width. The slit function shape changed from the expected diffraction pattern for $u = W/W_c = 0.5$ to a nearly Gaussian type function for u = 1-2 and finally to the triangular function expected in the geometric limit for u = 3. These results did not depend on the wavelength of the line used in the experiment. Fastie[44,45] has extensively studied Ebert-type spectrometers and has noted two effects which lead to an additional broadening of the instrumental profile. The first is astigmatism, which produces an hourglass shaped image of the entrance slit at the exit slit. This image has zero width at the center (lengthwise) of the exit slit and reaches its maximum width at the ends

of the slit, where the image width is given by

$$W_a = \frac{0.1\ L}{f^2}\ , \tag{D9}$$

where L is the slit length. The second broadening effect is due to a curved image of the entrance slit at the exit slit due to the use of a plane grating with spherical mirrors. The sagitta of this curve is given by

$$W_C = \Delta\lambda D, \qquad \Delta\lambda = \frac{\lambda L^2}{8F^2}\ . \tag{D10}$$

We are now in a position to discuss the resolution of the spectrometer used in this experiment. The relevant experimental parameters are:

(1) m	grating order	= 1
(2) n	number of ruled lines/mm	= 1200/mm
(3) w	grating width	= 5.2 cm
(4) F	focal length	≃ 50 cm
(5) L	slit length	≃ 1 mm
(6) f	f number	≃ 10
(7) N = nw	total number of rulings	= 62 400
(8) W	slit width	≃ 8 microns
(9) $R_D = 1/D$	reciprocal dispersion	≃ 16 Å/mm.

We consider a wavelength of 5000 Å. From Eqs. (D4), (D7), (D9), and (D10):

W_G = 4.4 microns		or	$\Delta\lambda_G$ = 0.071 Å
W = 8 microns			$\Delta\lambda$ = 0.13 Å
W_D = 5 microns			$\Delta\lambda_D$ = 0.08 Å
W_A = 1 micron			$\Delta\lambda_A$ = 0.016 Å
W_C = 0.16 micron			$\Delta\lambda_C$ = 0.0025 Å.

From the above values for the widths, we can see that astigmatism and curvature effects can be ignored in calculating the instrument function of this spectrometer. Furthermore, since $W/W_d = 1.6$, geometric optics gives a reasonable approximation to the exact slit function width (although the shape of the function itself is more Gaussian). In Fig. D-2 we show an attempt to try to fit an instrument function calculated using Eq. (D3) and the assumption of geometric optics for the slit function to a measured profile of the neon spectral line at 5852.49 Å. The fit was performed using PISA (Appendix G) with the average slit width and the total number of rulings N used as parameters and the area and peak amplitude used as constraints. The resultant best fit value for the average slit width was 4.1 microns compared to the measured values, 4.4 microns for the entrance slit and 4.0 for the exit slit. These latter values were obtained by using a helium-neon laser to illuminate the slits and then measuring the minima of the resultant diffraction pattern. The best fit value for N was 64 400 compared to the calculated value of 62 400.

In the spectrometer shown in Fig. D-1 the selection of a spectral line for study was accomplished by adjusting the grating

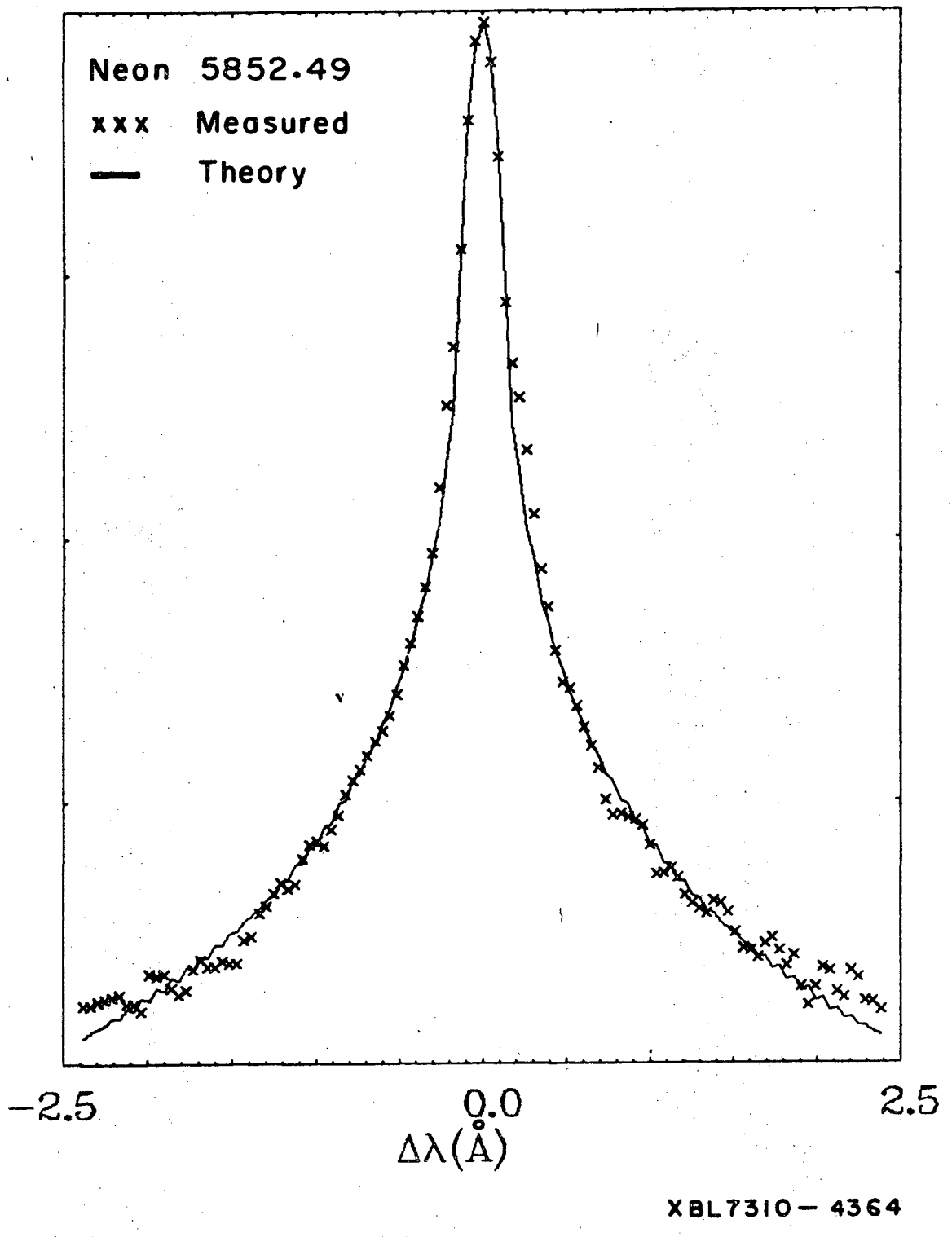

Fig. D-2. For legend, see page 133a.

Fig. D-2. Comparison of a measured neon spectral profile with the spectral profile calculated assuming a monochormator with an entrance- and exit-slit width of 4.1 microns and diffraction due to a plane grating with 64 400 ruled lines.

angle θ until the line was detected by the photomultiplier, i.e., until Eq. (D1) was satisfied. However, for the study of the line shape of a particular spectral line a second tuning mechanism was employed which provided an accurate and reproducible measurement of the line profile. This mechanism, shown in Fig. D-3, consisted of a quartz plate of thickness t which was mounted on the monochromator side of the exit slit and which was spring-loaded against the shaft of a micrometer. Movement of the shaft changed the tilt of the plate (the angle ψ) which in turn changed the wavelength detected at the photomultiplier.

Before discussing the figure we will make the following definitions: We will consider a narrow bundle of converging rays incident on the quartz plate from a spherical mirror which, if there were no plate, would be focused at P_0. In the presence of the plate there are two effects: The primary effect is a shift of the focus from P_0 to a new point P_1. Secondly, because of spherical aberration caused by the flat plate the focus will no longer be perfect, i.e., not all the rays in the bundle will intersect at the same point, hence the focus will be characterized by some finite width. However, if the bundle is sufficiently narrow, then this width will be much less than the exit slit width and can be ignored. We define a 'central ray' in the bundle to be the ray which originally came from the center of the grating; other rays will be referred to as 'lateral rays'. The angle between the central ray and the perpendicular to the quartz plate will be ψ, and ψ' will denote the angle to a typical lateral ray.

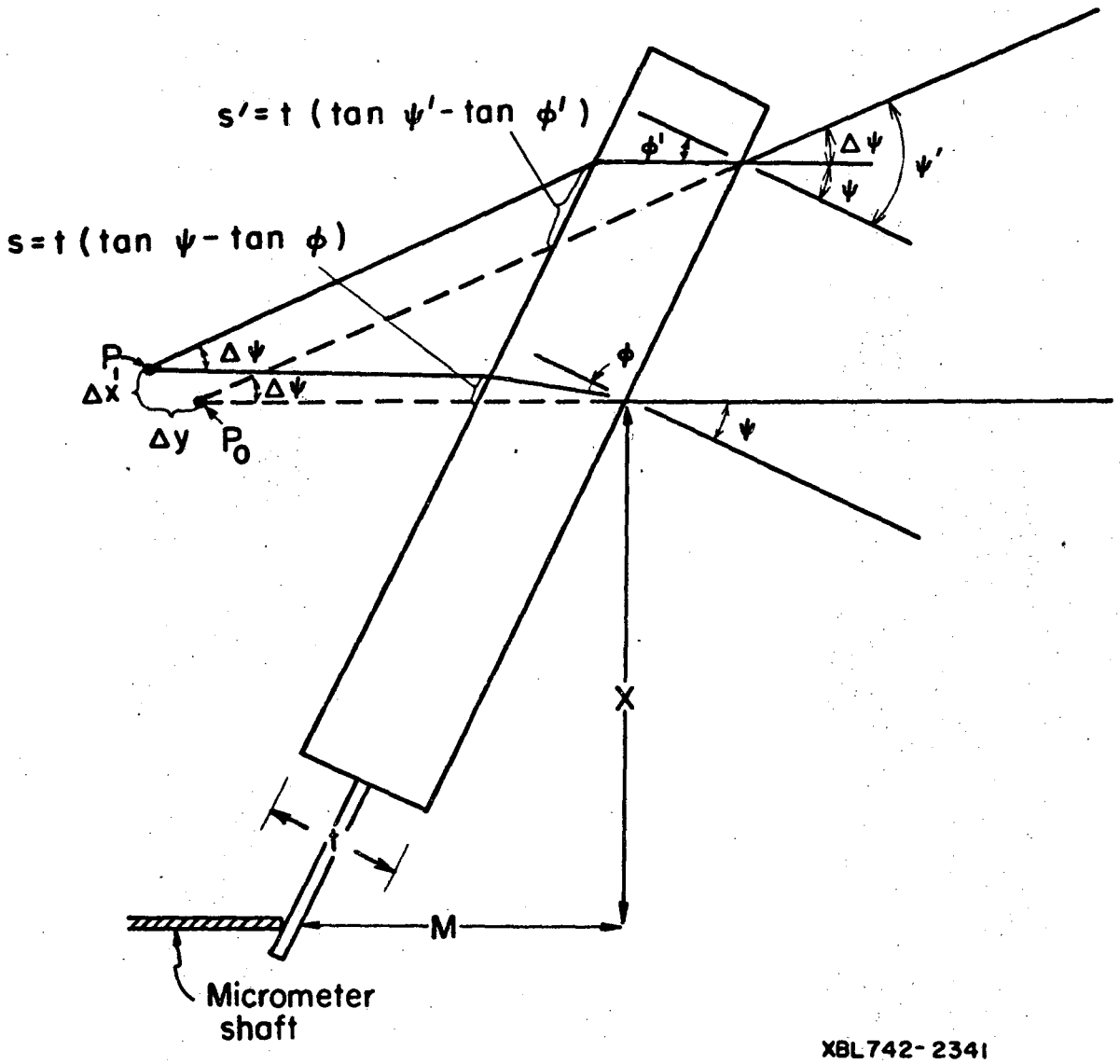

Fig. D-3. Schematic view of the quartz plate used for 'fine tuning' the monochromator.

By definition $\Delta\psi \equiv \psi' - \psi$ will be the angle between the lateral ray and the central ray. Δx will be the shift of the focus in the direction of the slit width and Δy will be the shift of the focus perpendicular to the plane of the slit. The angle ϕ' will be the angle of refraction in the quartz (index of refraction n) corresponding to an angle of incidence ψ'. The two angles are related by

$$\sin\psi' = n \sin\phi'. \tag{D11}$$

For a lateral ray at an angle ψ', Δx and Δy are given by

$$\Delta x = t \sin\psi \left[1 - \frac{\cos\psi}{n \cos\phi} \right]$$

$$\Delta y = \frac{(s' - s) \cos\psi - s' \sin\psi}{\tan\Delta\psi}$$

$$\simeq t \cos\psi \left[1 - \frac{\cos\psi}{n \cos\phi} (1 - \tan^2\psi + \tan^2\phi) \right] \tag{D12}$$

where the latter expression for Δy holds in the limit $\Delta\psi \ll 1$. Of more experimental interest than Δx versus ψ is an equation relating the change in the micrometer setting M to the shift in wavelength detected at the exit slit. From Fig. D-3 we can see that M is related to ψ by (X is defined in Fig. D-3)

$$\tan\psi = M/X.$$

Thus

$$\frac{d\lambda}{dM} = \frac{R_D t}{X} \left[\cos^3\psi \left(1 - \frac{\cos\psi}{n \cos\phi} \right) + \sin\psi \tan\psi \left(\frac{\cos\psi}{n \cos\phi} \right)^3 (n^2 - 1) \right] \tag{D13}$$

where we have used the reciprocal dispersion R_D = 1/dispersion to relate Δx to $\Delta\lambda$. The quartz plate serves as a useful wavelength tuning device when operated for $\psi \ll 1$. In this limit Eqs. (D12) and (D13) have the limiting forms:

$$\Delta x = t\psi(1 - 1/n)\left[1 + \psi^2(3 + 3n - n^2)/6n^2\right] \tag{D14a}$$

$$\Delta y = t(1 - 1/n)\left[1 + \psi^2(4 + 4n - n^2)/2n^2\right] \tag{D14b}$$

$$d\lambda/dM = (R_D t/X)(1 - 1/n)\left[1 + 3\psi^2(1 + n - n^2)/2n\right] \tag{D14c}$$

where we have kept terms to order ψ^2.

The wavelength tuning properties of the quartz plate can be summarized as follows: We assume that the angular divergence of the lateral rays from the central ray is so small that spherical aberration does not lead to a significant broadening of the focus and consequent loss of resolution. We also assume that for the purposes of this discussion the optical system has been adjusted so that for $\psi = 0$, light of wavelength λ is focused at the center of the exit slit. Then a displacement of the micrometer by ΔM will lead to a displacement of the focus in the direction of the slit width and a consequent shift of the wavelength $\Delta\lambda$ measured by the photomultiplier. The calibration constant of the quartz plate ($d\lambda/dM$) is essentially constant with only a very weak dependence on ψ and the wavelength. The error introduced into the measurement of the wavelength due to the dependence of $d\lambda/dM$ on ψ can be estimated from Eq. (D14c). For typical line profiles the maximum change in the micrometer setting was less than or equal

to ±0.1 inch. Using t = 7/16 in., R_D = 16 Å/mm, and X = 2 in. yields a maximum value of ψ = 0.05, and a maximum error in $d\lambda/dM$ of 0.06% of the value at ψ = 0.

In Fig. D-4 we present experimentally determined values of $d\lambda/dM$ versus wavelength for the equipment of Fig. D-1. These data were taken by determining the shift in the micrometer necessary to just tune between two closely separated lines whose wavelength separation was known. The figure includes values of $d\lambda/dM$ found from neon, argon, and krypton spectral lines. Using Eq. (D14) and knowledge of the index of refraction of quartz as a function of λ[46] we can determine the value of the reciprocal dispersion at any wavelength. From Eq. (D2) we see that the reciprocal dispersion is a function of wavelength and the parameters d (grating spacing), F (focal length), and θ_0 (included angle). We have used PISA (Appendix G) to fit the theoretical expression (D14) to the measured curve of Fig. D-4. For the purpose of the fit, 'd' was assumed to be equal to 8.333×10^{-5} cm (1200 rulings/mm). The resulting best fit values of θ_0 and F were $5^\circ 16'$ and 50.4 cm, respectively, which agreed favorably with the measured value of $\theta_0 = 5^\circ 9'$, and the expected focal length of ~ 50 cm.

Finally, in the discussion of the quartz tuning plate, we note that the plate is a further source of spectral line broadening. This occurs for two reasons: (1) the previously mentioned spherical aberration which arises because the different converging rays have different path lengths in the quartz, and (2) the movement of the focus in the direction perpendicular to the exit

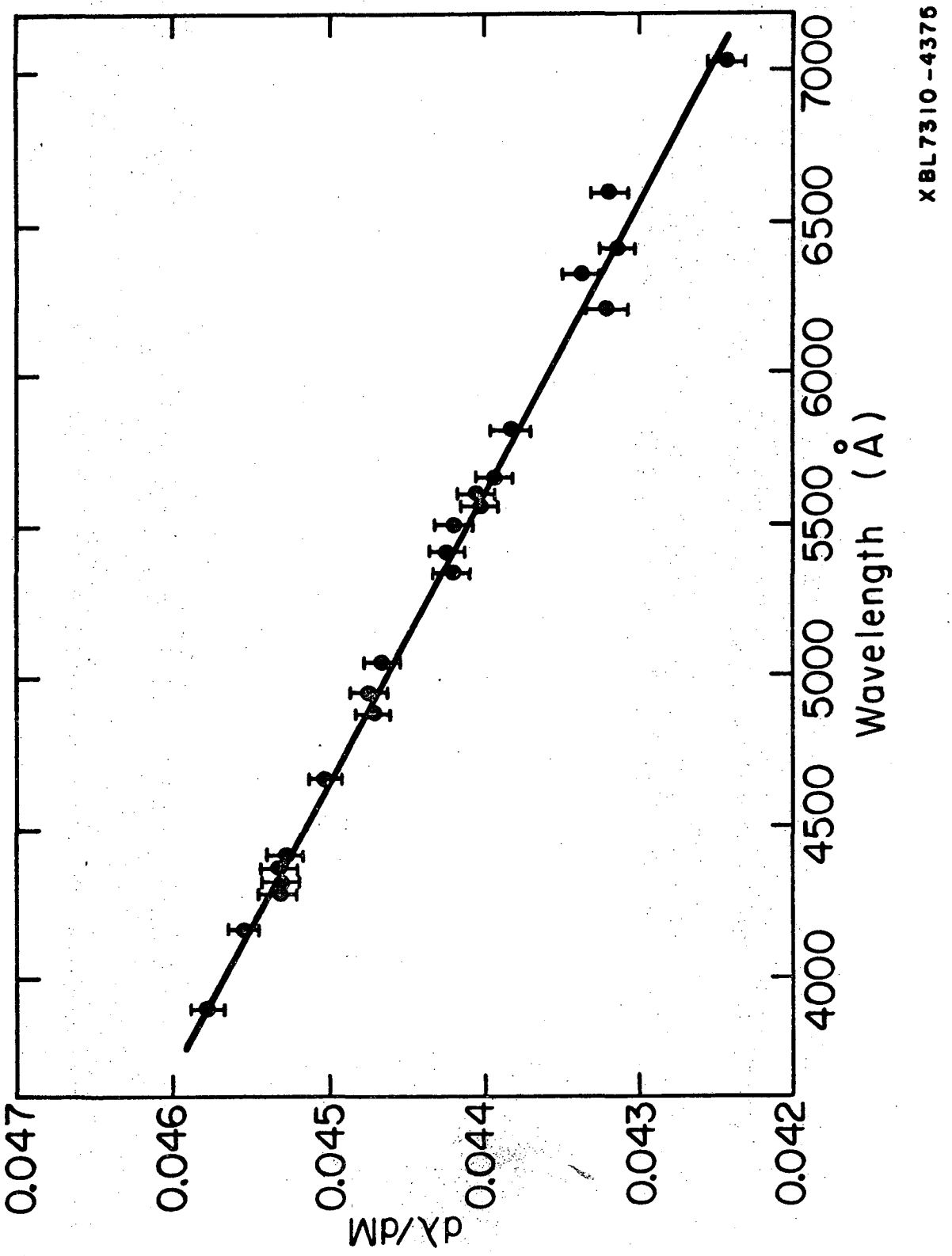

Fig. D-4. For legend, see page 139a.

Fig. D-4. Measured quartz plate calibration curves: $d\lambda$ is the change in wavelength observed at the exit slit for a change in micrometer position of dM.

slit as the micrometer adjustment of the plate is changed. We can estimate the magnitude of the first effect by considering the next higher-order corrections to the last expression in Eq. (D12). These can be shown to be of the order $t(\Delta\theta)^2$ where, as above, $\Delta\theta$ is the angle between the central ray and a given lateral ray. Defining $\Delta\theta'$ equal to the maximum-such $\Delta\theta$, the focus has a characteristic depth of

$$t(\Delta\theta')^2 = 2.5 \times 10^{-3} \text{ cm} = 25 \text{ microns},$$

where we have set $\Delta\theta'$ equal to its measured value, 0.05 radians. This focal depth corresponds to a spectral line width W_S at the exit slit of

$$W_S = t(\Delta\theta')^2 \, 2\tan(\Delta\theta) \simeq 2.5 \text{ microns}, \qquad \text{(D15)}$$

a value which does not significantly increase the broadening already produced by previously discussed methods.

We can estimate the magnitude of the second effect by noting that if the monochromator is set so that light of one wavelength is focused in the plane of the exit slit, then turning the quartz plate to another position (to measure the intensity at another wavelength) moves the focus out of the plane of the exit slit and hence broadens (or equivalently, decreases in amplitude) a spectral line which happens to be centered at the new position. The focal depth and an associated spectral line width W_Q corresponding to a maximum change in micrometer of 0.1 in. can be calculated from Eq. (D14b). The results are

$$\text{depth} = 1.6 \times 10^{-3} \text{ cm} = 16 \text{ microns},$$

and $$W_Q = 1.6 \text{ microns}. \qquad \text{(D16)}$$

This value, though small, does lead to an observable effect, primarily because the effect changes with quartz plate orientation. In Fig. D-5 we show a measurement of the peak intensity of the same neon spectral line as a function of micrometer position. For each quartz plate position, the monochromator was tuned to the neon line by rotating the grating. As can be seen, the measured intensity was peaked for a micrometer position $\simeq 350$, and fell off symmetrically on both sides. The solid line represents a line fitted to the data for use in data reduction.

As the final topic in this section on the optical system, we present a measurement of the relative attenuation of the two orthogonal polarizations of light (perpendicular and parallel to the slit). In Fig. D-6 we present a plot of the attenuation factor

$$r_{tf} = \frac{(I_\perp - I_\parallel)}{(I_\perp + I_\parallel)} \qquad \text{(D17)}$$

vs. wavelength. These data were obtained by illuminating the entrance slit of the monochromator with an unpolarized source (in this case a neon Geissler tube) and measuring the intensity of the two polarizations at the exit slit. The relative attenuation data were used to calculate the spectral profiles which were compared to the experimentally measured profiles.

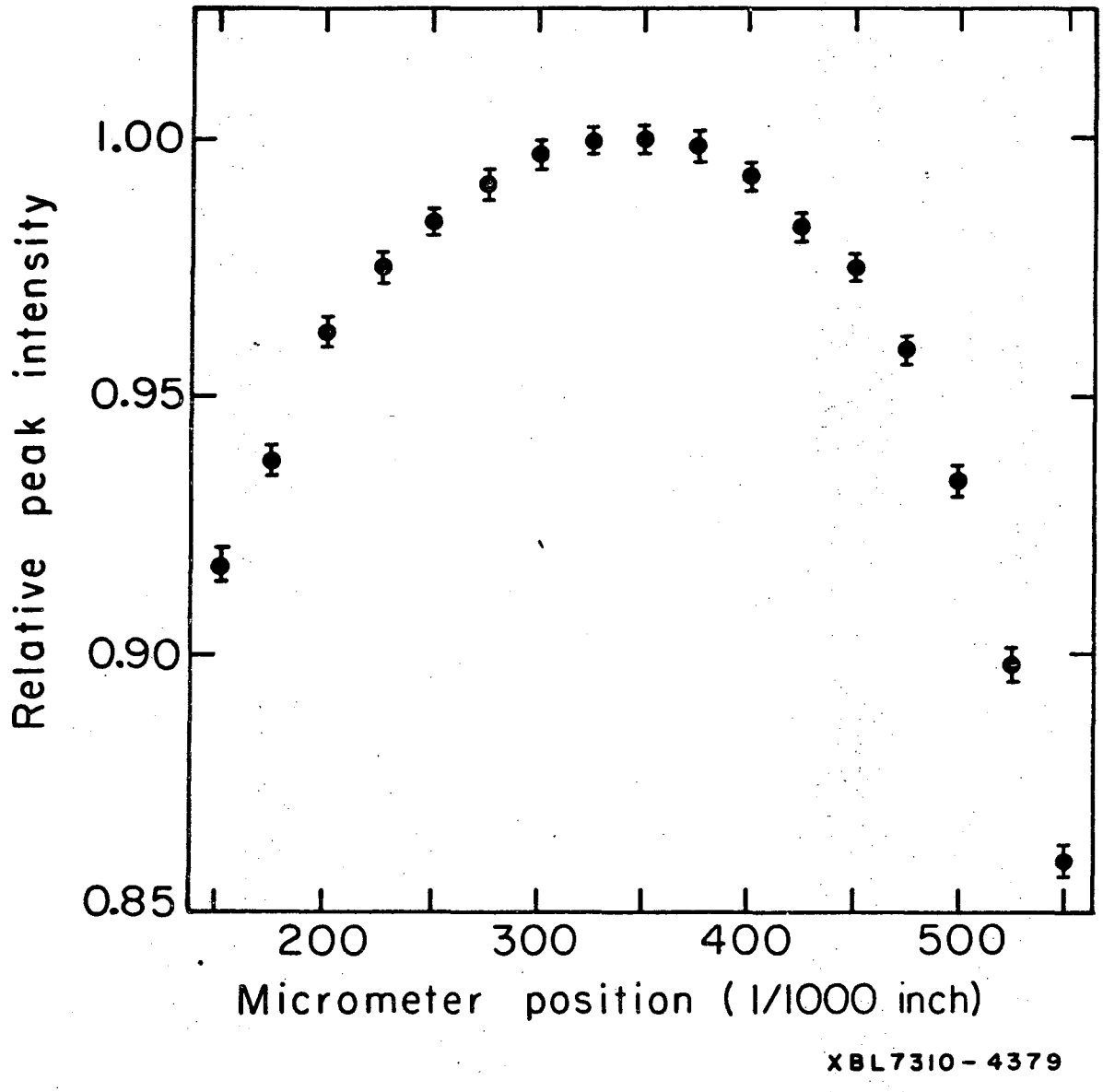

Fig. D-5. For legend, see page 142a.

Fig. D-5. Change in the measured peak intensity of a spectral line profile as a function of quartz plate angle relative to the central-ray path within the monochromator. For each plate angle (or equivalently, micrometer position) the grating was adjusted to keep the peak of the line at the center of the exit slit, eliminating any intensity variation due to line shifts.

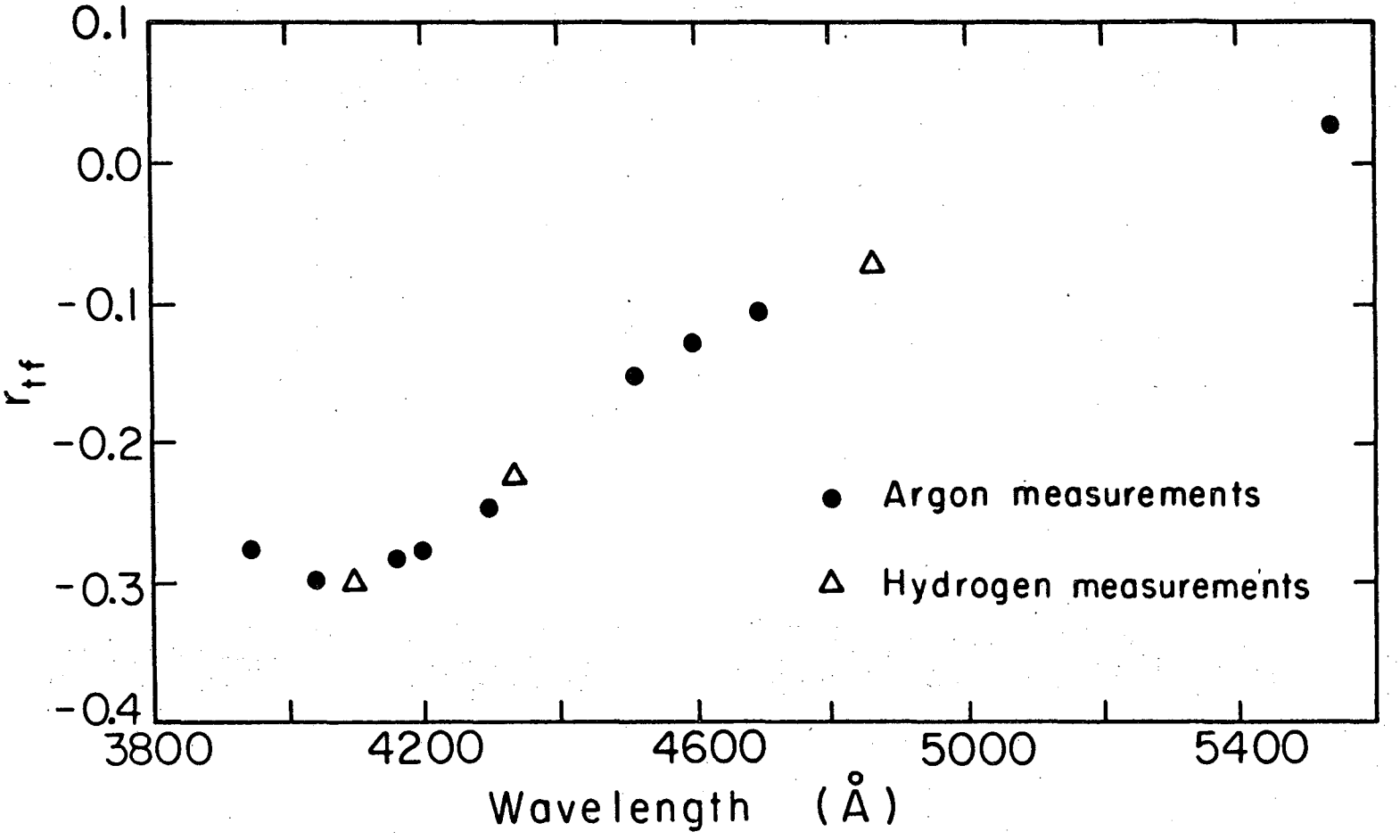

Fig. D-6. For legend, see page 145a.

Fig. D-6. Measured relative transparency of the optical system Fig. D-1) to the two orthogonal polarizations of light as a function of frequency.

E. The Plasma Discharge and a Further Discussion of Line Broadening

In this section we will discuss the plasma discharge. For simplicity we will discuss the case of a helium discharge.

We start by assuming that the neutrals in the plasma are in thermal equilibrium at the temperature of the inside surface of the quartz Geissler tube. We can estimate this temperature from the measured temperature on the outside surface (150-160°C) and by assuming that all the electric power supplied to the discharge in the capillary region is dissipated due to heat conduction through the quartz capillary walls. The dissipated heat (dQ/dt) is related to the temperature difference ΔT between the inside and the outside surfaces of the quartz tube by

$$\frac{dQ}{dt} = \kappa A \frac{\Delta T}{t} ,$$

where κ is the thermal conductivity of quartz (1.7 watt/m-deg C at 200°C),[47] A is the conducting area ($A = 2\pi r \ell$, where r is the tube radius and ℓ is the tube length), and t is the thickness of the quartz capillary wall. Setting $dQ/dt = IV = IE_z \ell$, where E_z is the longitudinal electric field ($V = E_z \ell$), yields (we set $t \simeq r \simeq 0.2$ mm)

$$\Delta T \simeq \frac{IE_z}{2\pi\kappa} \simeq 10^{\circ}C,$$

where we have used for E_z the value of 270 V/cm (see below), and for I the measured value of 3.5 mA. The neutral temperature T_n is then

$$T_n \simeq 160^{\circ}C\text{-}170^{\circ}C \simeq 0.04 \text{ eV}.$$

This value will be an upper estimate to the neutral temperature since the electric power will be dissipated by radiation as well as by conduction out the ends of the tube. However, since these effects would only affect ΔT, which is much less than the outside temperature of the Geissler tube, the calculated neutral temperature would not be significantly affected.

We can now calculate the neutral density from the gas pressure ($p \simeq 2$ torr) and the above calculated neutral gas temperature:

$$n_n = \frac{p}{kT_n} \simeq 4.3 \times 10^{16} \text{ cm}^3.$$

We can measure the electron density (n_e) of the plasma by measuring the shift in resonant frequency (δf) of the microwave cavity due to the presence of the plasma. Measurements show that $\delta f = 0.003$ GHz, for a cavity resonant frequency (f) of 35.2 GHz. The plasma frequency (and hence n_e) can then by calculated either from Eq. (C9) or by using the numerical method outlined in Appendix C (Eq. C7, etc.) to calculate the index of refraction (n_1) of the plasma necessary to account for a frequency shift of δf. In either case the index of refration is assumed to be given in terms of the plasma frequency (ω_p) by

$$n^2 = 1 - \frac{\omega_p^2}{\omega^2} .$$

Both methods yield an electron density of

$$n_e \simeq 2 \times 10^{11}/cm^3.$$

Using the measured current density ($j \simeq 2.7$ A/cm^2) we can calculate the longitudinal drift velocity of the electrons (u_e):

$$u_e = \frac{j}{en_e} \simeq 8.5 \times 10^7 \text{ cm/sec.}$$

This velocity corresponds to a translational energy of

$$\frac{1}{2} m_e u_e^2 \simeq 2 \text{ eV.}$$

For an electron traveling at a velocity u_e we can calculate the electron-neutral collision rate (ν_{en}) using standard expression (see Ref. 48, p. 50):

$$\nu_{en} = 2.3 \times 10^9 \, p \left(\frac{273^\circ K}{T_n} \right) \simeq 2.8 \times 10^9/\text{sec.}$$

We can estimate the longitudinal electric field in the following way: We assume that an electron has on the average no longitudinal velocity after a collision with a neutral; the electron then accelerates for a time t due to the longitudinal electric field (E_z) until its velocity is equal to two times u_e (average velocity equal to u_e) at which time it suffers another collision with a neutral. Since the mean time between electron-neutral collisions is $(\nu_{en})^{-1}$, E_z, u_e, and ν_{en} must satisfy

$$2mu_e = eE_z(\nu_{en})^{-1}$$

or

$$E_z = \frac{2mu_e\nu_{en}}{e} \simeq 270 \text{ V/cm.}$$

We next note that the mean path length between electron-neutral collisions for electrons traveling at a velocity of u_e is given by

$$\lambda_E \equiv \frac{u_e}{\nu_{en}} \simeq 0.3 \text{ mm}$$

and hence is greater than the inside diameter of the Geissler tube. As a result, electrons which are drifting with a mean velocity u_e along the Geissler tube and which undergo collisions in which a significant fraction of their longitudinal energy is transformed into perpendicular energy will strike the inner surface of the Geissler tube and be lost to the plasma. This will leave the plasma positively charged with respect to the Geissler tube wall (since the ions are less mobile than the lighter electrons) setting up an (ambipolar) electric field which will tend to retain the electrons and to accelerate the ions toward the tube wall. The properties of this type of physical situation have been theoretically studied and discussed in Ref. 49. It is shown there that the mean value of E_r is of the order of kT_e/er. This is consistent with the observed dc electric field of about 500 V/cm because "kT_e" must be several times larger than $\frac{1}{2} m_e u_e^2$ ($\approx$ 2 eV), and $r = 2 \times 10^{-2}$ cm. Of course, under the existing conditions of large nonuniform fields and small tube diameter, where the energy gained between collisions is comparable to the mean energy, the distribution cannot be assumed to be nearly Maxwellian, and the analysis becomes exceedingly complicated. Thus no attempt is made here to understand the ionization balance and other properties of

the discharge column in detail.

We now consider the ions. Charge neutrality requires that

$$n_i \simeq n_e \simeq 2 \times 10^{11}/cm^3.$$

The temperature of the ions will be nearly that of the neutrals, i.e.

$$kT_i \simeq kT_n \simeq 0.04 \text{ eV}.$$

This latter relation follows since the massive ions can gain only very little energy before colliding with a neutral, and because the similarity between the mass of the neutral and the ion makes energy exchange between the two particles in a collision very efficient.

Finally, in this section we will discuss two broadening mechanisms which affect the width of the line profiles observed in this experiment. The first, thermal or Dopper broadening, arises due to the motion of the neutral atoms parallel to the direction of observation. The full-width at half-maximum (FWHM) of a line which is only Doppler broadened can be expressed by

$$\frac{\Delta\lambda}{\lambda} = 2(\ln 2)^{1/2} \frac{v}{c} ,$$

where v is the particle velocity parallel to the direction of observation, and where c is the speed of light. In the following table we show the expected Doppler FWHM's for the spectral lines observed in this experiment for thermal velocities (v) corresponding to T_n = 0.04 and 0.10 eV.

Line	T_n = 0.04 eV	T_n = 0.10 eV
He 4922	0.037 Å	0.056 Å
He 4388	0.034 Å	0.053 Å
He 4144	0.032 Å	0.050 Å
H_α	0.101 Å	0.159 Å
H_β	0.075 Å	0.118 Å
H_γ	0.067 Å	0.105 Å
H_δ	0.063 Å	0.100 Å

The second broadening mechanism is the Stark effect due to the dc electric fields calculated above. For helium, the Stark effect is of second-order and the calculated line widths are much less than those due to instrument broadening, and hence can be ignored. For hydrogen, the line widths due to Stark broadening can become comparable to instrument widths, and are listed below for the cases of E_{dc} = 0.5 kV/cm and 1.0 kV/cm The former value of electric field is the measured value for this experiment, and was determined from the measured Stark broadening of H_γ and H_δ with no applied microwave electric field.

Line	E_{dc} = 0.5 kV/cm	E_{dc} = 1.0 kV/cm
H_α	0.025 Å	0.05 Å
H_β	0.05 Å	0.1 Å
H_γ	0.067 Å	0.135 Å
H_δ	0.095 Å	0.190 Å

F. Electronics--Correction of Data for Dead Time Losses

As was mentioned in Chapter IV, the data taken in this experiment used counting techniques to measure the number of photons detected by the photomultiplier. Such techniques employ electronic components with a finite frequency response due to the phenomenon of 'dead time', i.e., the time after a component has been triggered by an input pulse and before it has reset and can accept another pulse. For high pulse counting rates the number of pulses which enter the system during this dead time and are lost can be measurable and must be accounted for in interpreting the data.

Assuming that the distribution of pulses in time follows a Poisson distribution, the losses due to dead time can be easily calculated. If we assume that the pulse counting system is characterized by a single dead time τ, then the real counting rate N is given in terms of the measured counting rate by[50]

$$N_m = N - NN_m\tau, \qquad \text{or} \qquad N = \frac{N_m}{1 - N_m\tau}. \tag{F1}$$

The above expression has a very simple interpretation. The number of measured counts is equal to the number of actual counts minus the number of lost counts. The number of lost counts will be just the total time lost ($N_m\tau$) times the average number of counts per unit time, which for a Poisson distribution is N.

For a system characterized by more than one dead time the correction for the dead time losses must be modified. We will

specifically consider a two-element system composed of a discriminator with a dead time τ_1 and a set of scalers with a dead time $\tau_2 > \tau_1$. For such a system the relation equivalent to Eq. (F1) is given by

$$N_m = N_m N\tau_2 - N_m N\bar{\tau}\left[1 - e^{-N(\tau_2 - \tau_{min})}\right] \qquad (F2)$$

where τ_{min} and $\bar{\tau}$ are given by

$$\tau_{min} = \tau_2 - \tau_1, \quad \bar{\tau} = \tau_1/2 \qquad \text{for } \tau_1 \leq \tau_2,$$

and

$$\tau_{min} = \tau_1, \quad \bar{\tau} = (3\tau_i - \tau_2)/2 \qquad \text{for } \tau_1 \geq \frac{1}{2}\tau_2.$$

The above equation has the following interpretation. The first two terms on the right are equivalent to Eq. (F1): the loss term $N_m N\tau_2$ represents the counts lost while the scalers have not reset. For each measured pulse there is a further counting rate loss mechanism which we will refer to as discriminator 'retrigger'. Since the dead time of the discriminator is less than that of the scalers it resets before the scalers are prepared to accept a new pulse. Thus, there is the possibility that the discriminator will be triggered again before the scalers have reset. If the discriminator is triggered at a time t_1 (relative to the initial pulse at $t_0 = 0$) which satisfies

$$\tau_2 - \tau_1 < t_1 \leq \tau_2, \qquad (F3)$$

then the subsequent dead time of the discriminator will extend beyond the time when the scalers would normally reset. Before the discriminator resets the second time the counting system

cannot accept new pulses, hence the effective dead time of the system will be increased beyond that of a single element system with a dead time τ_2.

Again assuming Poisson statistics, the contribution of discriminator retrigger to the counting rate losses can be easily evaluated. We define τ_{min} to be the maximum of:

(1) the time (after t_0) that the discriminator has reset and is ready to receive a new pulse, and

(2) the retriggering time of the discriminator which would lead to a resulting reset time just equal to the normal reset time of the scalers, i.e., a discriminator triggered at $t_1 > \tau_{min}$ would extend the dead time of the counting system beyond τ_2.

We must distinguish two cases: if $\tau_1 \leq \tau_2/2$ then τ_{min} is determined by Eq. (F3):

$$\tau_{min} = \tau_2 - \tau_1,$$

and if $\tau_1 \geq \tau_2/2$ then τ_{min} is determined by the reset time of the discriminator:

$$\tau_{min} = \tau_1.$$

The additional counting rate loss due to discriminator retrigger is then given by

$$N_m \quad \text{times} \quad (1 - P_0) \quad \text{times} \quad N\bar{\tau}. \qquad (F4)$$

The various terms in Eq. (F4) can be identified as follows: N_m is the measured counting rate, $(1 - P_0)$ is the probability that one or more pulses (only the first is important) occur in the time period τ_{min} to τ_2 (or equivalently, one minus the probability

that there are no pulses in that time period) and hence retrigger the discriminator, and $N\bar{\tau}$ is the average number of additional pulses lost due to discriminator retrigger and is given by:

$$N\bar{\tau} = \frac{N}{\tau_2 - \tau_{min}} \int_{\tau_{min}}^{\tau_2} (t_1 + \tau_1 - \tau_2) dt_1. \qquad (F5)$$

P_0 is given by Poisson statistics to be

$$P_0 = e^{-N(\tau_2 - \tau_{min})}. \qquad (F6)$$

Substituting Eqs. (F6) and (F5) into Eq. (F4) leads to the final term in Eq. (F2).

Normal experimental practice is to keep $N\tau_2$ small so that the measured counting rate is given by the first two terms on the right of Eq. (F2). The dead time τ_2 can then be measured through the following strategy. One measures the apparent transmission of a filter which is placed so as to attenuate the light reaching the photomultiplier as a function of the number of measured counts. The resulting curve can then be used to obtain τ_2 and the actual transmission of the filter as follows: Let

N represent the actual number of counts with no filter,

N_m represent the number of measured counts with no filter,

N' represent the actual number of counts with the filter,

N_m' represent the number of measured counts with the filter,

and define

$T = N_m'/N_m$, the apparent transmission of the filter, and

$T_a = N'/N$, the actual transmission of the filter.

Then using Eq. (F1) with $\tau = \tau_2$ it is easy to show that

$$T = T_a + N'_m \tau_2 (1 - T_a). \tag{F7}$$

Thus the slope of the measured curve of T vs. N'_m gives τ_2 and the intercept of the curve with the line $N'_m = 0$ gives the actual filter transmission.

Fig. F-1 shows such a plot for the counting system used in this experiment. The data shown come from a measurement of T vs. N'_m for several helium and hydrogen spectral lines. All points are consistent with a dead time τ_2 of 2.2×10^{-7} sec (4.5 MHz). As can be seen from the intercepts of the curves for each spectral line, the actual filter transmission shows a monotonic change with the wavelength of the line.

Finally, we should see that for the data on Fig. F-1, Eq. (F1) is an adequate approximation for the exact expression Eq. (F2). We define R to be the ratio of the third term on the right of Eq. (F2) to the second term. R is then given by (expanding the exponential and keeping only the leading two terms)

$$R = \frac{\bar{\tau} N (\tau_2 - \tau_{min})}{\tau_2} . \tag{F8}$$

using the values of τ_2 and T found from Fig. F-1: $\tau_2 = 2.2 \times 10^{-7}$ sec and T = 0.11, and the rated dead time of the discriminator: $\tau_1 = 1.0 \times 10^{-7}$ sec, yields for the peak value of N'_m shown on the figure the values:

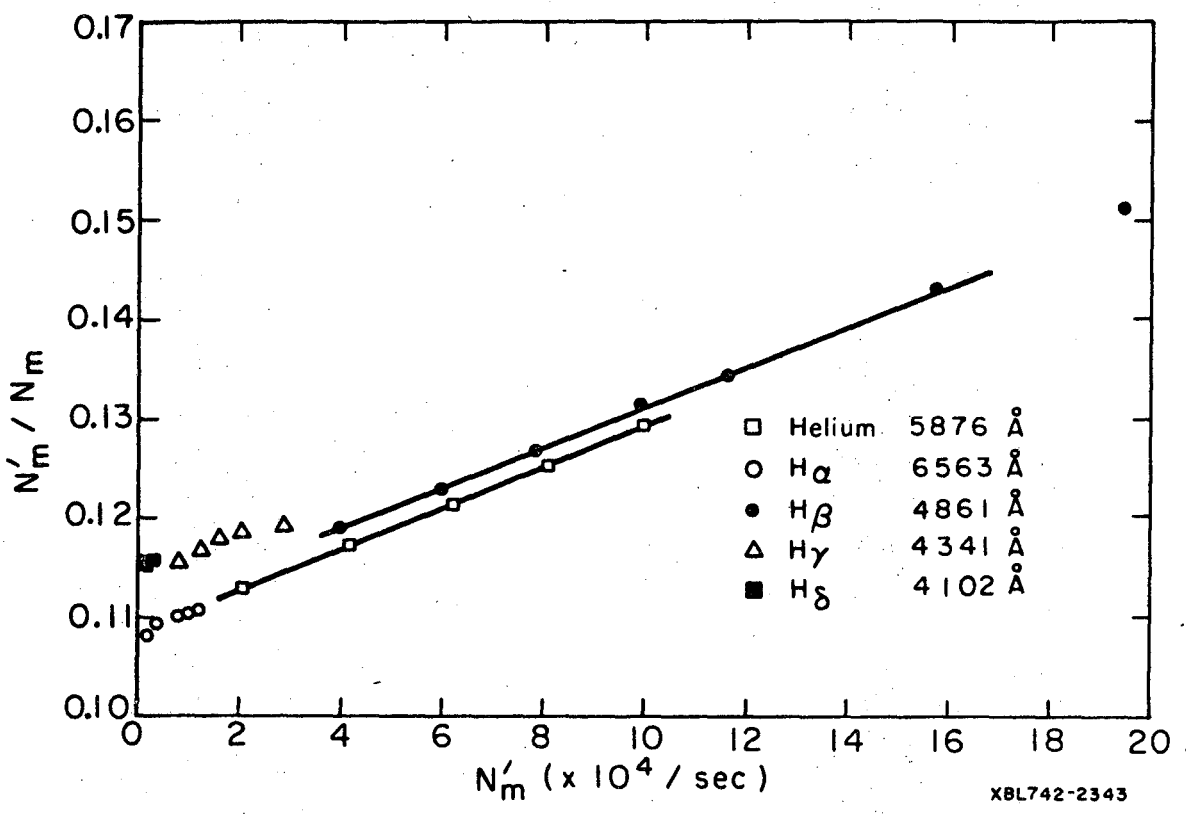

Fig. F-1. The apparent transmission of a neutral density filter measured using counting techniques. The experimental data shown for several spectral lines, can be used to determine the opacity of the filter as well as the dead time of the counting system (see text).

$N_m' = 2.0 \times 10^5$,

$N_m = 1.8 \times 10^6$,

$N = N_m/(1 - N_m\tau_{2-} = 3.0 \times 10^6$, and

$R = N\tau_1^2/(2\tau_2) = 0.07$.

Hence the approximation is justified.

G. PISA: Derivation and Discussion of Application to Spectral Profile Fitting

In comparing measured line profiles and those calculated using the methods of Chapters II and III we have made extensive use of a computer program written and developed by Klaus Halbach to do least squares fitting.[51] Although this program will be discussed within the framework of fitting spectral profiles, it is very flexible: essentially the same program has been used to design magnets for accelerators and to design extractor geometries for ion sources. The program, usually referred to by the acronym PISA, can be described as follows: combined with an analysis program that can evaluate a system performance given a set of parameters (for instance, a program which can calculate a spectral profile given the temperature, electric field strength and frequency, energy levels, etc.) PISA will vary those parameters until a 'best fit' in the least-square sense is reached. The system may have constraints (for instance, the area of a profile, or the peak amplitude, or the half-width) which must fit exactly. Before discussing the application of PISA to the fitting of spectral line profiles, we shall give an appreviated discussion of the method; a more extensive discussion is contained in Ref. 51. For simplicity, in the following discussion we will use matrix notation with the exception that all explicit matrix indications will be suppressed. The character of each variable (scalar, column vector, square matrix) will be described when it is introduced. For instance, in the text, the column vector '$\vec{p}$' is

denoted as 'p'; the $\underline{i}$th element of which is denoted by 'p_i'.

We define:

p = m-dimensional column vector formed from the parameters which will be varied by PISA.

x = n-dimensional column vector formed from the set of wavelengths at which the spectral profile is to be defined.

$\underline{s}$ = n-dimensional column vector formed from the values of the measured spectral profile intensity at the wavelengths x, i.e., $\underline{s}_i$ = measured intensity a x_i.

s(p) = n-dimensional column vector formed from the values of the calculated spectral profile intensity for the parameter set p at the wavelengths x.

$\underline{r}$ = n'-dimensional column vector formed from the desired values of the exactly fitted quantities.

r(p) = n'-dimensional column vector formed from the exactly fitted quantities.

To approximate $\underline{s}$ in the least-square sense subject to constraints, one has to find the parameter vector p_{min} that minimizes

$$S = \sum_{i=1}^{n} \left[s_i(p) - \underline{s}_i \right]^2 W_i, \qquad (G1)$$

subject to the condition

$$r_k(p) - \underline{r}_k = 0, \qquad k = 1, \cdots, n'. \qquad (G2)$$

The W_i are weight factors which may be used to fit some components

of s more closely to the measured value than others; they can usually be chosen to be

$$W_i = 1/\underline{\delta s}_i^2,$$

where $\underline{\delta s}_i$ is the experimental error in the measurement of the intensity at the $\underline{i}$th wavelength x_i. S can be minimized subject to the constraints given by Eq. (G2) by using Lagrange's method:

(1) We define the scalar quantity L by

$$L = S + \sum_{k=1}^{n'} \ell_k \left[r_k(p) - \underline{r}_k \right], \tag{G3}$$

where ℓ_k is the Lagrange multiplier corresponding to the $\underline{k}$th constraint equation.

(2) S is then minimized by solving the equations

$$\left.\frac{\partial L}{\partial p_j}\right|_{p_{min}} = 0 \qquad j = 1, \cdots, m$$

$$r_k(p_{min}) = \underline{r}_k \qquad k = 1, \cdots, n'. \tag{G4}$$

Since, in general, s and r are complicated functions of p and Eq. (G4) cannot be solved analytically, we will seek to solve it in an iterative manner suitable for use on a computer.

We assume that we have found a solution $p = p_0$, which is not the optimum solution, i.e., does not satisfy Eq. (G4). This may be the 'initial guess' at a solution or it may be the result of a previous iteration. We seek Δp such that the new solution $p = p_0 + \Delta p$ yields a calculated profile s(p) which better fits $\underline{s}$,

i.e., one for which L is less. Repeated iterations of this form will usually lead to a minimum value of L and an optimum value of $p = p_{min}$. We begin by writing L in matrix form and in terms of the vectors: $\Delta s = s(p) - s(p_0)$, $\underline{\Delta s} = \underline{s} - s(p_0)$, $\Delta r = r(p) - r(p_0)$, $\underline{\Delta r} = \underline{r} - r(p_0)$,

$$L = (\Delta s^t - \underline{\Delta s}^t)W(\Delta s - \underline{\Delta s}) + \ell^t(\Delta r - \underline{\Delta r}). \tag{G5}$$

In the above expression the weight factors have been written in the form of a diagonal square-matrix W and the Lagrange multipliers in the form of an n'-dimensional column vector ℓ. Equation (G4), the condition for an optimum solution, is given by

$$\left.\frac{\partial L}{\partial \Delta p_j}\right|_{p_{min}} = 0 \qquad j = 1, \cdots, m$$

$$r(p_{min}) = \underline{\Delta r}, \tag{G6}$$

where we have changed variables from p to Δp. We proceed by expanding Δs and Δr in Taylor series and retaining only the linear terms

$$\Delta s = M\Delta p \qquad M_{ij} = \partial s_i/\partial p_j$$
$$\Delta r = N\Delta p \qquad N_{kj} = \partial r_k/\partial p_j. \tag{G7}$$

Such an approximation will be valid in one of two cases: (1) r and s are linear functions of p, or (2) the calculated Δp is small enough that the higher order terms are negligible. Substituting the above expression into Eq. (G5), defining $a_j = \partial \Delta p/\partial \Delta p_j$, setting $\ell = 2\lambda$, and transposing some terms yields the following

conditions for an optimum solution of the linear problem:

$$\frac{\partial L}{\partial \Delta p_j} = 2a_j{}^t(M^tWM\Delta p + N^t\lambda - M^tW\underline{\Delta s}) = 0 \qquad j = 1, \cdots, m. \quad (G8)$$

Equation (G8) can only hold if the vector $(M^tWM\Delta p + N^t\lambda - M^tW\underline{\Delta s})$ is equal to zero. Hence we can solve for Δp by solving the partitioned matix equation:

$$\begin{pmatrix} M^tWM & N^t \\ N & 0 \end{pmatrix}\begin{pmatrix} \Delta p \\ \lambda \end{pmatrix} = \begin{pmatrix} M^tW\underline{\Delta s} \\ \underline{\Delta r} \end{pmatrix} \quad (G9)$$

If the system is nonlinear then the Δp calculated from Eq. (G9) will, in general, not satisfy the approximation of Eq. (G7). In this case, however, the solution of $\epsilon\Delta p$, where ϵ is some appropriately chosen number less than one, will satisfy the approximation; for this change in the parameters the problem will appear nearly linear and hence the 'new' spectral profile $s(p_0 + \epsilon\Delta p)$ will be a better approximation to $\underline{s}$ than the old one. This process can now be repeated until a suitable solution is reached.

We are now in a position to outline the operation of PISA:

(1) The user gives PISA

(a) a 'system' subroutine which calculates, for instance, at each wavelength x_i, the spectral intensity $s_i(p)$, and the partial derivatives $\partial s_i/\partial p_j$ for each parameter 'j' (if constraints are to be used then the system must also calculate $r_k(p)$ and $\partial r_k/\partial p_j$),

(b) the measured spectral profile and the weight associated with each point,

(c) an initial guess as to the parameter values.

(2) PISA then iteratively solves the least-squares problem. Each PISA iteration consists of the following steps:

(a) starting from the last (or initial) solution, p_0, the matrices M^tWM, N, $\underline{\Delta r}$, $M^tW\underline{\Delta s}$ are calculated,

(b) Eq. (G9) is then solved for Δp,

(c) a new solution for which the parameters are incremented by $\epsilon\Delta p$ is calculated and compared to $\underline{s}$ and $\underline{r}$,

(d) if convergence criteria supplied by the user are satisfied, PISA ends; otherwise

(e) the solution is tested for linearity and depending on the result, ϵ is either increased to a maximum of one, kept the same, or decreased for the next iteration, or the present solution is rejected and a new solution is constructed using the same Δp but a decreased ϵ.

Finally, we will briefly describe the application of PISA to the problem of fitting spectral profiles. We have written three system subroutines for calculating the high-frequency Stark effect suitable for use with PISA. We refer to these as helium, hydrogen, and hydrogen (modified).

1. Helium

This subroutine folds a spectrum calculated using the methods of Chapter II with an instrument function supplied by the user. It assumes a linearly polarized electric field and calculates the profile for arbitrary electric field frequency, electric field strength, and angle of observation relative to the electric field

(azimuthal angle is averaged). It can also vary the energy of the n^1F level as well as the n^1G level (if present). As discussed in the next section, the measured helium profiles had a significant contribution to the intensity due to normally forbidden transitions from the n^1F and n^1G energy levels. These unwanted lines were removed numerically when calculating the instrument function, but had to be replaced when comparing measured profiles with calculated profiles, especially for weak field strengths. For this reason the helium subroutine was given the ability to add to the high-frequency Stark profile a maximum of two simple line profiles of arbitrary position, intensity, and width.

2. Hydrogen

This subroutine folds a spectrum calculated using the Blochinzew solution to the high-frequency Stark effect Eq. (2.33) with an instrument function supplied by the user. It assumes a linearly polarized electric field and calculates the profile for arbitrary electric field frequency, electric field strength, and angle of observation (azimuthal angle is averaged). It also can vary the width of the instrument function used in the folding, thus allowing for a possible change in the instrument function width due to the effect of the microwave field on the dc electric field or temperature.

3. Hydrogen (Modified)

This subroutine calculates hydrogen Balmer-line spectral profiles in a high-frequency electric field for arbitrary electric field strength and electric field frequency. The effect of an

additional dc electric field in the plane perpendicular to the high-frequency field is included as well as the fine-structure splitting of the n = 2 energy levels. The profile is calculated using the methods of Chapter II. The instrument function is calculated from an instrument function supplied by the user, which is then Doppler broadened. The program allows an arbitrary angle of observation relative to both the high-frequency electric field and the dc electric field. The dc electric field may be assumed to be random in azimuth.

REFERENCES

1. M. Baranger and B. Mozer, Phys. Rev. 123, 25 (1961).
2. J. Reinheimer, J. Quant. Spectrosc. Radiative Transfer 4, 671 (1964).
3. W. S. Cooper and H. Ringler, Phys. Rev. 179, 226 (1969).
4. H.-J. Kunze and H. R. Griem, Phys. Rev. Letters 21, 1048 (1968).
5. G. Baravian, R. Benattar, J. Bretagne, J. L. Godart, and G. Sultan, Phys. Letters 30A, 198 (1969).
6. B. Ya'akobi and G. Bekefi, Phys. Letters 30A, 539 (1969).
7. H.-J. Kunze, H. R. Griem, A. W. DeSilva, G. C. Goldenbaum, and I. J. Spalding, Phys. Fluids 12, 2669 (1969).
8. W. S. Cooper and R. A. Hess, Phys. Rev. Letters 25, 433 (1970).
9. F. R. Scott, R. V. Neidigh, J. R. McNally, Jr., and W. S. Cooper, J. Appl. Phys. 41, 5327 (1970).
10. Y. Hamada, J. Phys. Soc. Japan 29, 463 (1970).
11. G. V. Zelenin, A. A. Kutsyn, M. E. Maxnichenko, O. S. Pavlichenko, and V. A. Suprunenko, Sov. Phys.-JETP 31, 1009 (1970).
12. N. Ben-Yosef and A. G. Rubin, J. Quant. Spectrosc. Radiative Transfer 11, 1 (1971).
13. W. D. Davis, Phys. Fluids 15, 2383 (1972)
14. R. A. Hess, Study of a Beam-Plasma Instability by Spectroscopic Methods (Ph.D. Thesis), Lawrence Berkeley Laboratory Report LBL-1531, December 1972.
15. W. W. Hicks, R. A. Hess, and W. S. Cooper, Phys. Rev. A5, 490 (1972).
16. S. H. Autler and C. H. Townes, Phys. Rev. 100, 703 (1955).

17. W. S. Cooper and W. W. Hicks, Phys. Letters 33A, 188 (1970).

18. D. I. Blochinzew, Physik. Z. Sowjetunion 4, 501 (1933).

19. V. E. Mitsuk, Sov. Phys.-Tech. Phys. 3, 1223 (1959).

20. E. V. Lifshits, S. S. Krivulya, and V. S. Us, Ukr. Fiz. Zh. 8, 1328 (1963).

21. E. V. Lifshits, Sov. Phys.-JETP 26, 570 (1968).

22. S. P. Zagorodnikov, G. E. Smolkin, E. A. Striganova, and G. V. Sholin, JETP Letters 11, 323 (1970).

23. E. K. Zavoiskii, Yu. G. Kalinin, V. A. Skoryupin, V. V. Shapkin, and G. V. Sholin, Sov. Phys.-Dokl. 15 823 (1971).

24. A. B. Berezin, L. V. Dubovoi, and B. V. Lyublin, Sov. Phys.-Tech. Phys. 16, 1844 (1972).

25. A. P. Berezin, L. V. Dubovoi, B. V. Lyublin, and D. G. Yakovlev. Sov. Phys.-Tech. Phys. 17, 750 (1972).

26. C. C. Gallagher and M. A. Levine, Phys. Rev. Letters 27, 1693 (1971).

27. C. C. Gallagher and M. A. Levine, Phys. Rev. Letters 30, 897 (1973).

28. A. Cohn, P. Bakshi, and G. Kalman, Phys. Rev. Letters 29, 324 (1972).

29. H. Margenau and G. M. Murphy, The Mathematics of Physics and Chemistry (Van Nostrand, New York, 1949), pp. 80 and 81.

30. National Bureau of Standards, Handbook of Mathematical Functions (1964).

31. J. M. Stone, Radiation and Optics; an Introduction to the Classical Theory (McGraw-Hill, New York, 1963).

32. W. C. Martin, J. Res. Natl. Bur. Std. (U. S.) A64, 19 (1960).

33. W. C. Martin, J. Res. Natl. Bur. Std. (U. S.) A74, 699 (1970).

34. J. D. Jackson, Classical Electrodynamics (Wiley and Sons, New York, 1962).

35. Reference Data for Radio Engineers (Howard W. Sams and Co., New York, 1972), 5th edition, p. 4-28.

36. S. J. Buchsbaum, L. Moyer, and S. C. Brown, Phys. Fluids 3, 806 (1960).

37. J. C. Slater, Microwave Electronics (D. Van Nostrand, New York, 1950), Ch. 5.

38. E. L. Ginzton, Microwave Measurements (McGraw-Hill, New York, 1957), Ch. 9.

39. R. A. Sawyer, Experimental Spectroscopy (Prentice-Hall, New York, 1971), p. 111.

40. G. R. Harrison, Practical Spectroscopy (Prentice-Hall, New York, 1948), p. 121.

41. P. H. Van Cittert, Zeit. f. Phys. 65, 547 (1930).

42. D. C. Stockbarger and J. Burns, J. Opt. Soc. Am. 23, 379 (1933).

43. P. C. Von Planta, J. Opt. Soc. Am. 47, 629 (1957).

44. W. G. Fasti, J. Opt. Soc. Am. 42, 641 (1952).

45. W. G. Fastie, Appl. Opt. 11, 1960 (1972).

46. The Handbook of Chemistry and Physics, 41st edition (Chemical Rubber Publishing Co., Cleveland, 1959), p. 2936.

47. American Institute of Physics Handbook, 3rd Edition (McGraw-Hill Book Company, New York, 1972), p. 4-157.

48. S. C. Brown, Basic Data of Plasma Physics (Wiley and Sons, New York, 1959), p. 50.

49. L. Tonks and I. Langmuir, Phys. Rev. 34, 876 (1929).

50. F. Robben, Appl. Opt. 10, 776 (1971).

51. K. Halbach, University of California Radiation Laboratory Report UCRL-17436, July 1967.

TECHNICAL INFORMATION DIVISION
LAWRENCE BERKELEY LABORATORY
UNIVERSITY OF CALIFORNIA
BERKELEY, CALIFORNIA 94720